JOEL FILIPE GUERREIRO

DESIGN AND IMPLEMENTATION OF A MULTILEVEL ACTIVE POWER FILTER FOR MORE ELECTRIC AIRCRAFT VARIABLE FREQUENCY SYSTEMS

APLICAÇÃO DE FILTROS ATIVOS MULTINÍVEIS EM SISTEMAS ELÉTRICOS DE AERONAVES EM REGIME DE FREQUÊNCIA VARIÁVEL

CAMPINAS
2014

i

UNIVERSIDADE ESTADUAL DE CAMPINAS
FACULDADE DE ENGENHARIA ELÉTRICA E DE COMPUTAÇÃO

JOEL FILIPE GUERREIRO

DESIGN AND IMPLEMENTATION OF A MULTILEVEL ACTIVE POWER FILTER FOR MORE ELECTRIC AIRCRAFT VARIABLE FREQUENCY SYSTEMS

Orientador: Prof. Dr. José Antenor Pomilio

APLICAÇÃO DE FILTROS ATIVOS MULTINÍVEIS EM SISTEMAS ELÉTRICOS DE AERONAVES EM REGIME DE FREQUÊNCIA VARIÁVEL

Master dissertation presented to the Electrical Engineering Post-Graduation Program of the School of Engineering Electrical of the University of Campinas to obtain the M.Sc. grade in Engineering Electrical, in field of Electrical Energy.

Dissertação de Mestrado apresentada ao Programa de Pós-Graduação em Engenharia Elétrica da Faculdade de Engenharia Elétrica e de Computação da Universidade Estadual de Campinas para obtenção do título de Mestre em Engenharia Elétrica, na área de Energia Elétrica.

ESTE EXEMPLAR CORRESPONDE À VERSÃO FINAL DA DISSERTAÇÃO
DEFENDIDA PELO ALUNO JOEL FILIPE GUERREIRO
E ORIENTADO PELO PROF. DR. JOSÉ ANTENOR POMILIO

Assinatura do Orientador

_____

CAMPINAS
2014

iii

Guerreiro, Joel Filipe, 1988-

G937d   Design and implementation of a multilevel active power filter for more electric aircraft variable frequency systems / Joel Filipe Guerreiro. – Campinas, SP : [s.n.], 2014.

Orientador: José Antenor Pomilio.
Dissertação (mestrado) – Universidade Estadual de Campinas, Faculdade de Engenharia Elétrica e de Computação.

1. Filtros elétricos ativos. 2. Inversores elétricos. 3. Kalman, Filtragem de. 4. Teoria de potência. 5. Aeronaves. I. Pomilio, José Antenor,1960-. II. Universidade Estadual de Campinas. Faculdade de Engenharia Elétrica e de Computação. III. Título.
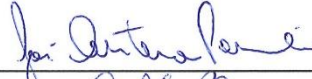
COMISSÃO JULGADORA - TESE DE MESTRADO

Candidato: Joel Filipe Guerreiro

Data da Defesa: 30 de junho de 2014

Título da Tese: "Design and Implentation of a Multilevel Active Power Filter for More Electric Aircraft Variable Frequency Systems"

Prof. Dr. José Antenor Pomílio (Presidente): _____

Prof. Dr. Helmo Kelis Morales Paredes: _____

Prof. Dr. Marcelo Gradella Villalva: _____

ABSTRACT

Aircraft Active Power Filters (AAPFs) are most commonly used to improve energy quality in Aircraft Electrical Power Systems (AEPS) by means of mitigating current harmonics, improving the source power factor and minimizing the effects of unbalanced loads. This work presents the design, simulation and implementation of a Multilevel AAPF for a Variable Speed Variable Frequency (VSVF) advanced aircraft electric power system. The AEPS is very different than the residential and industrial power systems, in these systems, the frequency may vary between 360 Hz and 800 Hz, and the load dynamics is often modified. For aircraft purposes an enhanced filtering technique is required. The proposed AAPF topology is composed by an Asymmetrical Multilevel Inverter (AMI), controlled by the Conservative Power Theory (CPT) and synchronized by a Kalman Filter Phase-Locked Loop (KF-PLL). A three phase AAPF prototype was implemented in order to investigate the proper system operation and accurateness to the simulations.

Keywords*: Aeronautical Active Power Filter, Asymmetrical Multilevel Inverter, Kalman Filter-Phase Locked Loop, Conservative Power Theory, More Electric Aircraft.*

RESUMO

Filtros Ativos de Potência Aeronáuticos (FAPA) são geralmente utilizados para melhoria da Qualidade da Energia em Sistemas Elétricos de Potência Aeronáuticos (SEPA). Os FAPA compensam os harmônicos de corrente, aumentam o fator de potência e minimizam os efeitos de cargas desbalanceadas. Este trabalho apresenta o desenvolvimento, simulação e implementação de um FAPA pra um SEPA avançado de velocidade e frequência variável. O SEPA é muito diferente dos sistemas elétricos residenciais e industriais, nesses sistemas a frequência pode variar de 360 Hz a 800 Hz, além do mais a carga se reconfigura repetidamente. Deste modo, uma estratégia avançada de filtragem ativa é necessária para SEPAs, O FAPA proposto neste trabalho é composto por um inversor multinível do tipo cascata assimétrica, o algoritmo de controle é implementado utilizando a teoria da potência conservativa e a sincronia do FAPA com o SIPA é realizada por meio de um algoritmo PLL com filtro de Kalman. Um protótipo trifásico é implementado para validar ambos o FAPA e as simulações.

Palavras Chave – Filtros Ativos de potência aeronáuticos, Inversor multinível em Cascata Assimétrica, PLL com Filtro de Kalman, Teoria da Potência Conservativa, Avião Mais Elétrico.

CONTENTS

"Success is nothing but a choice"
O sucesso é apenas uma escolha.

À minha mãe
Iracema Guerreiro de Albuquerque;
Aos meus irmãos
David Jonas Guerreiro e
Isabela Cristina Guerreiro

ACKNOWLEDGMENT

The Acknowledgement is written in Portuguese language.

LIST OF FIGURES

LIST OF TABLES

LIST OF ABBREVIATIONS

AAPF	Aircraft Active Power Filters
AC	Alternate Current
AEPDS	Advanced Electrical Power Distribution System
AEPS	Aircraft Electrical Power Systems
ADC	Analogic-Digital Converter
AMI	Asymmetrical Multilevel Inverter
APF	Active Power Filter
APU	Auxiliary Power Unit
ATRU	Autotransformer Rectifier Unit
CBs	Circuit Breakers
CC	Constant Current
CCStudio	Code Composer Studio
CCU	Contactor Control Units
CEPDS	Centralized Electrical Power Distribution System
CF	Constant Frequency
CPT	Conservative Power Theory
CP	Constant Power
CV	Constant Voltage
DC	Direct Current
ECS	Environmental Control System
ELMU	Electrical Load Management Units
EUT	Equipment Under Test
FTEPDS	Fault-Tolerant Electrical Power Distribution System
GCU	Generator Control Unit
HSPMSG	High Speed Permanent-Magnet Synchronous Generator
HTE	High-Temperature Electronics
HVDC	High Voltage DC
IDG	Integrated Drive Generator
IFE	In-Flight Entertainment

KF-PLL	Kalman Filter Phase-Locked Loop
MEA	More Electric Aircraft
MIL	Model in the Loop
MOET	More Open Electrical Technologies
PCC	Point of Common Coupling
PDC	Power Distribution Centre
PECs	Power Electronics Circuits
PFC	Power Factor Corrector
PF	Power Factor
PHC	Perfect Harmonic Cancellation
PID	Proportional Integral and Derivative
PIL	Processor in the Loop
PLL	Phase-Locked Loop
PM	Permanent Magnet
PVS	Programmable Voltage Source
RAT	Ram Air Turbine
RMS	Root Mean Square
RSU	Relay Switching Units
RT	Remote Terminal
RU	Rectifier Unit
SCM	Staircase Modulation
SDEPDS	Semi-Distributed Electrical Power Distribution System
SIL	Software in the Loop
THD	Total Harmonic Distortion
VFSG	Variable Frequency Stator Generator
VSI	Voltage Source Inverter
VSVF	Variable Speed Variable Frequency
WBG	Wide-Band Gap
WIPS	Wing Ice Protection System

1 INTRODUCTION

The world of airline economics is leading to the appearance of techniques for reducing the operating costs of aircraft. There is a trend in the aerospace industry to increase the amount of electrically powered equipment on future aircraft [1]. This movement is called the "More Electric Aircraft" (MEA). The progress of MEA [2], [3] technologies has increased dramatically due to the rise of electronically controlled solutions, such as the use of electrical energy instead of hydraulic, pneumatic and mechanical means to power all aircraft subsystem including flight control actuation, environmental control system and utility function [4]. The new systems are expected to provide great benefits in terms of reduced overall aircraft weight, reduced life cycle costs, system reliability, actuation accuracy, and energy efficiency [5].

Moreover the non-linear electrical loads, mostly electronically controlled, are becoming a challenge due to the strict standards of the aircraft power distribution system. The use of Aeronautical Active Power Filters (AAPFs) is well known to overcome power quality deviations [6]. However, the application of filtering techniques in avionics systems may lead to limitations. Those are related to the high fundamental frequency of the Aeronautical Electric Power System (AEPSs), which is 400Hz.

Nowadays, some airplane power networks use the Variable Speed Variable Frequency (VSVF) topology such as the Airbus A380 and the Boing 787, with fundamental frequency varying between 360Hz and 800Hz. The use of AAPFs is probably the unique solution to compensate power networks quality deviations.

Considering the AEPS characteristics, it is challenging to design and implement an AAPF. The solutions address the use of advanced control techniques and high performance devices in order to comply with the aeronautic standards. However, this sort of embedded filtering technique is not yet fully established, and there are some important aspects, such as the tracking of high frequency variations and electromagnetic compatibility that should be improved. Different issues are faced when referring to the hardware level. To achieve an effective compensation performance, it is required power converters with semiconductor devices that can operate in high switching frequency, as well as the digital controllers that must be able to process many variables, with high accuracy, resolution and sample rate.

This research project addresses these limitations and issues proposing a high performance solution. By means of an AAPF, the AEPS will both meet the Military Aircraft Electrical Standards MIF-STD-704F and the IEEE Std. 519.

The proposed AAPF topology is composed by an Asymmetrical Multilevel Inverter (AMI), the control references are obtained by means of the Conservative Power Theory (CPT) [7] and synchronized by a Kalman Filter Phase-Locked Loop (KF-PLL). Based on the development stages of the project, this thesis is divided as follows:

Chapter 2 presents the state of art of the More Electric Aircraft followed by a study of the Aeronautical Electric Power Characteristics and Power Quality Assessment. Furthermore, the Aeronautical Electric Power Standards are shown, as well as the State of Art of the current AAPFs and finally the proposed solution.

Chapter 3 begins reporting the modeling of the AAPF, followed by an accurate simulation implemented in the Matlab/Simulink platform in order to validate the digital implementation of the control.

Chapter 4 presents a comprehensive model of an AEPS, a case study is used for simulating the AAPF during steady-state and dynamic operations. The above simulation verifies the feasibility of the AAPF and the high performance of the control strategy.

Chapter 5 presents the implementation of a prototype and a case study is developed in the laboratory.

Finally, chapter 6 is a conclusion of the results obtained by both prototype and simulations.

2 STATE OF ART

More-Electric Aircraft (MEA) is the future trend in adopting electrical power for driving the aircraft systems. The MEA is anticipated to achieve numerous advantages such as optimizing the aircraft performance and decreasing the operation and maintenance costs, as well as reducing the emissions of air pollutant gases. However, some challenges on the aircraft electrical system come with the advent of the MEA, such as the new architectures, power electronics devices and management controls. This chapter introduces the outline for MEA, shows the Electrical Power Topologies and Quality Issues based on standards. It also includes an investigation of the roll of Aeronautical Active Power Filters (AAPFs) and an overview of the state of art of these devices.

2.1 MORE ELECTRIC AIRCRAFT

The MEA industry is placing great attention in the design of electrical systems to replace conventional devices. In this context there are several pros and cons related to the optimal designs of the newer electrical and mechanical systems.

2.1.1 Benefits of More-Electric-Aircraft

The aircraft industry is propelling the use of technologies that can reduce the cost in the design, operation, and maintenance, as well as the fuel consumption of most avionics systems. The conventional aircraft architecture has four energy sources: Pneumatic, Electric, Hydraulic and Mechanical, as shown in Figure 2-1.
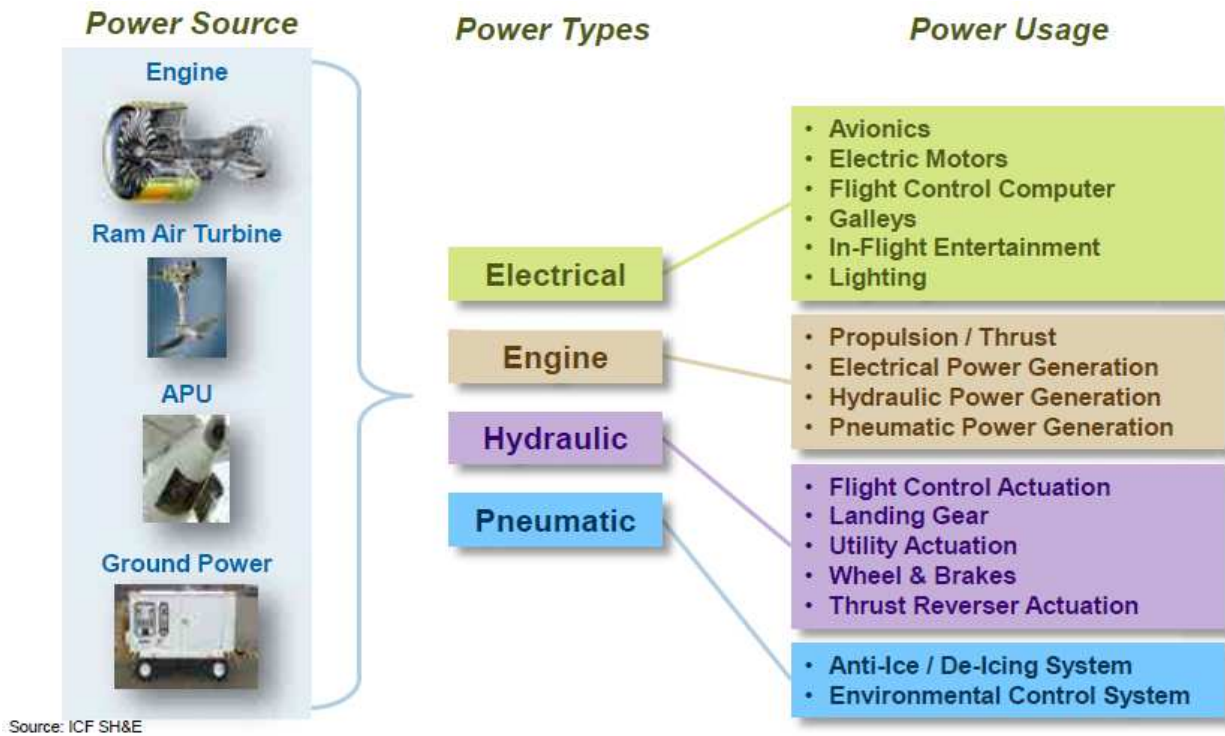
Figure 2-1: Conventional Aircraft Power Sources. [8]

The aim of MEA is to identify, optimize, and validate the innovative aircraft equipment systems. The proposed electrical solutions can reduce consumption of non-propulsive power, and thus fuel burn. This trend has led engineers to modify the electrical part of the aircraft, replacing conventional systems by electrical systems [4]. An example is the "More Open Electrical Technologies" (MOET) Integrated Project, executed from 2006 to 2009, under European Commission 6th Framework Program [9].

These studies and validation testing show that MEA has both, advantages and disadvantages to more electrical systems. So far, electrical systems are relatively heavier than conventional mechanical, hydraulically and pneumatic systems. This weight increase is related to heavy power electronics and heavy drives, which transfer hundreds of kilowatts of electric power through the aircraft.

However, electrical systems are more energy efficient. One of the main reasons is that the losses in electrical cabling are lower than those in hydraulic or pneumatic piping. Additionally, electrical systems can be designed to work in real time mode, performing their functions only at the right time. Nowadays, the central hydraulic lines are kept energized during the entire flight, such as landing gear and secondary flight control, which are used during short time. Electrical

4

systems can be designed to provide exactly the needed function, reducing the danger of hydraulic system to have too little or too much available power in the pipes. As illustrated in Figure 2-2, MEA architecture is more simplified due to the removal of pneumatics and hydraulics.
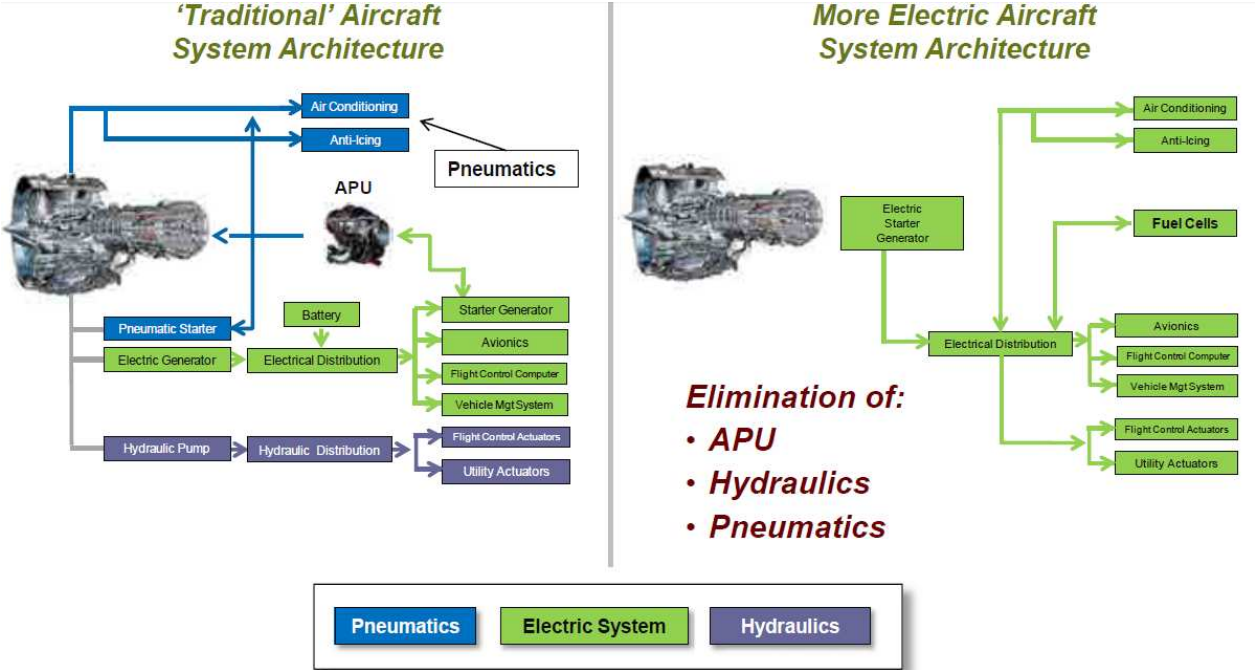
Figure 2-2: Conventional and MEA System Architecture. [8]

Some architectures have large reductions in energy losses and electrical system architectures render the aircraft no longer dependent on engine speed or thrust. All these solutions resulted in reduced fuel burn.

Another benefit of MEA is the reliability. The replacement of a bleed-air-based Environmental Control System (ECS) by an electrical ECS leads to reliable systems. The bleed-air-based is a high pressured system, which presets drawbacks such as risks . Equivalent systems are developed to the landing gear. This all leads to reduced airline maintenance costs [10].

The continuous investments and research has led to the evolution of the power needs in aircrafts, as shown in Figure 2-3.
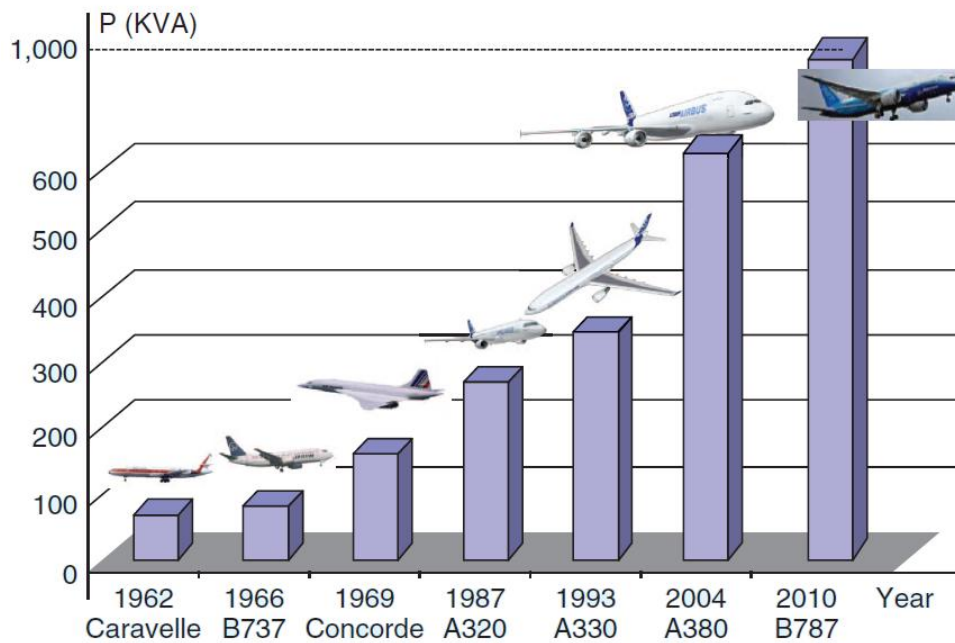
Figure 2-3: Evolution of electrical power needs. [11]

The first generation of AEPS adopted were in fixed-frequency ($115/200V$ $400Hz$) as on the A320, A330, and A340. In order to simplify the constant-speed mechanical gearbox, the variable-frequency generators replaced the fixed-frequency ones, as on the A380 and on the next A350. In these models the voltage standard is doubled ($230/400V$) due to the increase in electrical power needs.

THALES AES [12] has proposed a permanent magnet (PM) generator directly as part of the engine. This approach was used in MOET project, the simulations of the electrical network can be seen in Figure 2-4.
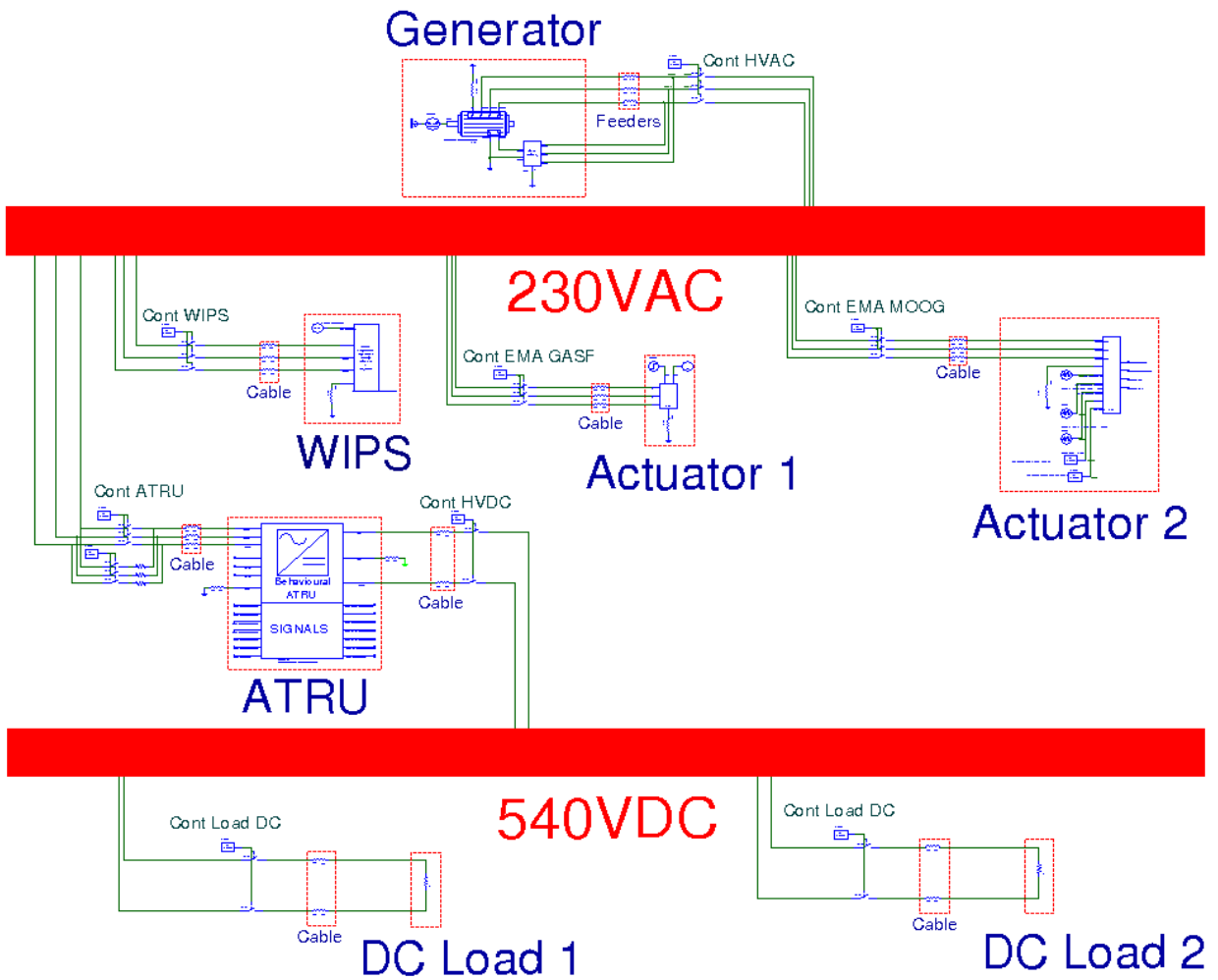
Figure 2-4: Simulation of MOET AEPS using Thales' Generator. [9]

The 230 V bus is supplied by a PM generator. The wing ice protection system (WIPS) and the two electro mechanical actuators are connected to the 230VAC variable frequency system. An autotransformer rectifier unit (ATRU) is connected to supply the $\pm270VDC$ bus bar.

The introduction of variable frequency generation requires the replacement of loads by electronically-fed loads in order to work properly in the variable frequency standards (360–800 Hz).

A power/mass ratio of 4 kW/kg such as DC/AC converters is considered applicable to aircrafts. However, system integration in aircraft with filtering equipment and cooling systems may reduce this density to 2 kW/kg.

In the near future electrical and hybrid vehicles technologies will be applied to aerospace, even if environmental and safety constraints are different [11].

The Boeing B787 [13] skyrocket the transition process to MEA. The electrical bleed less system was proposed to decouple engine operations from the air conditioning and deicing system. As a consequence the hydraulic powered loads were replaced by electrical power loads (braking, pumps). The engine start-up is now electrically powered through the torque-controlled Variable Frequency Stator Generator (VFSG), which has a voltage source inverter (VSI) dedicated to power the VFSG in motor mode to start the engine [14]. For the Boeing 787, the absence of "bleedless effect" multiplies by 4 the electrical embedded power because of the removal of the mechanical and pneumatic networks and partial removal of the hydraulics, what results in four $250kVA$ generators, Figure 2-5.

2.1.2 Challenges of More-Electrical Aircraft

For the regular aircrafts to turn into MEA, there will be a very challenging transition. The embedded power system will be more integrated, what means a significant increase in the number of electronic devices, which will need to be more powerful, compact and reliable. The power electronic devices will face several environmental constrains, such as temperature and pressure. Low pressure and high voltages may impact in power electronic devices, in this scenario there is the possibility of partial discharge and arcs.

In transmission lines, High Voltage Direct Current (HVDC) architecture is used to economically transmit large amount of power over large distances, as well as improve stability and control at minimum losses. While in the aircraft, the HVDC grid means lower cable weight, lighter converters, thus a good combination in cost efficiency.

Nevertheless, aircraft HVDC buses poses some problems related to power quality. The increasing number of power electronic loads such as AC/DC rectifier stages and Auto-Transformer Rectifier Unit (ATRU) leads to power quality deviations, such as harmonics. A better electrical system solution would be a HVDC Network associated with a generator and its control unit, a rectifier unit and an Aeronautical Active Power Filter (AAPF), Figure 2-5.

Boeing 787 and Airbus 350 variable frequency generators have output voltage of $230\ V$ to obtain a HVDC network of $\pm 270V\ DC$, this standard has been applied in the MOET EU project [1].
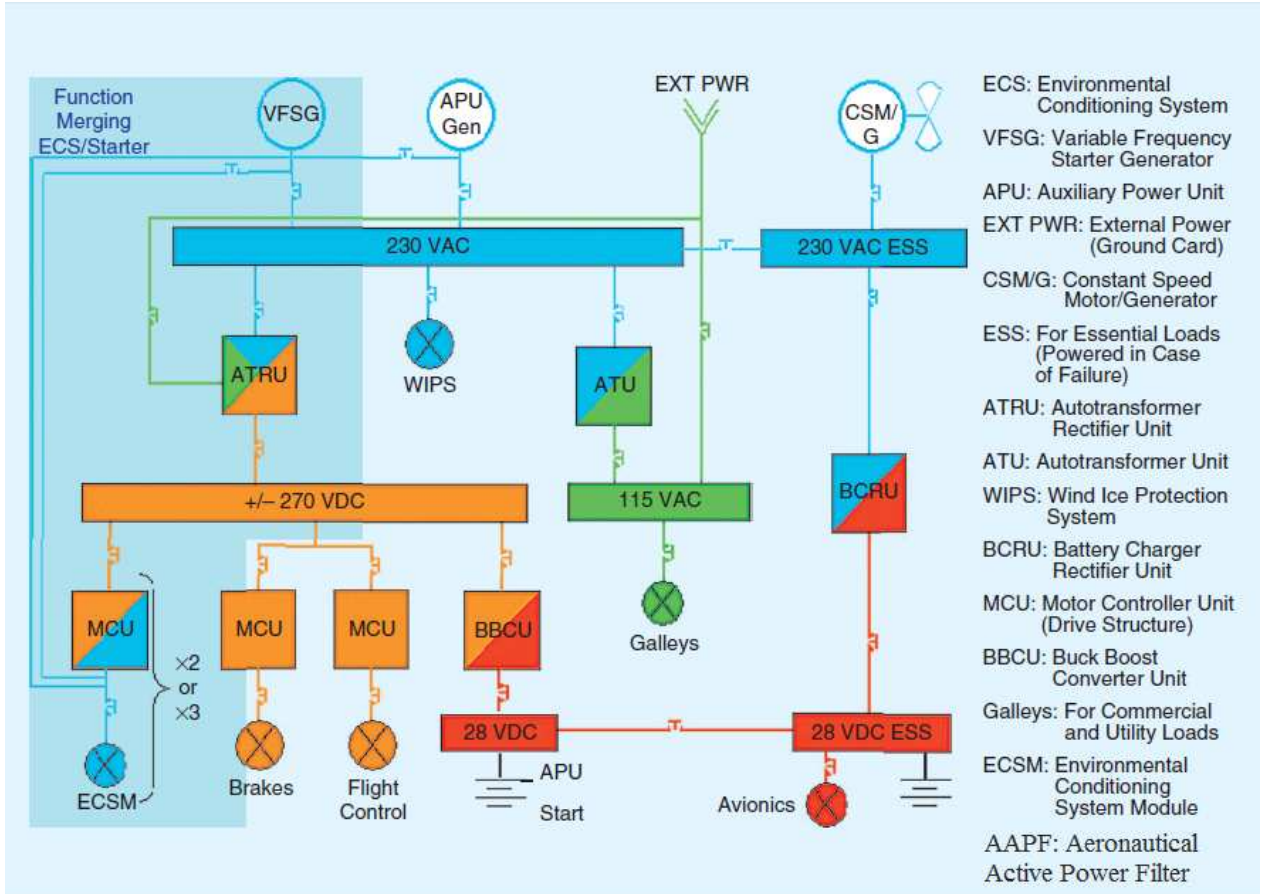
Figure 2-5: Bleedless architecture with HVDC aircraft power system. [11]

The new aircraft HVDC bus consisting of a generator, a rectifier unit (RU), a filter in the DC side, and a generator control unit brings issues in terms of quality and stability. As the power loads supplied with controlled power electronics works normally in a constant power point, however, the system may become instable if a convenient filter sizing is not achieved [15]. It is important to remark that HVDC makes easier the coupling between the main source and storage devices in the event of total engine fails. In the other hand, the harmonic spectrum in the variable AC side is worrying [16].

Some optimization studies were done to aircraft HVDC systems [17], focused in analyzing the operation of the systems of Figure 2-5. These studies proved a possible mass reduction by 30% in the amount of electrical devices.

The High Speed Permanent-Magnet Synchronous Generator (HSPMSG) is a considerable challenge. Issues related to high speed, losses and temperature are very problematic. Figure 2-6 illustrates the operating points of the HSPMSG. At the field weakening operation, the generator operates under high speeds, resulting in higher reactive currents and lower torque, what impacts in the temperature. Therefore the optimal sizing of the HSPMS, as well as the newer electrical systems, are very important subjects to be studied [18].
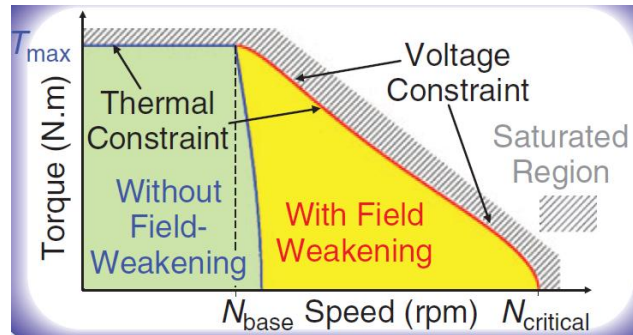
Figure 2-6: Field Weakening in HSPMSG. [11]

Moreover, the various aspects of the power quality and stability in more-electric aircraft electrical systems are of extreme importance to render the above topologies reliable.

2.1.3 Discussion

The MEA technologies are targeting specially gains in terms of mass. Many advantages come, such as the energy rationalization and management capacity, maintenance costs and electrical systems, making aircraft greener.

However, the electrical systems have to deal with unusual issues, as well as their power density should also be increased to save mass. The integration of power devices to the system is very challenging, as well as controlling the network stability.

The aircraft standards, devices, and electrical constraints should be explored in order to achieve MEA. The next section will come with more details of MEA electrical architectures and standards.

2.2 MEA POWER GENERATION AND DISTRIBUTION SYSTEM AND AIRCRAFT ELECTRIC POWER STANDARDS

MEA puts some challenges to the electrical systems, both in the amount of the required power and the processing and management of this power. This section investigates the possible topologies for the power systems of the aircraft where the power generation, power electronics interfacing circuits and design requirements are highlighted.

2.2.1 MEA Distribution systems

As previously shown in Figure 2-5, and is currently in use by the aeronautical industry, the power distribution system of the civil aircrafts is composed of combined AC and DC topologies. As an example, AC supply voltage of 115V/400Hz is used to power large loads, while 28V DC is used for avionics and flight control [19]. The recent trend in using HVDC is propelled by the possibility of using new variable frequency generation options, recent advancements in the areas of interfacing circuits, control techniques, protection systems, and, finally, the advantages of the high voltage DC distribution system in reducing the weight, the size and the losses, while increasing the levels of the transmitted power [20].

Different topologies were suggested for implementing the distribution system in MEA [21], these are the:

1. Centralized Electrical Power Distribution System (CEPDS),
2. Semi-Distributed Electrical Power Distribution System (SDEPDS),
3. Advanced Electrical Power Distribution System (AEPDS),
4. Fault-Tolerant Electrical Power Distribution System (FTEPDS).

2.2.1.1 Centralized Electrical Power Distribution System (CEPDS)

CEPDS is a radial power distribution system, Figure 2-7, with one Power Distribution Centre (PDC), the "Avionics Bay", where the voltage regulation is also located. In this topology, each load is supplied individually. The CEPDS pros and cons are as follows.

Pros:

- Easy maintenance; decoupling between loads; and fault tolerance.

Cons:

- No upgrade possibilities; faults in the distribution affect all loads; and it is costly and unreliable.
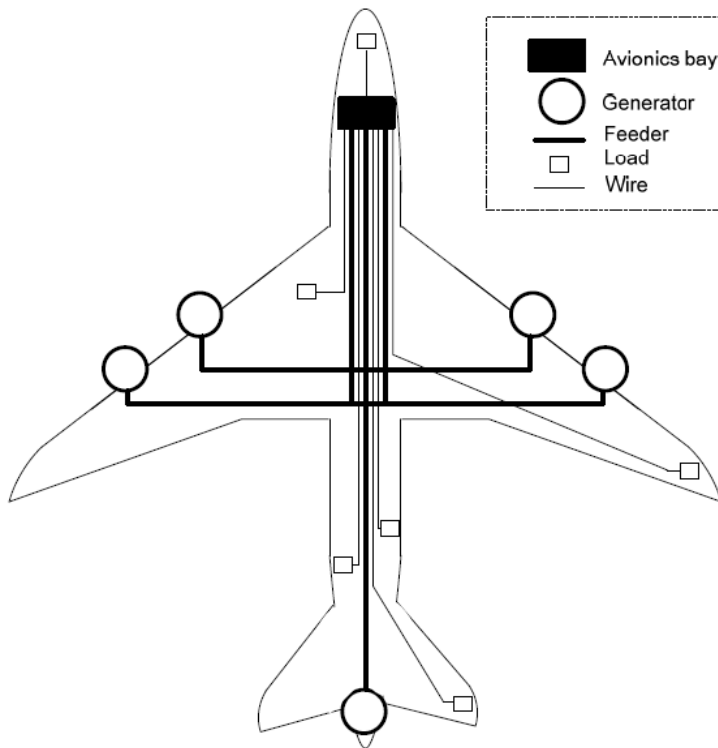
Figure 2-7: Centralized Electrical Power Distribution System CEPDS for the MEA. [19]

2.2.1.2 Semi-Distributed Electrical Power Distribution System (SDEPDS)

The SDEPDS was created to overcome the limitations of CEPDS. The main difference is a large number of PDC, Figure 2-8, which are located close to loads and distributed around the aircraft to optimize the system volume, weight and reliability. The SDEPDS pros and cons are as follows:

Pros:

- Improved power quality and Electromagnetic compatibility, high efficiency and cost effective, efficient and stable system operation, high level of redundancy in primary power distribution path and easy to upgrade

Cons:

- The close coupling among the loads can lead faults and disturbances to propagate to nearby loads.
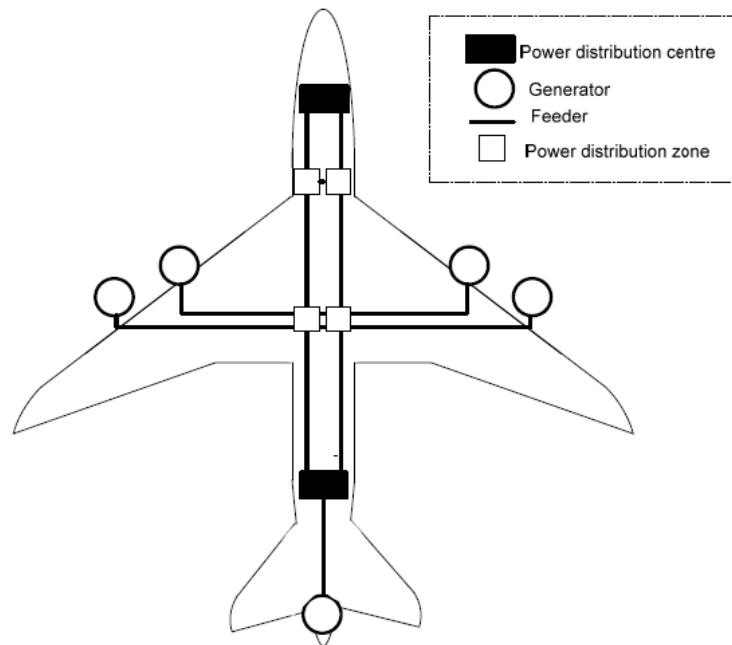
Figure 2-8: Semi-Distributed Electrical Power Distribution System SDEPDS for the MEA. [19]

2.2.1.3 Advanced Electrical Power Distribution System (AEPDS)

The AEPDS is a microprocessor controlled fault-tolerant system. As shown in Figure 2-9, the electrical power from the generators, Auxiliary Power Unit (APU), battery or ground source is supplied to the primary power distribution, where the Contactor Control Units (CCU) and high power contactors are located. The voltage/frequency regulation, damping oscillation and power flow control is done by the primary PDC.

The loads are supplied by the Relay Switching Units (RSU), which is controlled and monitored by the Remote Terminal (RT) unit. The Electrical Load Management Units (ELMU) control the distribution system, exchanging data/control strategies with the RTs. The AEPDS pros and cons are as follows:

Pros:

- Reduced life cycle cost, power quality management, reduction in the weight and wiring and fault-tolerance.

Cons:

- The concentration of the distribution and management may interrupt the whole system operation in the occurrence of a fault.
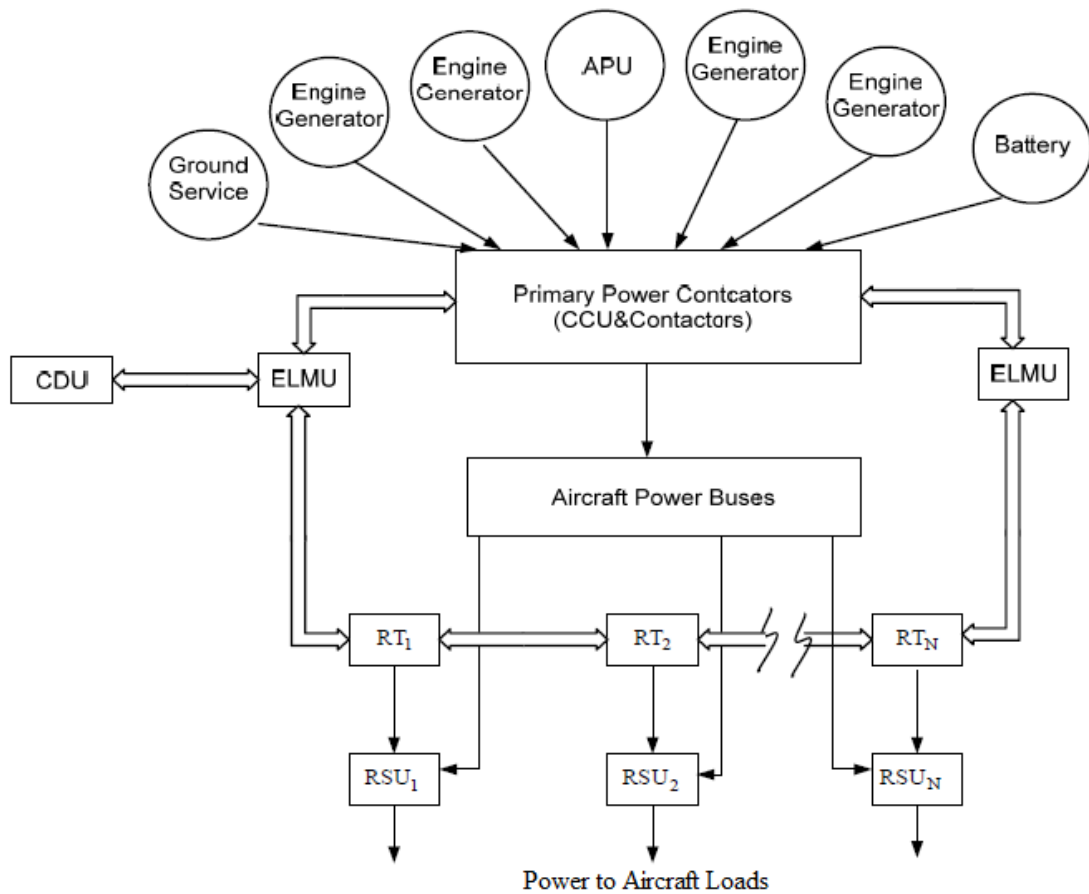
Figure 2-9: Advanced Electrical Power Distribution System AEPDS for MEA. [19]

2.2.1.4 Faulted-Tolerant Electrical Power Distribution System (FTEPDS)

As it is called, the FTEPDS is well protected, it is a mixed distribution system; the AC power from generators is connected to a source switch matrix and the 270V DC system is connected thought power converters.

This system enables the possibility of bi-directional power flow which allows integral starter/generator operation. The generator can act as motor, starting the propulsive engine and, later, on working as a generator to supply the aircraft electrical system, Figure 2-10. The $270V$ DC system also has a bi-directional power flow, to charge the batteries during flight. Moreover the DC system can stabilize during faults and disturbances thanks to the bidirectional characteristic. The FTEPDS pros and cons are as follows:

Pros:

- Aircraft engine start by generator, high redundancy and fault-tolerant.

Cons:

- A fault in source/load switch matrices may interrupt the operation of the entire system.
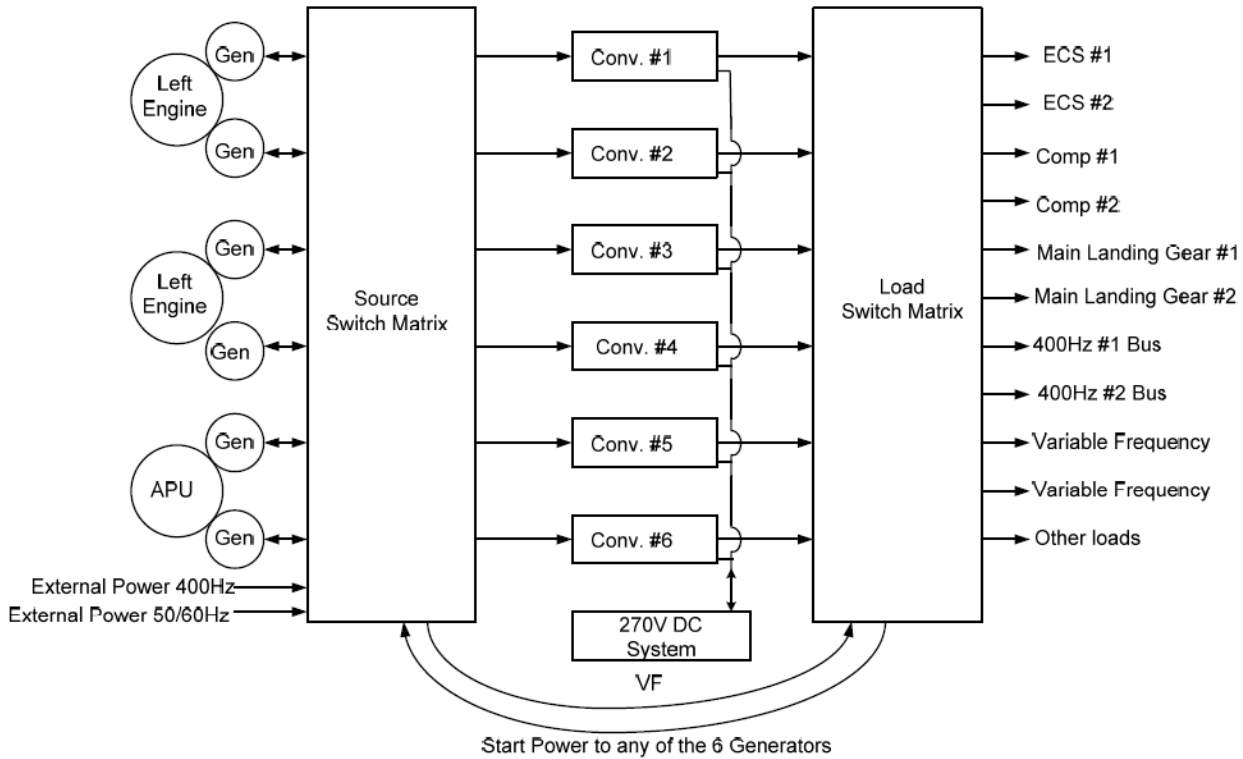
Figure 2-10: Fault-tolerant Electrical Power Distribution System FTEPDS for MEA. [19]

2.2.1.5 IMPACT OF REGENERATION INTO AC POWER BUS

The bi-directional power flow characteristic leads to the study of the impacts of transient regeneration on the voltage quality of the AC bus. The regeneration study can exploit the property that any of the power system buses be supplied by more than one source. The architecture of Figure 2-5 enables power regeneration while using a FTEPDS.

Regeneration can occur either when the actuation system deals with aerodynamic forces or when a fast response from an actuator is requested, resulting in a high rate of deceleration.

16

Taking into account some safety margin, the "normal" regeneration scenario, is assumed as a $100\,ms$ pulse of 17 kW mechanical power on the actuator shaft. In this scenario the voltage transients of the HVAC bus (230V AC) should be assessed against the specified in the military standard [22] during transients initiated by both, rising and falling regenerative power pulses.

The model and simulation of active damping system for the HVDC distribution system is described in [6]. The $\pm270V$ DC link is normally damped using a passive filter that comprises a large DC-blocking capacitor and a resistor, Cd and Rd. The active stabilizing method monitors the DC link voltage variation and stabilizes the drive system by injecting a small proportion of the DC link voltage variation into the current control loop via a DC-AC inverter, Figure 2-11.
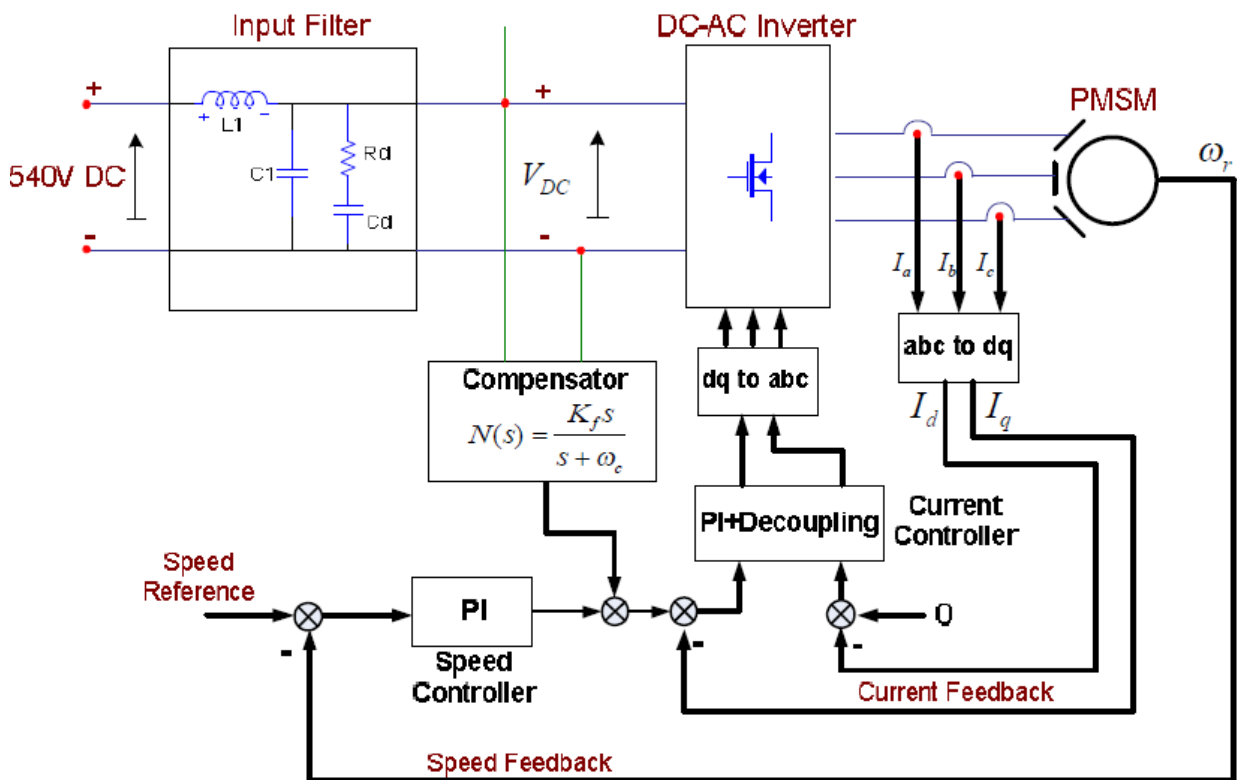
Figure 2-11: Active stabilizing method. [6]

2.2.2 Electric power generation in MEA

The electrical power needed onboard MEA has been increasing due to the growth of loads in aircrafts such as the In-Flight Entertainment (IFE) systems, Figure 2-3. Not only are aircraft

electrical system power levels are growing, but the diversity of the power generation types is increasing as well. The civil aircraft power generation topologies are shown in Figure 2-12.
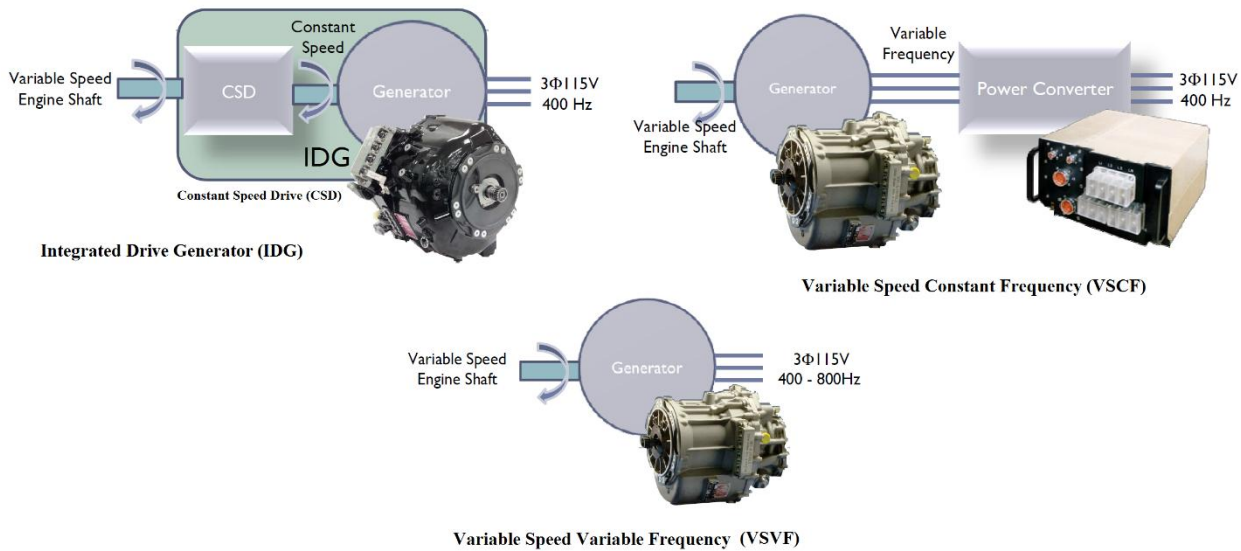
Figure 2-12: MEA Primary Electric Power Generation. [23]

2.2.2.1 Integrated Drive Generator (IDG)

The IDG provides Constant Frequency (CF) generation in three-phase 115 V/400 Hz. This scheme is the most common, as it is in-service in most civil aircrafts. In the IDG CF system, the generator is attached to the engine thought a heavy mechanical gearbox. This structure is required, since the generator must maintain a constant speed, irrespective of the engine speed. The IDG must be examined constantly and it does not allow internal starting of the engine.

2.2.2.2 Variable Speed Constant Frequency (VSCF)

The VSCF DC-link system is preferred for most military and commercial aircraft. In this scheme the generator is directly attached to the engine, thus the electrical system frequency varies as well. Regarding this issue, an interfacing power electronics circuit is placed, this circuit first converts the power from AC to DC. Then a three-phase inverter is used to convert the DC power

in three-phase $115V/400Hz$. The VSCF DC-link option is generally characterized by simplicity and reliability.

2.2.2.3 Variable Speed Variable Frequency (VSVF)

The VSVF is the most recent power generation topology. In this approach the generator shaft is directly attached to the engine, this method is known as "Embedded Generation". In this scheme there in no need of the take-off shaft and the gearbox, which reduces the size and weight and increase the reliability [24]. However there are implications of placing electrical machines in the core of the engine, such as:

- A new design of the engine components which might change the structure and aerodynamics.
- Heat losses require additional exchange of heat.

The features of VFVS are the small size, weight, volume, and cost as compared with other aircraft electrical power generation options. However, this system may pose risk when operation in high power, which need to be addressed.

Rolls-Royce is developing a More Electric Engine for MEA, the more electric engine eliminates the bleed-air systems, which are replaced by electric generators. As pointed out by [25], "one of latest steps is the 'More Electric Aircraft'. But even before the first flight of the 'More Electric' Boeing 787 Dreamliner, at Rolls-Royce, we were already looking at technology for the next development, the - More Electric Engine" Figure 2-13.
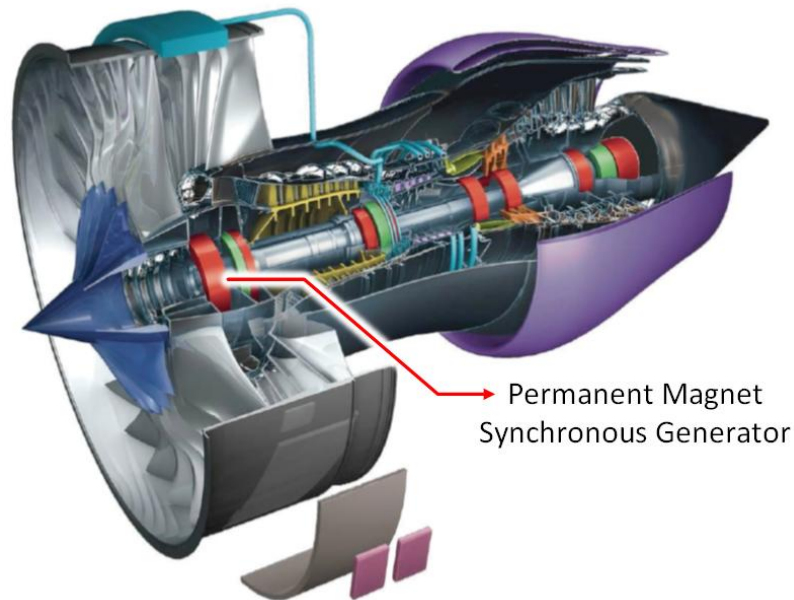
Figure 2-13: Rolls Royce More Electric Engine. [25]

2.2.3 Generator Topologies

The increase in electrical power generation on MEA leads to VSVF. When generators are mounted on the engine shaft, harsh operating conditions may arise. For that there is the need of innovations in materials, processes and thermal management systems design. In the recent years many machines were considered to be used in MEA systems, for example, Induction, Switched Reluctance, Synchronous and Permanent Magnet Machine types [21].

Below is a list of possible machines and their pros and cons:

1. Induction Generator:

    Pros: Robustness, reduced cost and ability to withstand harsh environment

    Cons: Requires complex power electronics and have low power density compared to other machines.

2. Synchronous Generator:

    -   Pros: Reliable and inherently safe; as the field excitation can be removed and the ability to absorb/generate reactive power.

    -   Cons: External DC excitation, which decreases the reliability and the efficiency.

3. Switched Reluctance Generator:

- Pros: Very simple robust structure; and can operate over a wide speed range and fault-tolerance.

- Cons: High acoustic noise and torque ripples.

4. Permanent Magnet Synchronous Generator:

- Pros: Ease of cooling, almost zero rotor losses, high efficiency compared to other machine types, high volumetric and gravimetric power density, and high pole number with reduced length of stator end windings and self-excitation.

- Cons: Inferior fault tolerance compared with Switched Reluctance machines; and requires power converters with high VA rating.

The fault-tolerant PM Machines are a solution because they offer high levels of redundancy and fault tolerance. The high number of phases provides the ability to deliver a satisfactory level of torque/power after a fault.

5. Emergency Power Generator

The emergency power is sourced from generators coupled to a Ram Air Turbine (RAT). This system has several drawbacks as it is expensive, costly to maintain, unreliable and unpopular.

2.2.4 Interfacing Circuits and Protection System

As shown in Figure 2-5 it is required to convert the electrical power from one level to another, using Power Electronics Circuits (PECs) such as AC/DC, DC/DC and DC/AC converters. This circuitry must be efficient and satisfy requirements such as reduced weight and volumetric dimension, fault-tolerance, have the ability for operation in harsh conditions, present electromagnetic compatibility with other electric systems, and be easy to upgrade.

The Wide-Band Gap (WBG) High-Temperature Electronics (HTE) is an example of electronics improvements to MEA [26]. These devices are able to operate under high temperatures (600ºC) and have high efficiency in low temperatures (-55ºC to 125ºC).

Many advantages will come from the use of WBG-HTE devices:

- Elimination of cooling flight control electronics;

- Reducing the engine control system weight and volumetric dimension;

- Improving the system reliability;

- Reducing the installation and running cost;
- Improving system fault-tolerance and redundancy.

For the Protection system, the distribution system is protected by Circuit Breakers (CBs) and Solid State Circuit Breakers, which are power electronics based breakers.

2.3 POWER QUALITY OF AIRCRAFT ELECTRIC POWER SYSTEMS

The power quality characteristics of the MEA electric power system must be in compliance with the most recent military aircraft electrical standards MIL-STD-704F as well as with the IEEE Std. 519.

The Aircraft Electrical Power System (AEPS) has several nonlinear loads connected to it, most commonly DC loads. The DC loads are connected either to the high voltage $\pm 270V$ DC bus as well as to the $28V$ DC bus. Some of these loads are electronically controlled and connected thought DC-DC converters. They are classified as constant power (CP) loads, constant current (CC) loads, and constant voltage (CV) loads. The proliferation of controlled electrical loads in MEA demands a lightweight, efficient and reliable cooling system for the associated power electronics.

2.3.1 Power Quality and Harmonic Control

Based on Figure 2-5, the Autotransformer Rectifier Unit (ATRU) is responsible for the conversion from $230V$ AC to $\pm 270V$ DC. Most of the DC loads are connected to this bus, as well as the $28V$ DC. The current absorbed by the DC loads impacts in the power quality of the AC bus side.

Nonlinear loads change the sinusoidal form of the current, what distorts the voltage. The flow of harmonic currents in the AC power system can cause interference with communication circuits and other types of equipment, what can be very problematic in an aircraft. A known solution to mitigate the effects of nonlinear loads is the use of passive filters. However passive compensation is impractical in VSVF AC systems. The system frequency varies constantly what detune these filters.

In a VFVS system, the harmonics will be multiples of the system frequency at a determinate time. If frequency may vary from $360 Hz$ to $800 Hz$, the harmonic spectrum will vary from $360 \cdot n Hz$ to $800 \cdot n Hz$, where n is the harmonic order.

The effects of current harmonics on a power system depend on feeder impedance that determines the voltage distortion, as well as the system short-circuit level. The AEPS has a very high short circuit level compared to residential and industrial systems. Capacitor banks, cables and loads alter the impedance in each node of the circuit. Resonant conditions can arise due to the inductive characteristic of the feeder impedance associated with the capacitive devices.

Yet, in the AEPS, the resonance condition is extremely risk. It may exist even when the distortion levels comply with the standards. Resonances can impact in the operation of essential equipment, as follows:

- A major effect of harmonic voltages and currents in electrical machines, such as induction and synchronous, is increased heating due to iron and copper losses at the harmonic frequencies, reducing the machine efficiency and development of torque.

- In transformers, the current harmonics cause an increase in copper losses and stray flux losses, and voltage harmonics cause an increase in iron losses.

- In cables, harmonics cause additional heating over and above what would be expected for the RMS value of the waveform. This happens because of the "skin effect" and "proximity effect," both of which vary as a function of frequency as well as conductor size and spacing.

- In electronic equipment abnormal operation can be caused by harmonic distortion. Harmonic distortion can result in a shifting of the voltage zero crossing or the point at which one phase-to-phase voltage becomes greater than another phase-to-phase voltage.

- In meters and instrumentation, these are affected specially in resonant conditions due to EMI caused by in high harmonic voltages and currents on the circuits.

The control of harmonic currents can be done by methods, i.e. shunt filters, phase multiplication and harmonic compensation or injection.

Harmonic analysis must be done for an AEPS planning process. This procedure is due to the increasing level of harmonic generation associated with normal system loads [27].

2.3.2 Aircraft Electric Power Requirements

An aircraft electric power system consists of:

- A main power source;
- Emergency power source;
- Power conversion equipment;
- Control and protection devices;
- An interconnection network (wires, cables, connectors, etc.).

The main electrical power source comes from generators which are driven by the aircraft propulsion engines. Emergency power comes from batteries, engine bleed air, independent auxiliary power units, ram air driven generators, or hydraulically driven generator.

2.3.2.1 AC Power Characteristics

The AEPS must provide electrical power grounded single or three-phase systems. In the VSCF topology, the nominal voltage shall be $115/200V$, $400Hz$. VSVF systems have frequencies varying from 360 to $800Hz$ at $115/200V$. There are systems called double-voltage, which have nominal voltages of $230/400V$, $400Hz$.

The normal operation characteristics have severe limits that apply to under voltage, voltage transients and frequency transients for both, $400Hz$ systems and variable frequency systems, as shown in Table 2.1 and 2.2.

The rate of change of frequency from onset of a normal frequency transient measured for over a period of time of greater than 25 milliseconds shall not exceed $250Hz$ per second. In abnormal operation, the over frequency and under frequency for variable frequency systems shall not exceed the $360 - 800Hz$ steady state values. The rate of change of frequency from onset of a abnormal frequency transient measured for over a period of time of greater than 25 milliseconds shall not exceed $500Hz$ per second.

Table 2-1: AC normal operation characteristics - 400 Hertz

Steady state characteristics	Limits
Steady state voltage	108.0 to 118.0 Volts, RMS
Voltage unbalance	3.0 Volts, RMS maximum
Voltage modulation	2.5 Volts, RMS maximum
Voltage phase difference	116° to 124°
Distortion factor	0.05 maximum
Distortion spectrum	Figure 2-14
Crest factor	1.31 to 1.51
DC component	+ 0.10 to - 0.10 Volts
Steady state frequency	393 to 407 Hz
Frequency modulation	4 Hz

Table 2-2: AC normal operation characteristics - variable frequency

Steady state characteristics	Limits
Steady state voltage	108.0 to 118.0 Volts, RMS
Voltage unbalance	3.0 Volts, RMS maximum
Voltage modulation	2.5 Volts, RMS maximum
Voltage phase difference	116° to 124°
Distortion factor	0.05 maximum
Distortion spectrum	Figure 2-14
Crest factor	1.31 to 1.51
DC component	+0.10 to – 0.10 Volts
Steady state frequency	360 to 800 Hz
Frequency modulation	4 Hz

Frequency	Distortion Amplitude, dBV	
	400 Hz	VF
10	-10.00	-10.00
100	-10.00	-10.00
1,000	10.00	10.00
3,000	10.00	10.00
6,000	4.00	10.00
500,000	-34.44	-24.44
1,000,000	---	-34.44
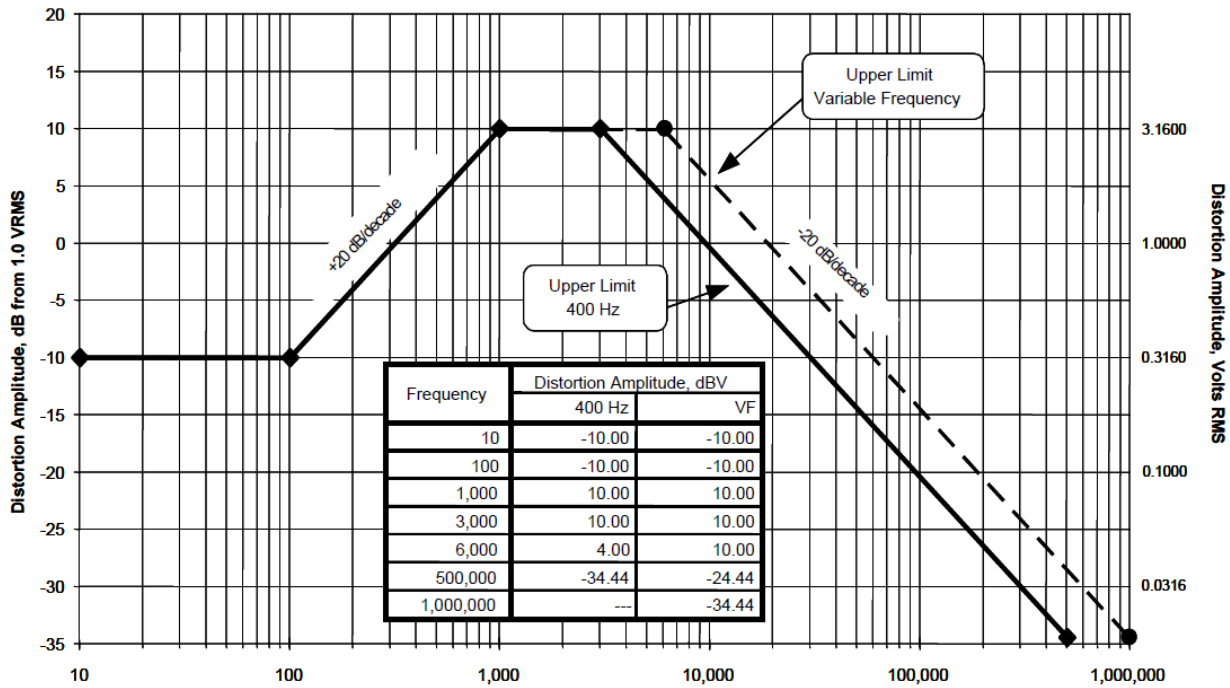
Figure 2-14: Maximum distortion spectrum of 400 Hz and variable frequency AC voltage. [22]

Figure 2-14 shows that the harmonic limits are very severe in AEPS. The curve shows that the spectral components must be lower than $0.31V$ RMS in some low frequencies, and even lower in high frequencies. It is important to notice that as the system frequency varies, the frequency of the harmonics varies as well. Note that in both $400Hz$ and variable frequency systems the distortion factor so called Total Harmonic Distortion (THD) must be less than 5%.

2.3.2.2 Voltage and Frequency Transients

The AEPS is very susceptible to transients which occur as result of normal disturbances such as electric load engine speed changes. Figure 2-15 shows the limits of AC voltage transient while Figure 2-16 shows the limits of frequency transient.
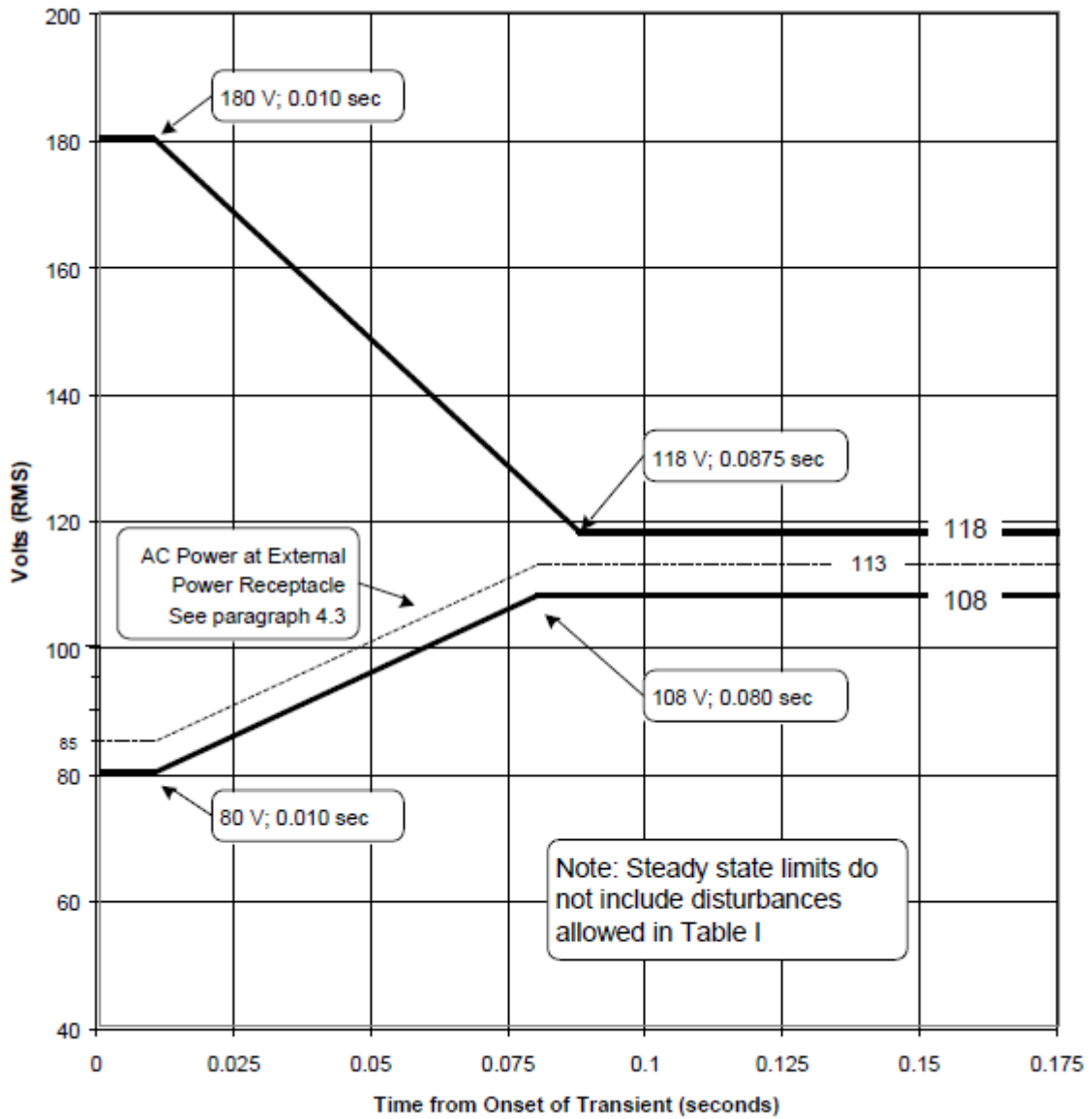
Figure 2-15: Envelope of normal 400Hz and variable frequency AC voltage transient. [22]
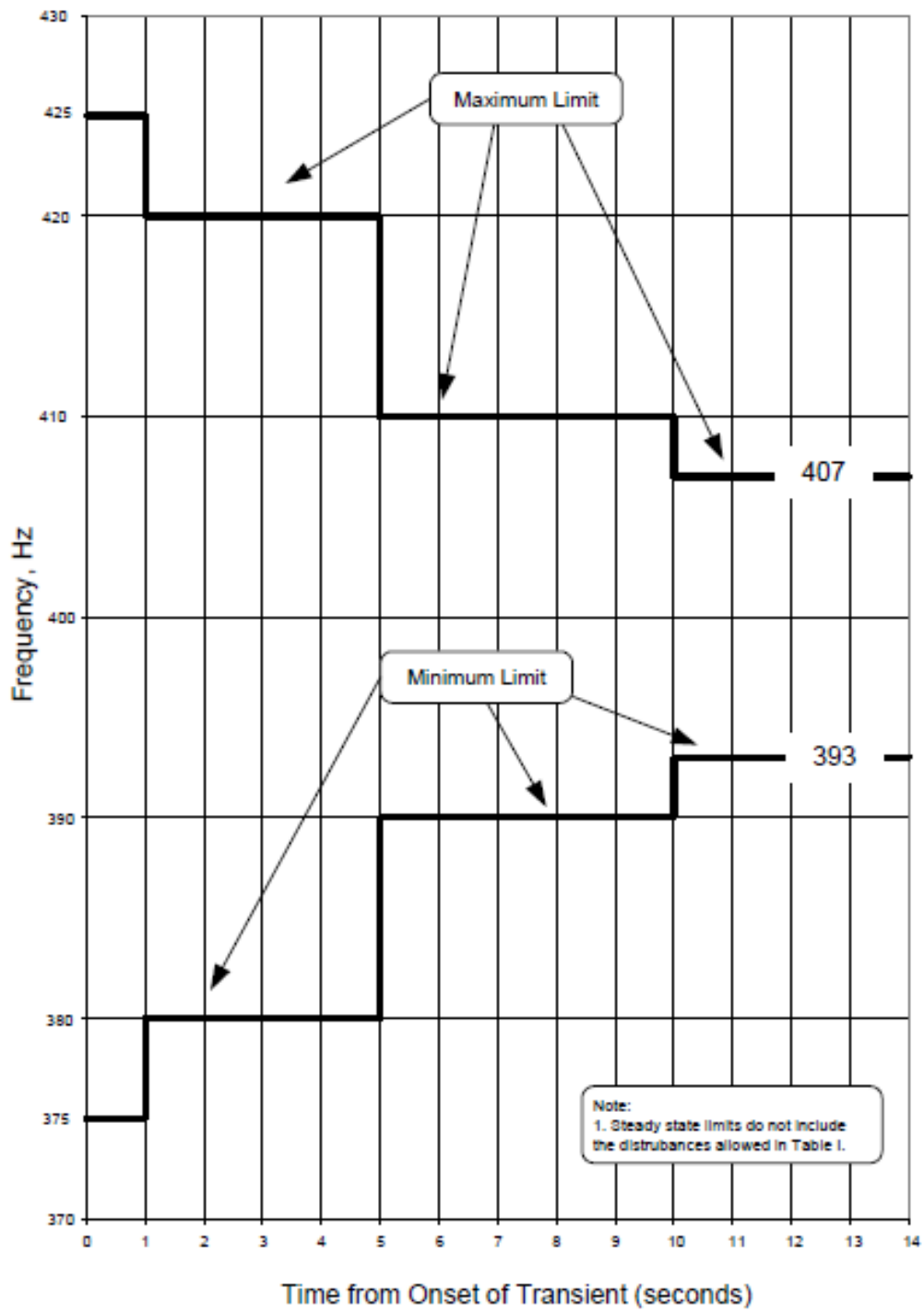
Figure 2-16: Envelope of normal 400Hz AC frequency transient. [22]

2.3.2.3 Load Characteristic

When operating in either normal or abnormal conditions, the load unbalance of equipment exceeding $30kVA$ shall not exceed 3.33 % of the total three-phase load [22].

Power factor of AC equipment greater than $500VA$ shall be between 0.85 lagging and unity when operating at 50 percent or more of its rated load current in steady state condition. AC equipment shall not have leading power factor when operating at more than $100VA$.

Attention must be given to non-linear loads and their effect on the AC power bus. All loads should not introduce excessive current distortion such that other equipment is affected.

The equipment chassis shall not be used for power returns, all electrical power input terminals, including AC neutral and DC negative terminals, shall be electrically isolated from case ground.

2.3.2.4 Compatibility of Equipment

To use equipment in AEPSs, system testing should be performed as in MIL-HDBK-704-1 through -8. Each component and subsystem is designed and tested to its individual equipment specification, which often requires tighter performance than does MIL-STD-704 to compensate for the effects of loads as well as the associated feeder/line voltage drops therein. The limits specified in MIL-HDBK-704-1 thought 8 are minimum requirements for specifying that utilization equipment is compatible with aircraft electrical power.

2.3.2.5 RTCA/DO-160 Testing

RTCA/DO-160 [28] is a set of standard procedures and environmental test criteria for testing airborne equipment for the entire spectrum of aircraft from light general aviation aircraft and helicopters.

Section 16 of this standard defines test conditions and procedures for ac and dc electrical power applied to the terminals of the equipment under test. It covers the following electrical power supplies:

- $14V$ DC, $28V$ DC and $270V$ DC
- $115V$ RMS ac and $230V$ RMS ac at either a nominal $400Hz$ frequency or over a variable frequency range which includes $400Hz$.

Section 16.7 delimits the load equipment influence on AEPS (AC and DC). This test designation relates to AC equipment with an individual maximum power consumption greater than $35VA$ or installations where the combined power consumption of multiple units (of the same equipment type) is greater than $150VA$.

According to this section:

1) **Voltage Distortion:** If the Equipment Under Test (EUT) power is greater than $2kVA$, the THDv may be greater than 1.25 % but shall not exceed 4 %.

2) **Current Distortion:** The equipment shall not demand harmonic currents greater than 1.25% above that already specified in Table 2-3 for every 1% of distortion in the corresponding individual voltage harmonic.

Table 2-3: Current Harmonic Limits for Balanced Three-Phase Electrical Equipment

Harmonic Order	Limits
3rd, 5th, 7th	$I_3 = I_5 = I_7 = 0.02\ I_1$
Odd Triplen Harmonics (h = 9, 15, 21, ..., 39)	$I_h = 0.1\ I_1\ /\ h$
11th	$I_{11} = 0.1\ I_1$
13th	$I_{13} = 0.08\ I_1$
Odd Non Triplen Harmonics 17, 19	$I_{17} = I_{19} = 0.04\ I_1$
Odd Non Triplen Harmonics 23, 25	$I_{23} = I_{25} = 0.03\ I_1$
Odd Non Triplen Harmonics 29, 31, 35, 37	$I_h = 0.3\ I_1\ /\ h$
Even Harmonics 2 and 4	$I_h = 0.01\ I_1\ /\ h$
Even Harmonics > 4 (h = 6, 8, 10, ..., 40)	$I_h = 0.0025\ I_1$

I1 =   maximum fundamental current of the equipment that is measured during the maximum steady-state power demand operating mode condition, at a single test frequency (*).

This maximum current shall be used to calculate the current harmonic limits for all modes of operation, at that test frequency.

h =   order of harmonic.

Ih =   maximum harmonic current of order h obtained for all normal steady state modes of operation.

3) **Power Factor:** For AC load equipment other than motors the power factor shall be equal or higher than the values listed in Table 2-4. For loads with a maximum total power consumption of all similar equipment on the airplane greater than 150VA, the steady-state full load power factor for each load shall be between 0.8 lagging and 0.968 leading.

Table 2-4: Power Factor Limits to AC load equipment

Load (kVA)	Power Factor - Leading	Power Factor - Lagging
≤ 0.02	0.200	0.200
0.03	0.355	0.321
0.04	0.464	0.406
0.06	0.619	0.527
0.08	0.728	0.613
0.10	0.813	0.679
0.15	0.968	0.800
Larger than 0.15	0.968	0.800

- The leading PF between 0.02 kVA and 0.15 kVA is given by:

$$PF = 0.87765 * log(kVA) + 1.69110$$

- The lagging PF between 0.02 kVA and 0.15 kVA is given by:

$$PF = 0.68567 * log(kVA) + 1.36493$$

4) **Phase Unbalance:** The apparent (VA), real (W) and reactive (var) power demands of any phase of a three-phase load shall not differ from similar power demands of any other phase, during any normal operating mode, by more than the limits of Figure 2-17.

Figure 2-17: Allowable Phase Unbalance for Three Phase AC Loads [28]

2.4 STATE OF ART OF AERONAUTICAL ACTIVE POWER FILTERS

As pointed in the previous sections, the use of non-linear electrical loads is becoming a great challenge to the aircraft power distribution. This scenario leads to the introduction of AAPFs into the aircraft power system to improve its power quality and overall reliability.

The application of these techniques in the avionic scenario presents many issues mainly related to the current AEPS fundamental frequency of $400Hz$ when in steady-state. The latest airplane power networks uses a VSVF generation, which results in fundamental frequency varying between $360Hz$ and $800Hz$ due to the speed variations of the turbine. An AAPF is considered an effective device to compensate power networks quality deviation; however for the AC airplane power system harmonics between the whole frequency ranges should be compensated.

2.4.1 State of Art of AAPFs

Recently, efforts have been made to design and implement AAPF using advanced control techniques and devices in order to comply with the standards.

2.4.1.1 Nanjing University of Aeronautics and Astronautics

Nanjing University has placed a lot of time and efforts in finding an optimum AAPF. In 2010, researchers from Nanjing University proposed an AAPF [29] based on analyzing and updating two core functions of APF: current reference generation module and current tracking module for source current direct control strategy. A cascaded inverter topology was applied; Figure 2-18 illustrates the proposed system.
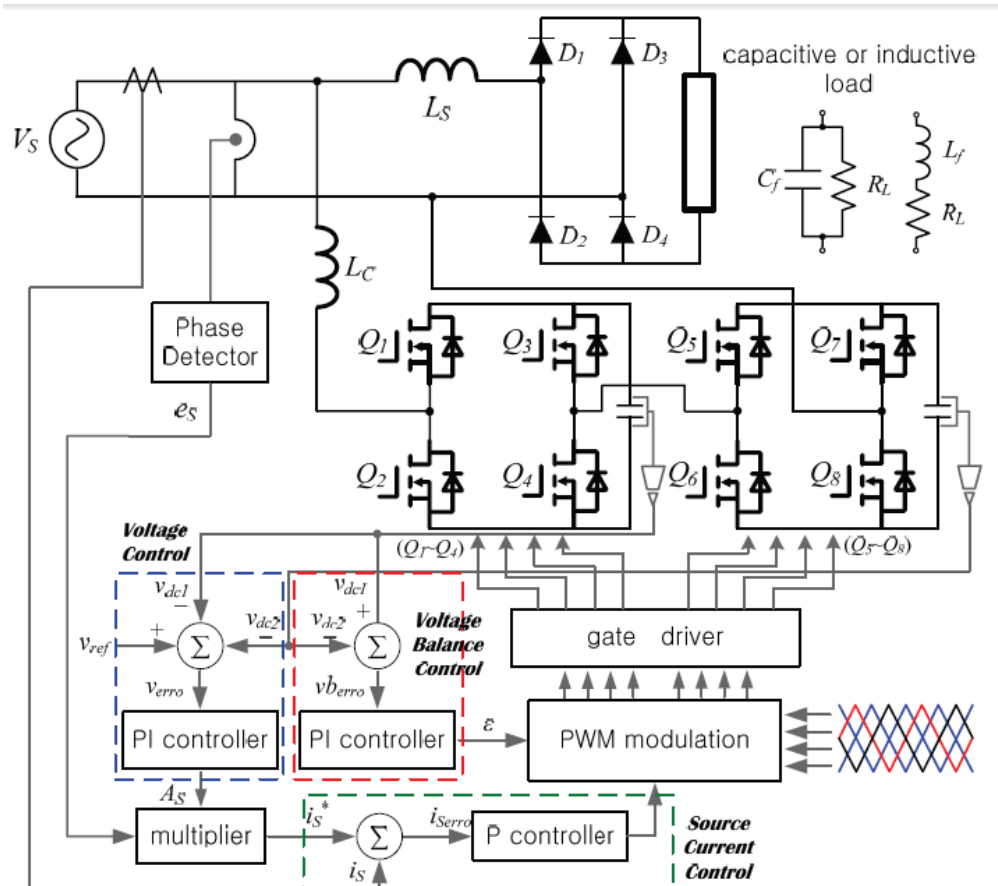
Figure 2-18: Single Phase System Diagram of AAPF. [29]

33

The prototype achieved good compensation performance; however the source current THD decreased from 167% to 6%, not complying with the military standards [22]. The AAPF was enhanced in 2011 [30] and in 2012 by [31] and [32].

The same group presented different topologies, concentrating in DSP implementations [33], [34]. The proposed method focused in overcoming the DSP computation resources when executing the control system by rearranging the computation elements, based on their different requirements of control bandwidth.

2.4.1.2 The University of Nottingham

In 2009, researchers from the Nottingham University proposed a five-level active shunt power filter (ASF) structure with a predictive current controller, power systems with variable frequency (ranging from 360Hz to 800Hz) [35]. This ASF was able to track current harmonics with low switching frequency. The proposed high bandwidth, two-steps ahead predictive current controller is shown in Figure 2-19.
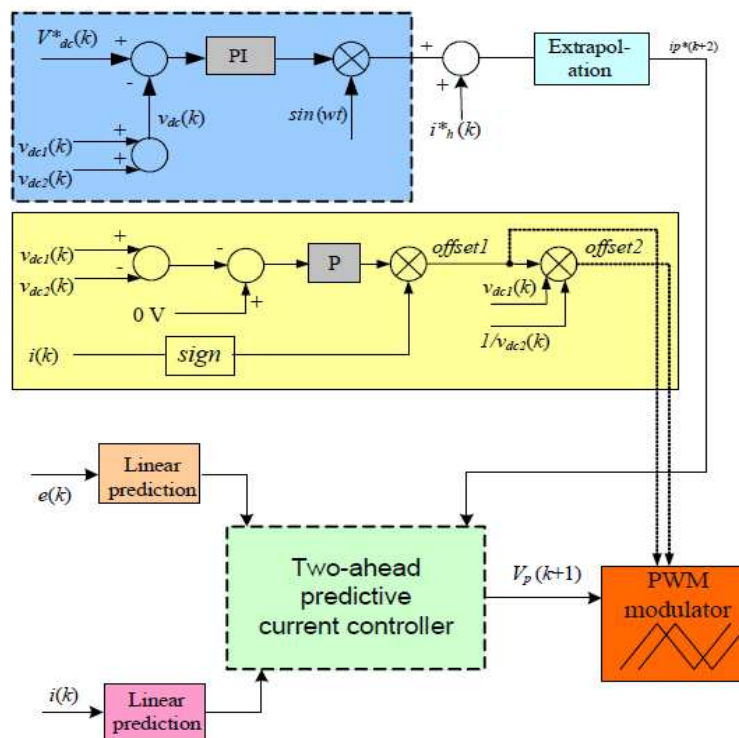
Figure 2-19: Control strategy of ASF. [35]

34

The system was tested in simulation for the fundamental, 5th and 7th harmonic current components compensation. However, this solution may not filter higher order harmonics. Therefore, the AEPS may not comply with the MIL-STD 704 in some load configurations. The AAPF was enhanced in 2010 [36] and finally proposed a multilevel topology in 2013 [37]. The novel modulation technique provided a 50% reduction of the converter switching frequency. Another control technique based on Iterative Learning Control [38] was used.

2.4.1.3 University of Campinas

In 2013, the Laboratory of Power Conditioning of University of Campinas, presented the design of a multilevel active power filter for more electric airplane variable frequency systems [39]. The system overview is shown in Figure 2-20.
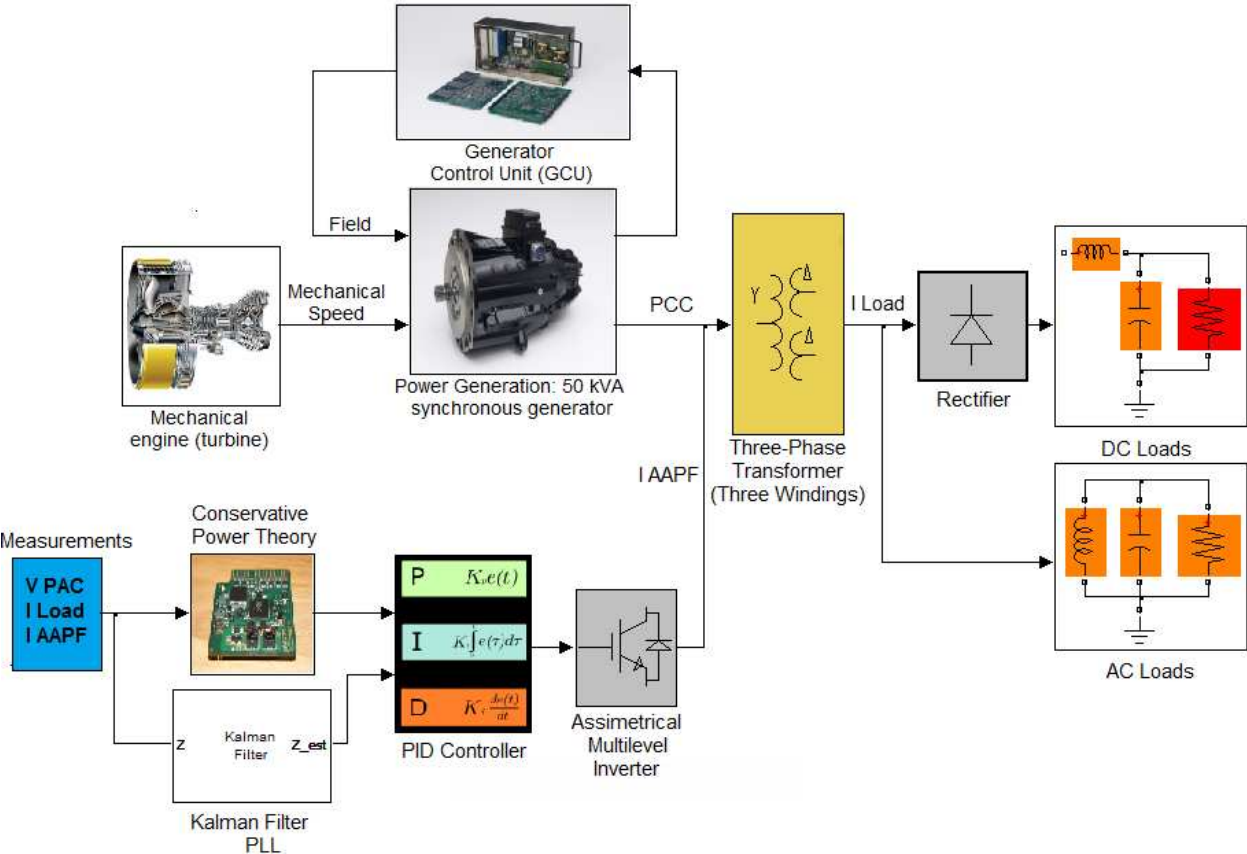
Figure 2-20: System overview of Multilevel Active Power Filter for for Aircrafts [39]

This work has described the use of an Aeronautical Active Power Filter for aircraft power networks where the frequency varies between $400Hz$ and $800Hz$. The system requires robustness and the ability of compensating harmonics at a very high frequency. Therefore it has been optimized with an asymmetrical multilevel voltage source converter employing the CPT. The control system uses a Kalman Filter Phase-Locked Loop (KF-PLL) to synchronize to the grid. After analyzing accurate simulation results, it can be concluded that the proposed active filter control has proved to be very effective for mitigation of current harmonics on aircraft power grids, achieving good dynamics with a reasonable switching frequency. In simulation, the proposed AAPF is was helpful to make the AEPS comply with the MLI-STD 704.

2.4.1.4 Different Resources

In 2010, researchers from South Valley University, Aswan, Egypt proposed and designed a fully controlled active power filter to regulate the load terminal voltage, eliminate harmonics, correct supply power factor, and minimize the effect of unbalanced loads [40]. The control algorithm for the active power filter (APF) is tuned for cancelation of all harmonics. The proposed APF is integrated into the model of a $90kVA$ advanced aircraft electric power system under VSCF operation as illustrated in Figure 2-21.
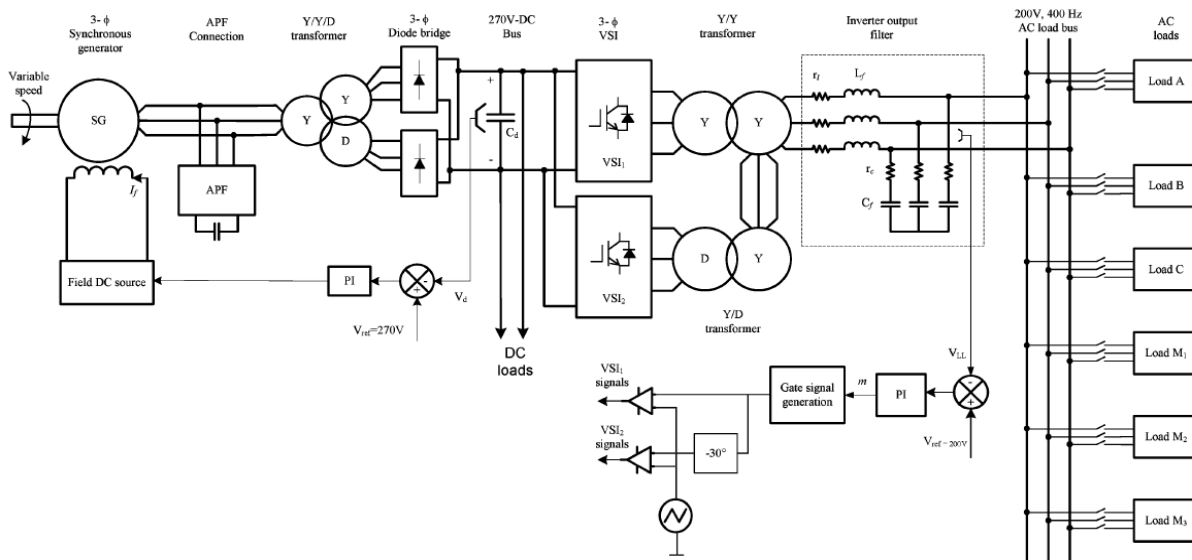
Figure 2-21: Modeled VSCF aircraft electric power system with the APF, inverter passive filter, main loads, and controllers. [40]

For the full compliance with the respective harmonics standards, unbalance elimination, and reactive power compensation, the total harmonic cancellation was applied for the control strategy, which is capable of compensation under all conditions, Figure 2-22.
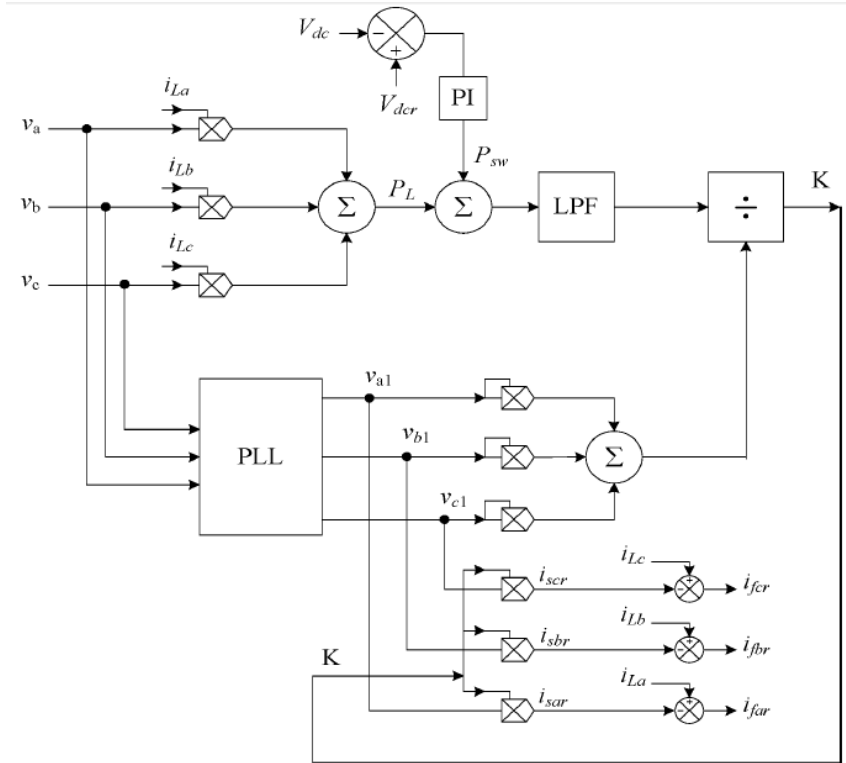
Figure 2-22: PHC control method. [40]

The performance characteristics of the system are studied with the frequency from 400 Hz to 800 Hz under different loading conditions. Several cases studies are presented including DC loads as well as passive and dynamic AC loads. According to the author, the power-quality characteristics of the studied VSCF aircraft electric power system with the proposed active filter are shown to be in compliance with the most recent military aircraft electrical standards [22] as well as with the popular IEEE-Std. 519. However the authors make use of a three-phase inverter that can lead to issues related to high switching frequencies.

In the same year, University of Padova and University of Nottingham presented [41], which investigates an adaptive current controller to compensate selected load current harmonics, however, the focus was on the compensation at a supply frequency of $800Hz$, where the 5th harmonic is at $4kHz$ and the 7th is at $5.6kHz$.

2.5 PROPOSED SOLUTION

Based on the previous sections, it is evident that harmonic distortion and low power factor should be avoided in AEPS. The state of art of AAPF shown previously, reinforces that the use of multilevel inverters is a trend, as well as the use of advanced control techniques.

In this work, an AAPF is shunt connected to an aircraft grid and normally placed close to the power generators. To begin the research, an aircraft system model is built in Matlab/Simulink. Each relevant part is modeled and an enhanced AAPF is proposed in order to overcome the challenges reported in the last sections. The overall system overview is shown in Figure 2-23.
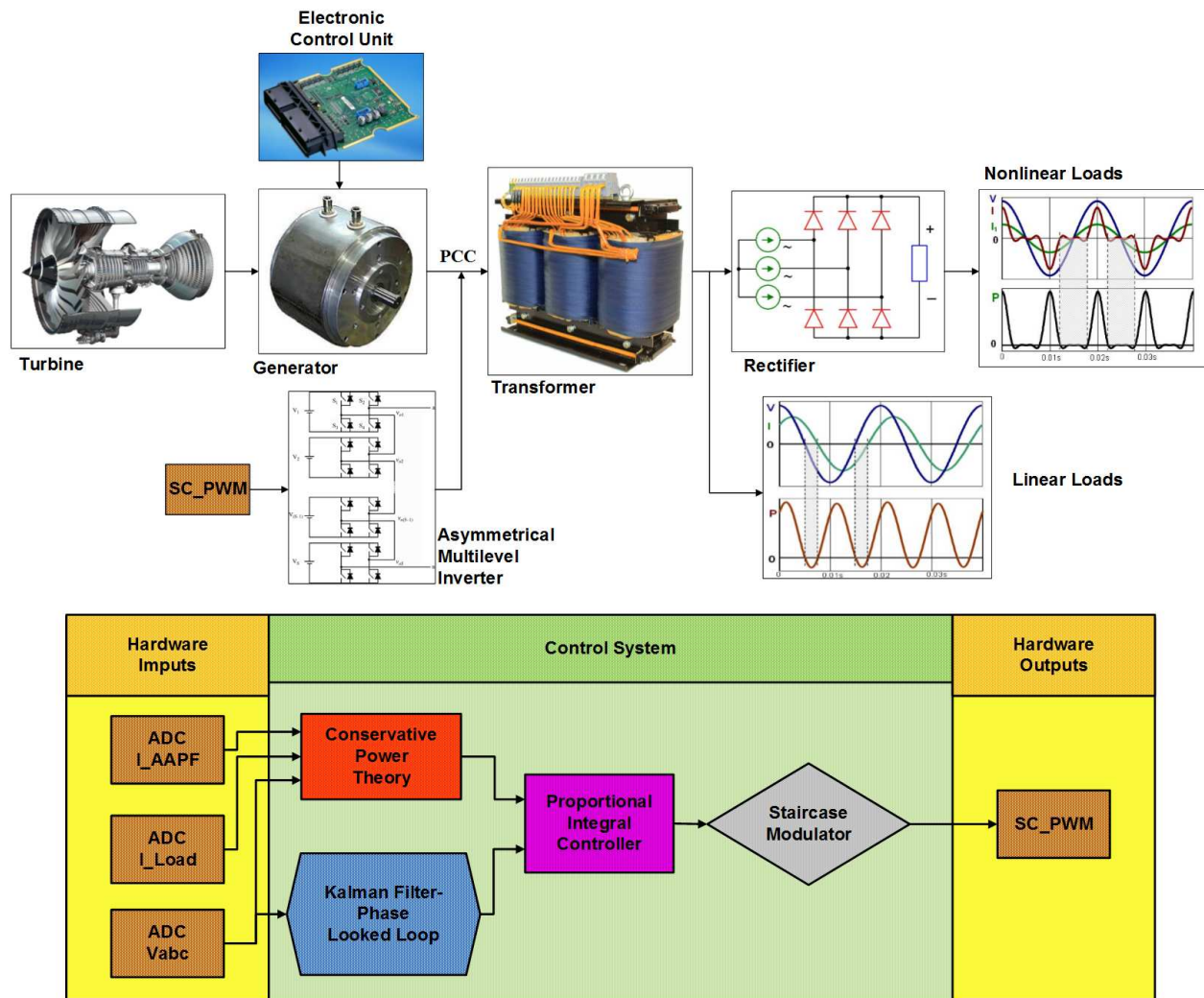
Figure 2-23: Proposed System Overview

In the above system, a three phase transformer was placed and the loads were modeled as DC Loads (such as the 540 and 28 VDC systems) and AC Loads (induction machines, resistive loads and brushless motors). The mechanical turbine is modeled by a simple signal builder, which determines the mechanical speed of the shaft, which drives the synchronous generator. The Generator Control Unit (GCU) regulates the generator voltage to 230 volts. The Conservative Power Theory (CPT) [7] is used to obtain the reference currents, moreover, this theory was proved to be very robust since it is valid even when the source voltages and currents are non-sinusoidal. A Kalman Filter-Phase Locked Loop (KF-PLL) [42] was chosen due to its highly accurate and fast estimation of grid frequency and phase angle. An Asymmetrical Multilevel Inverter (AMI) was used due to certain characteristics, such as, reduced switching power loss, low output filter requirements, and high power quality.

3 SYSTEM MODELLING

In the last section the most important topologies of More Electric Aircraft (MEA) were shown. In the electrical system field, the standards bring severe limitations related to harmonic distortion. The development of Aeronautical Active Power Filters (AAPFs) is an attractive solution for the compliance of the Aircraft Electrical Power Systems (AEPS) with the requirements. However, the AEPS characteristics (high nominal frequency and high speed variable frequency) render the development of these techniques to be a great challenge. In this section, the proposed AAPF is modelled and simulations are shown to validate the digital implementation.

3.1 SYNCHRONIZATION IN MEA

The application of AAPFs techniques in the avionic scenario presents many issues mainly related to the high steady state fundamental frequency ($400Hz$) of the Aeronautical Electric Power Systems (AEPSs). The latest airplane power networks use a Variable Speed Variable Frequency (VSVF) configuration, which results in fundamental frequency varying between $360Hz$ and $800Hz$ due to the turbine speed variations, such as the Boeing 787 architecture.

Due to the field of application, severe standards are applied for utilization of equipment in compliance to aircraft electrical power characteristics. The life risk that a device can represent during failure or abnormal operation highlights the need of high accurate and advanced control techniques. Synchronization with the AC grid voltages is one of the keys for the good operation of some electronic devices, such as controlled rectifiers, AC-AC converters and active filters. This factor propelled the enhancement of Phase-Locked Loop (PLL) techniques. PLL is a circuit (or algorithm) responsible for producing an output signal synchronized with the frequency of the input signal.

There are several straightforward PLL methods; however, when applied to electrical power signals, they suffer from the presence of power quality deviations, such as harmonics [43], and unbalanced utility conditions [44]. Moreover, in aircraft VSVF power grids, the fast frequency variations turn most PLL algorithms inapplicable and traditional solutions for unbalance and harmonics improper.

Different methods were proposed lately for power grid synchronization. As a remark, in [45] a comparative study of three methods is presented; the PLL, the Recursive Discrete Fourier Transform (RDFT) and the Kalman filter Phase-Locked Loop(KF-PLL). None of the above techniques has been tested for high fundamental frequencies, or under severe frequency deviations, therefore they cannot be extended to aircraft grid frequency estimation without consistent testing and demonstrations.

This section addresses these issues and proposes a robust solution based on KF-PLL. The algorithm will be validated by model/software and processor in the loop simulations. Attention has been given to the virtual modeling of the different software levels in order to make the simulations closer to reality. The control algorithm was optimized and tested in a DSP of Texas Instruments, respecting ADC time conversion, memory, as well as CPU processing and actuation time. Moreover, the simulations were developed in Matlab/Simulink. A fixed-step discrete solver was chosen to reflect a real embedded micro-controller unit.

3.1.1 Kalman Filter-Phase Locked Loop

An AAPF is shunt connected to the AEPS. The control algorithm requires the measurement of the three phase voltages in the Point of Common Coupling (PCC), which are used by the PLL for phase extraction. For simulation purposes, a comprehensive model of the AEPS was built in Matlab/Simulink. A Three-Phase Programmable Voltage Source (PVS) was placed to simulate a Permanent Magnet Synchronous Generator, which is driven by a turbine in a real system. The frequency variations of the generator, due to the turbine accelerations, are programmed in the PVS. The distribution system was simplified by a three-phase transformer, DC and AC loads, which are the most predominant electrical loads in an AEPS. Figure 3-1 shows the system overview.
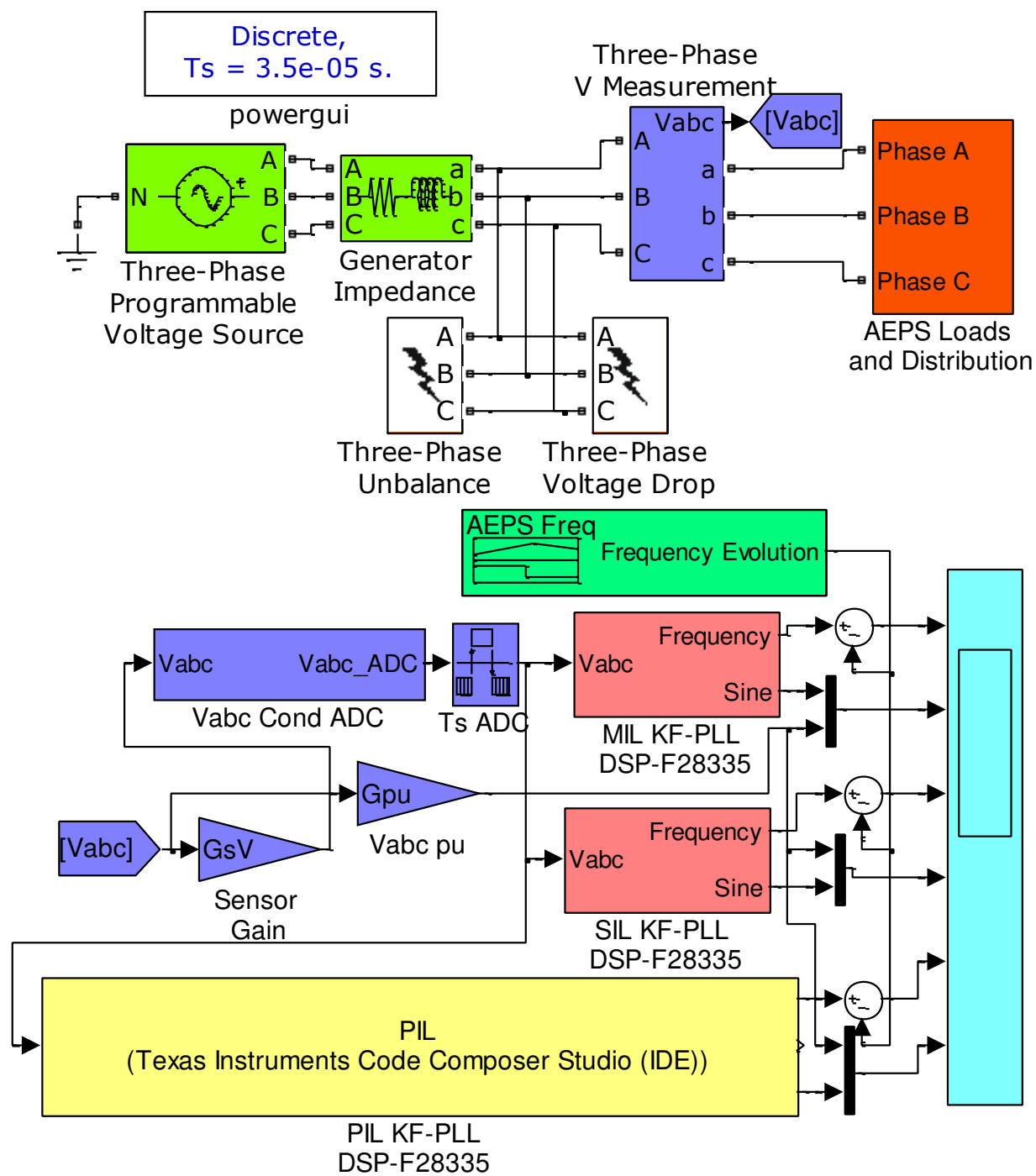
Figure 3-1: KF-PLL System Overview

The voltages are sensed by the "Three Phase VI Measurement" block. "Sensor Gain" is
applied to simulate a Hall sensor gain. The block "Vabc Cond ADC" implements the operations of

the TMS320F28335 DSP analogic-digital converter (ADC). The results are 12 bits words, which are used by the block "KF-PLL DSP-F28335". The block "MIL KF-PLL DSP-F28335" implements a model based design of a PLL preceded by a Kalman estimator-based filter, called Kalman Filter-Phase Locked Loop (KF-PLL) [42] that provides a highly accurate and fast estimation of grid frequency and phase angle. This algorithm is robust to several perturbations, such as harmonics, voltage unbalance, measurement noise, three-phase faults and frequency variations that may occur in the aircraft power system.

Furthermore, the blocks "SIL KF-PLL DSP-F28335" and "PIL KF-PLL DSP-F28335" are setups for Software in the Loop (SIL) and Processor in the Loop (PIL) simulations respectively. These steps are extremely important to validate the design of digital control algorithms for embedded applications. The SIL and MIL simulations are used to validate generated code. The SIL runs the generated code implemented into the MIL subsystem, this code runs into Simulink. The PIL is a setup to run the generated code into a real time TMS320F28335 microprocessor.

3.1.2 Kalman Filter-Phase Locked Loop Algorithm

The Kalman filter is well known due to its ability to deal with linear systems corrupted by uncertainties in the states of the plant, as well as measurement noise. The spectrum of this type of noise is usually distributed over a wide frequency range, which can be modeled as white noise [46]. Since the Kalman filter considers this type of perturbation, it is highly indicated to be used in PLL systems. Figure 3-2 details the block "KF-PLL DSP-F28335" of Figure 3-1.
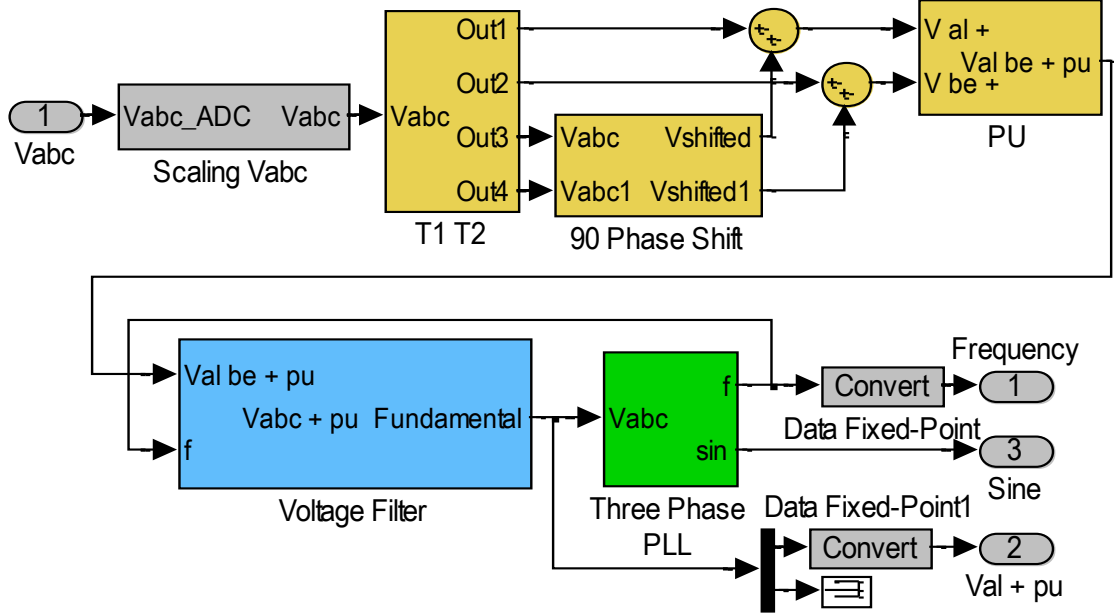
Figure 3-2: KF-PLL Control System

The block "Scaling $Vabc$" makes the scaling of the ADC output to real world values. The functionality of the other blocks is detailed in the next section. The block "Voltage Filter" implements the Kalman filter model [47].

3.1.2.1 Kalman Filter Model

As discussed in [42], considering a discrete linear dynamic stochastic system modeled by (3-1).

$$\begin{cases} x_{k+1} = A_k \cdot x_k + B_k \cdot \gamma_k \\ \quad y_k = C_k \cdot x_k + \vartheta_k \end{cases} \tag{3-1}$$

where γ_k and ϑ_k are Gaussian white noise, which have average values and covariances given by (3-2).

$$E\{\gamma_i \cdot \gamma_j{}^T\} = Q_i \cdot \delta_{ij}; \ E\{\vartheta_i \cdot \vartheta_j{}^T\} = R_i \cdot \delta_{ij} \tag{3-2}$$

where δ_{ij} denotes the Kronecker Delta function.

Based on the above definition, the model that adequately represents the grid voltage dynamics in the alpha-beta frame, following (3-1), is (3-3).

$$\begin{cases} \begin{bmatrix} v_\alpha \\ v_\beta \end{bmatrix}_{k+1} = \begin{bmatrix} \cos(\omega_k \cdot T_s) & \sin(\omega_k \cdot T_s) \\ -\sin(\omega_k \cdot T_s) & \cos(\omega_k \cdot T_s) \end{bmatrix}_k \cdot \begin{bmatrix} v_\alpha \\ v_\beta \end{bmatrix}_k + \begin{matrix} \gamma_1 \\ \gamma_2 \end{matrix} \\ y_k = \begin{bmatrix} 1 & 0 \end{bmatrix} \cdot \begin{bmatrix} v_\alpha \\ v_\beta \end{bmatrix}_k + \vartheta_k \end{cases} \tag{3-3}$$

Where v_α and v_β represent the Clarke's transformation of three-phase v_{abc} voltages; ω_k is the angular frequency and Ts is the sampling time.

The harmonics are not included; they will be considered perturbations and in this sense, will be modeled by the measurement and process noises.

It is observed that ω_k is the only variable that depends on the frequency. If a frequency variation in the input signal happens, it leads to changing the elements of matrix A, if "Ts" is kept constant. In order to make the KF immune to these disturbs, the identification of ω_k is essential. Updating this variable accordingly to the frequency deviations can handle the Kalman filter algorithm immune to frequency variations. This characteristic enables the Kalman filter to be used to AEPS phase estimation, since the frequency of these systems varies continuously.

By means of the above definition, it is possible to define a Kalman Filter to the system of (3-3). The state estimation "$\widehat{v_\alpha}$" based on measurements "y_k", is achieved in two parts: a prediction step and a correction step, as shown in Table 3-1. The first step estimates the state ahead and gets the error covariance ahead. The second one computes the Kalman gain, update the estimation with measurement and update the error covariance [45].

Table 3-1: Kalman Filter Description

Prediction	Correction
1 – Project the State Ahead $$\widehat{x}_{k/k-1} = A \cdot \widehat{x}_{k-1}$$	3 – Compute the Kalman Gain $$K_k = P_{k\|k-1} \cdot B_k^T \cdot \left(B_k \cdot P_{k\|k-1} \cdot B_k^T + R_k \right)^{-1}$$
2 – Project the Error Covariance ahead $$P_{k/k-1} = A \cdot P_{k-1} \cdot A^T + Q$$	4 – Update estimate with measurement $$\widehat{x}_k = \widehat{x}_{k\|k-1} + K_k \cdot \left(y_k - B_k \cdot \widehat{x}_{k\|k-1} \right)$$ 5 – Upadate the error covariance $$P_k = (I - K_k \cdot B) \cdot P_{k\|k-1}$$

Where:

- **A** – system matrix
- **B** – input matrix
- **Q** - process noise covariance,
- **R** - measurement noise covariance,
- $\widehat{x}_{k/k-1}$ - initial estimation error,
- $P_{k/k-1}$ - estimation covariance error,
- $x_k - \widehat{x}_k$ - final estimation error,
- P_k - final estimation error covariance and
- K_k **-** Kalman gain.

The filtering characteristics and the convergence speed of the filter depends on the measurement noise and process noise. When the measurement noise **R** is high, the convergence is slow, alternatively when the measurement noise is small; it is assured a better confidence in y_k and a fast dynamic response. When the process noise **Q** is high, the results are a large reliability of y_k in the next estimation step. If the process noise is small, resulting in a slow convergence of the algorithm. Therefore, the Kalman Filter design depends on the balance between the choice of matrices **Q** and **R**, considering input waveform distortions and desired output.

In the software development, based in the initial state $\widehat{x}_{k|k-1}$, the error $P_{k|k-1}$ is predicted. K_k is calculated and the estimated value $\widehat{x}_k$ is obtained. Finally, the error P_k is corrected and the process restarts.

A successful approach for selecting R is to consider the noise as white and Gaussian and to use standard methods to determine its variance. Although **Q** is not evident to be defined, the cleverest way is to remember that small values of **Q** increase the filter performance. On the other hand, small values can generate output states with modeling errors, such as phase delays.

The above method was implemented in Matlab/Simulink and the Kalman estimator was tuned to $diag(Q) = 0.01$ and $R = 20$, based on [48].

The Matlab code developed to implement the Kalman Filter is shown in Appendix A.

3.1.3 Positive Sequence Identification

The KF-PLL must provide a signal in phase with the positive sequence, fundamental component of the grid voltage. Given the phase voltages, the positive α, β (pu) components of the voltages v_{abc} can be obtained throughout (3-4), which is the association of Clarke's and Fortescue's transformations [42]:

$$v_{\alpha\beta}{}^+ = T_1 \cdot v_{abc} + T_2 \cdot b \cdot v_{abc} \tag{3-4}$$

where,

$$\begin{cases} T_1 = \sqrt{\dfrac{2}{3}} \cdot \begin{bmatrix} 1/2 & -1/4 & -1/4 \\ 0 & \sqrt{3}/4 & -\sqrt{3}/4 \end{bmatrix} \\[2em] T_2 = \sqrt{\dfrac{2}{3}} \cdot \begin{bmatrix} 0 & \sqrt{3}/4 & -\sqrt{3}/4 \\ -1/2 & 1/4 & 1/4 \end{bmatrix} \end{cases}$$

and, $b = e^{j90°}$ is a 90° phase shift operator,

From Figure 3-2, the blocks "T1 T2" and "90 Phase Shift" implements (3-4) and the block "PU" calculates the normalized per unit values. The positive sequence voltages $v_{\alpha\beta}{}^+$ are applied to the Kalman filter to extract the harmonics and obtain the fundamental component, which is applied to a classical PLL for the extraction of the phase and frequency. The diagram of the classical PLL is showed in Figure 3-3.
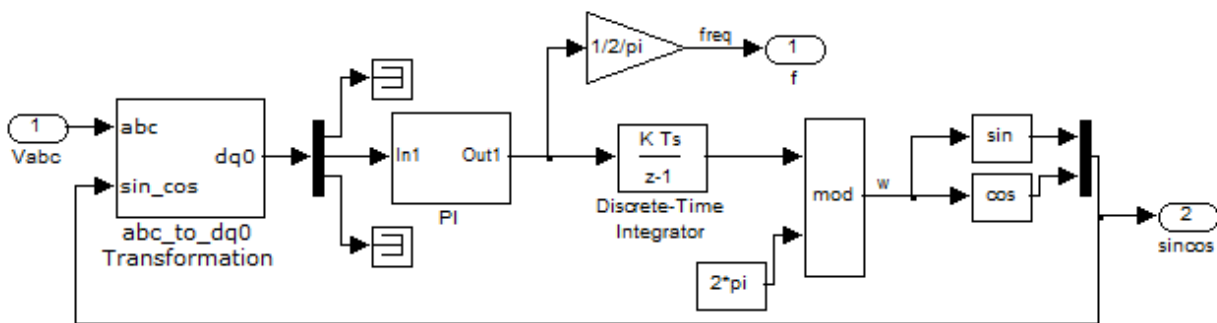

Figure 3-3: Classical PLL

3.1.4 Simulations and Experimental Results

The simulation by Model in the Loop (MIL) and Software in the Loop (SIL) validates the code implemented in a real time microprocessor TMS320F28335 throughout Code Composer Studio (CCStudio). The MIL simulation, refers to the simulation with Simulink blocks. On the other hand, the SIL simulation, refers to the simulation of the software generated by the MIL.

The algorithm execution time was $27.8 \, \mu s$. However for PIL simulation some optimized settings from Code Composer Studio (CCStudio) are not supported by Simulink, therefore the execution time (fixed-step size) was set to $35 \, \mu s$.

In order to demonstrate the algorithm dynamic response in the presence of the perturbations that can occur in the AEPS, the following sequence of events is applied:

1. Between $t = 0 \, s$ and $t = 1 \, s$ the system frequency is $360Hz$. Yet, a component with 15% of the fundamental supply voltage is added at the 11th order harmonic between t $= 0.4$ s and $t = 0.6 \, s$. Furthermore, a voltage unbalance of 45.5% was applied to the phase "c" between $t = 0.7 \, s$ and $t = 0.9 \, s$.

2. A $500Hz/s$ frequency transient simulate abnormal conditions, discussed in [22]. It is placed between $t = 1 \, s$ and $t = 2.08 \, s$. At this moment the frequency of the electrical system reaches $900Hz$.

3. Finally, from $t = 2.3 \, s$ to $t = 2.5 \, s$, a 99.0% voltage drop is inserted, reducing the peak value to 2 volts.

This sequence of events proves the KF-PLL robustness to harmonics, unbalance, frequency variations, and voltage sags. Table 3-2 contains the parameters of the simulated AEPS of Figure 3-1. Figure 3-4 shows the load setup of the simulation.

Table 3-2: Parameters of the System

Voltage Source	Parameters
Line Voltage	$230V\ RMS$
Internal resistance and inductance	$R = 0.0204\Omega;$ $L = 0.08104mH$
Line Impedance	$300\mu H$
Load Power	
DC	$5kW$
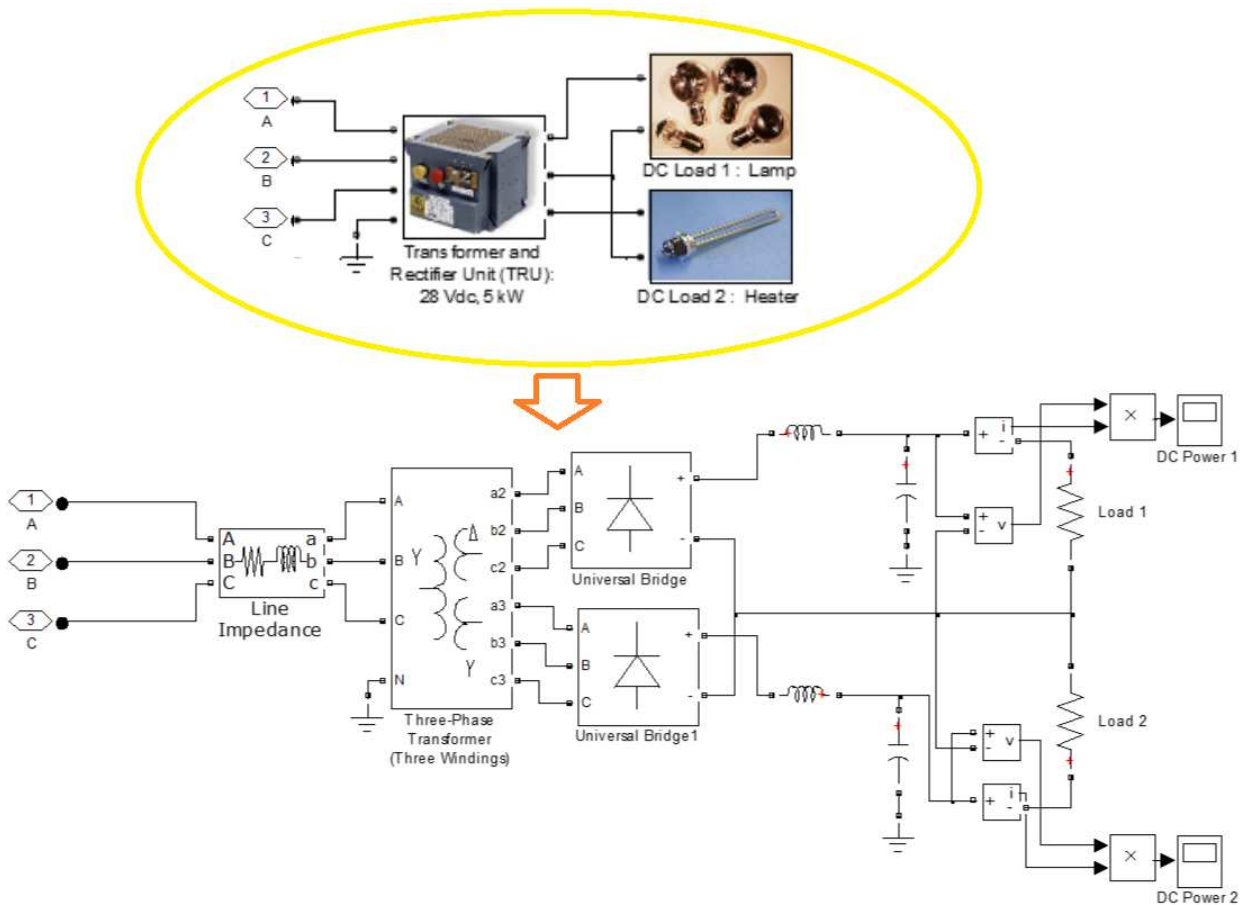
Figure 3-4: Load Setup

Recent studies point to the use of a 12 pulse transformer and rectifier unit in MEA [49], in this topology the 5th and 7th harmonics are canceled. Figure 3-5 shows the load current spectrum at 400 Hz and 800 Hz.
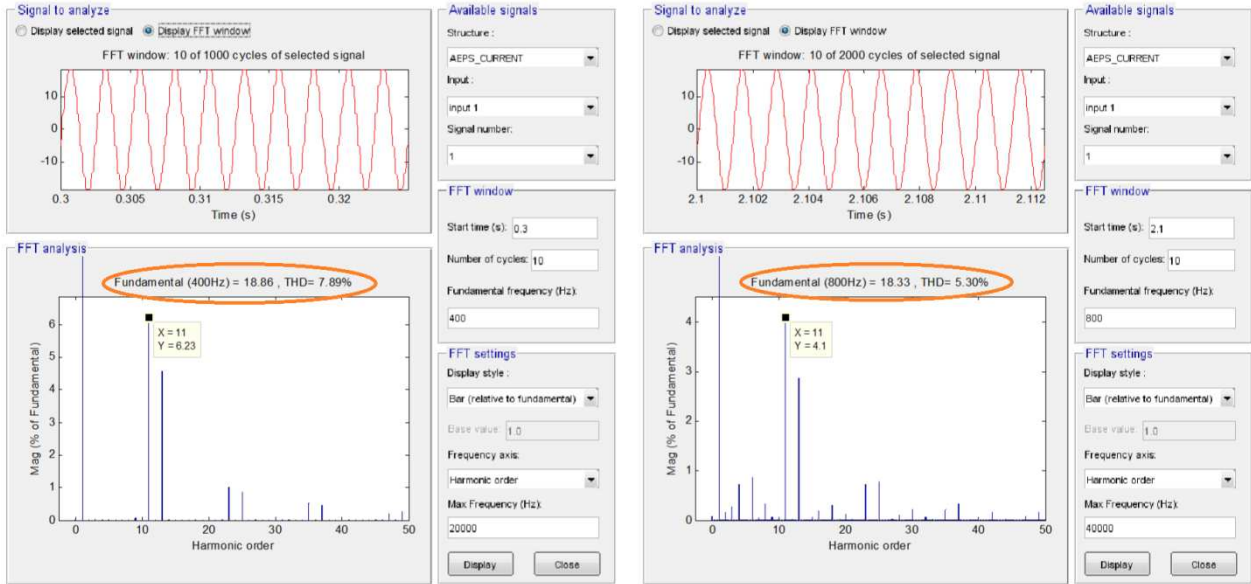
Figure 3-5: Load Spectrum

3.1.5 Performance of the KF-PLL

Figure 3-6 shows the experimental tracking response of the PIL KF-PLL. As scoped in Figure 3-1, the generated sine and the grid voltages in pu are shown. Figure 3-6(a) shows the moment when the 11th order harmonic is inserted and Figure 3-6(b) when the unbalance is applied. Figure 3-6(c) shows the response in the beginning of the $500 Hz/s$ frequency transient and Figure 3-6(d) shows the moment of the voltage drop. Figure 3-8 shows the frequency tracking error of the MIL, SIL and PIL simulations.
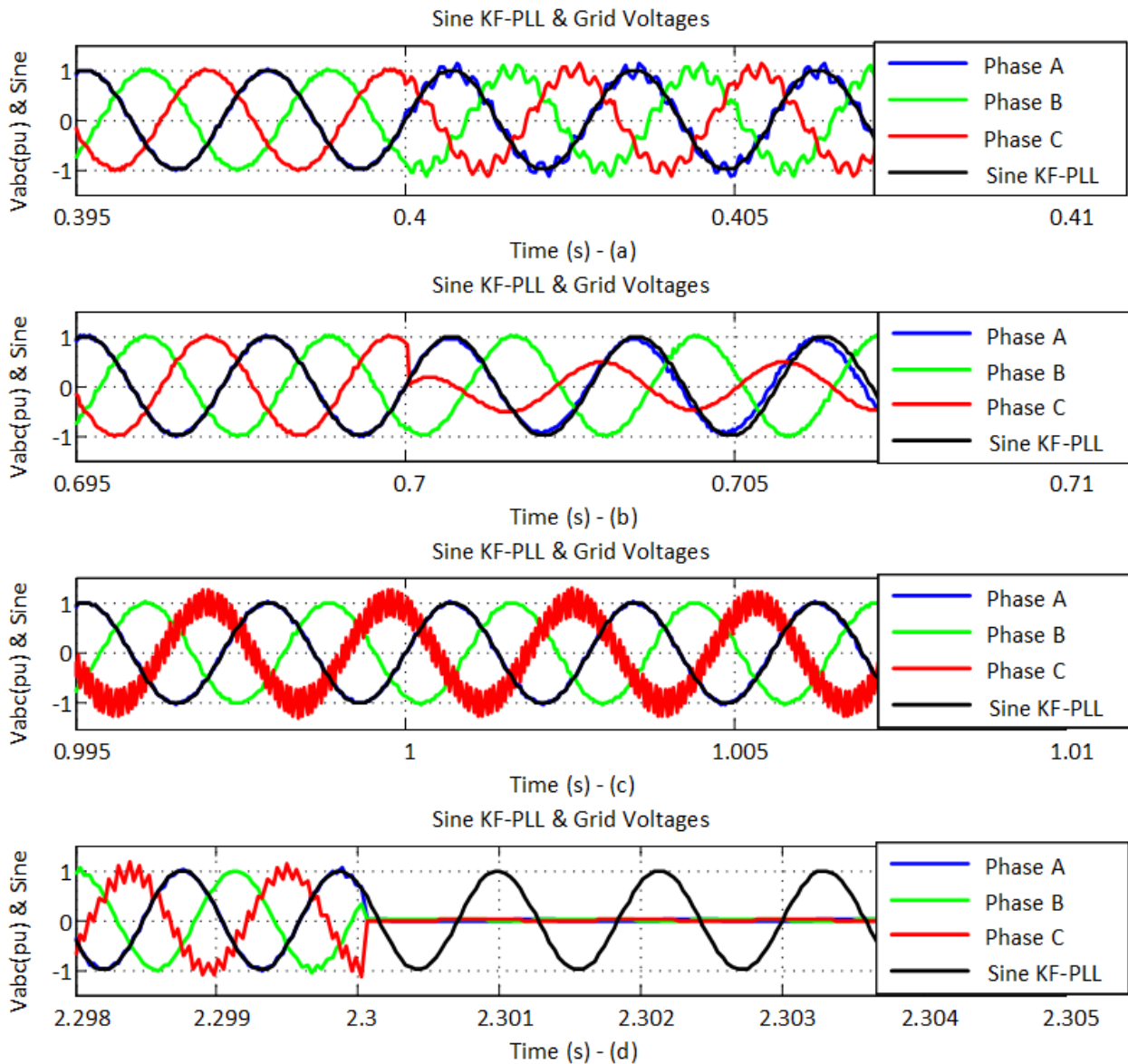
Figure 3-6: Tracking Response of the KF-PLL

Figure 3-7 shows the frequency track response of the KF-PLL. Inspecting Figure 3-7 and Figure 3-8, the KF-PLL phase tracking is very faithful, rejecting all the disturbances in an accurate manner and providing an overall good dynamic response for all frequencies. Furthermore, the frequency track is very accurate, presenting slight oscillations when the disturbances are inserted.
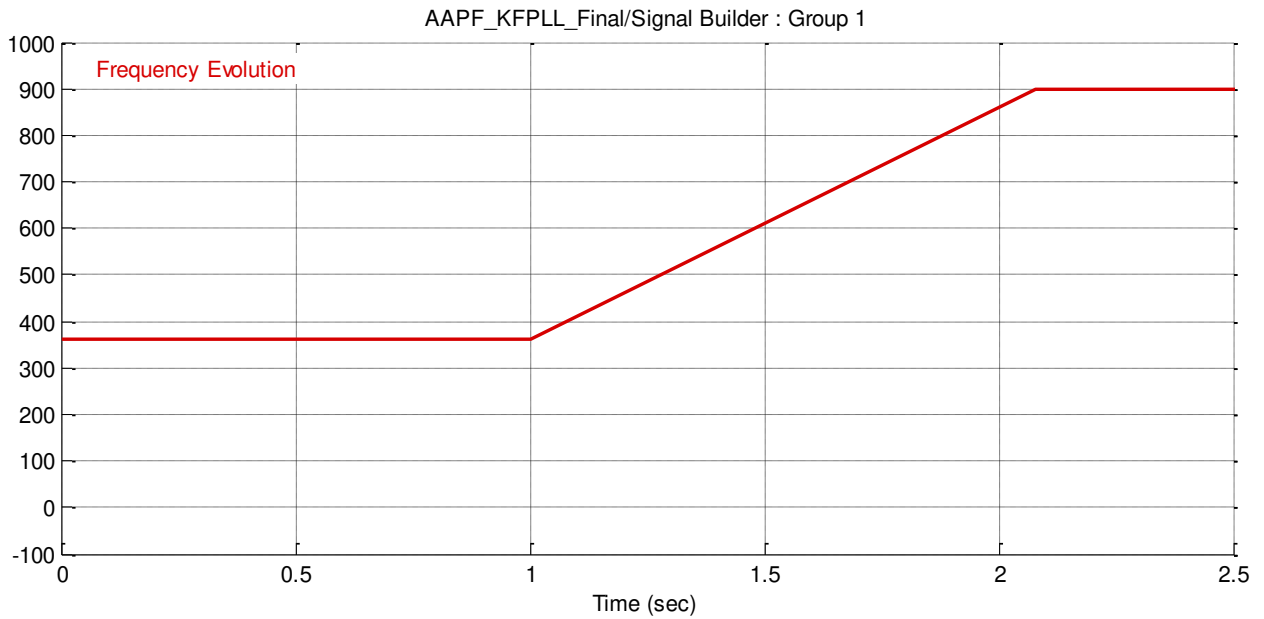
Figure 3-7: Frequency track
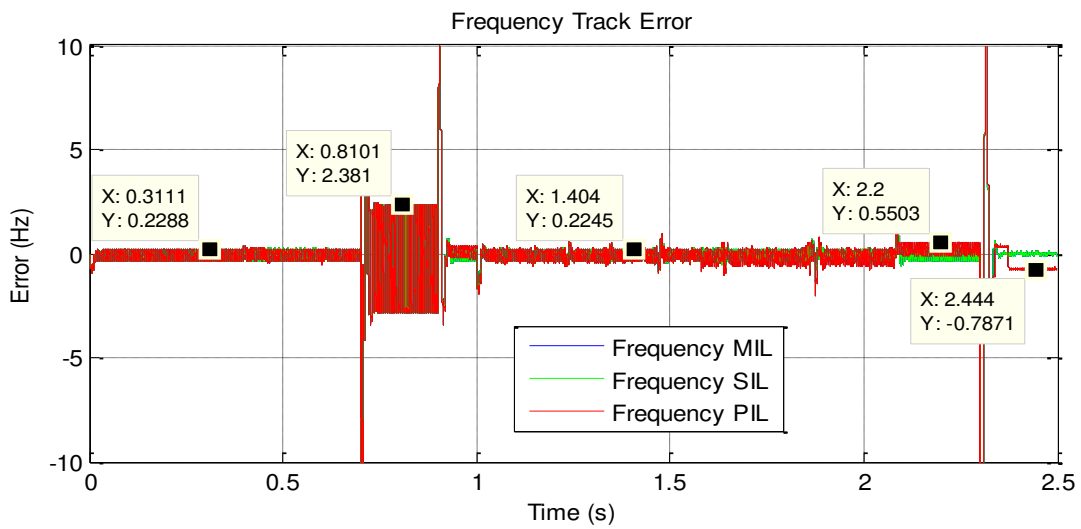
Figure 3-8: Frequency Track error of the KF-PLL

Based on the MIL and SIL responses, a small error appears in the PIL simulation (0.595% to 0.057%) considering the fundamental frequency.

3.1.6 Discussions

Thus, this KF-PLL is a proper synchronization algorithm to be used in power electronics applications for the aeronautical industry. After analyzing accurate simulation results and hardware implementation, it can be concluded that the proposed KF-PLL has proved to be very effective for voltage phase tracking of aircraft power grids, achieving good dynamics with a reasonable sampling rate.

3.2 CONSERVATIVE POWER CONTROL TECHNIQUE

Many compensation strategies have been used lately [50], some of these techniques are widely used such as the theories based on the pq-Theory [51]. The cited theories have the drawback of working only under sinusoidal conditions. The CPT [7] is valid under sinusoidal and non-sinusoidal and variable frequency conditions, additionally it can be used to selective compensation strategies [52].

The control must provide the correct references in non-sinusoidal voltage conditions; otherwise the AAPF may work improperly, which may be risky to the AEPS.

3.2.1 The Conservative Power Theory in Current Decomposition

The CPT was proposed by Tenti et al. for use in any system operation conditions. The theory can be applied to multiphase systems

In order to present the decomposition process, some definitions are necessary, such as the vector representation and the index "μ" for each m-phase variable. Considering periodical quantities, with period T and fundamental angular frequency $\omega = 2 \cdot \pi/T$, well-known definitions, such as the internal product of voltage $\underline{v}$ and current $\underline{i}$ vectors, are used to define quantities in a μ - phase electrical system.

Considering the variable $v(t)$, the mean value of $v(t)$ is (3-5).

$$\overline{v}(t) = \frac{1}{T} \int_0^T v(t) \cdot dt \tag{3-5}$$

The time integral of $v(t)$ is shown in (3-6)

$$v_f(t) = \int_0^T v(T) \cdot dt \tag{3-6}$$

Therefore, the unbiased integral of the $v_f(t)$ is shown in (3-7).

$$\hat{v}(t) = v_f(t) - \overline{v}(t) \tag{3-7}$$

Due to the Tellegen's Theorem, the instantaneous quantities and their average values are conservative for whichever network and irrespective of voltage and current waveforms [53].

3.2.2 Power Definitions of the CPT

Instantaneous Active Power (p) and Total Active Power (P), (3-8).

$$p(t) = \underline{v} \cdot \underline{i} = \sum_{\mu=1}^{M} v_\mu \cdot i_\mu \ ; \ P = \overline{p} = \langle \underline{v}, \underline{i} \rangle = \frac{1}{T} \int_0^T \underline{v} \cdot \underline{i} \, dt = \sum_{\mu=1}^{M} P_\mu \tag{3-8}$$

where v_μ and i_μ represent the voltage and the current respectively.

Instantaneous Reactive Energy (w) and Total Reactive Energy (W), *(3-9)*.

$$w(t) = \underline{\hat{v}} \cdot \underline{i} = \sum_{\mu=1}^{M} \hat{v}_\mu \cdot i_\mu \ ; \ W = \langle \underline{\hat{v}}, \underline{i} \rangle = \frac{1}{T} \int_0^T \hat{v}(t) \cdot \underline{i}(t) dt = \sum_{\mu=1}^{M} W_\mu \tag{3-9}$$

where $\underline{\hat{v}}$ is the unbiased integral of the voltage vector v.

The active power P represents the average value of instantaneous power and the reactive energy is the average value of the instantaneous energy. Based on the definitions, the current components are defined.

- Active and Reactive Currents ($i_{a\mu}$; $i_{r\mu}$), (3-10).

$$\underline{i_a} = \{i_{a\mu}\}_{\mu=a}^{m} \ \rightarrow \ i_{a\mu} = \frac{P_\mu}{V_\mu^2} \cdot v_\mu ; \quad \underline{i_r} = \{i_{r\mu}\}_{\mu=a}^{m} \ \rightarrow \ i_{r\mu} = \frac{W_\mu}{\hat{V}_\mu^2} \cdot \hat{v}_\mu \tag{3-10}$$

- Balanced and Unbalanced Active Currents ($\underline{i_a^b}, \underline{i_a^u}$), (3-11).

$$\underline{i_a^b} = \frac{P}{V^2} \cdot \underline{v} ; \ \underline{i_a^u} = \underline{i_a} - \underline{i_a^b} \tag{3-11}$$

where, the three phase voltage is represented by (3-12).

$$V = \|\underline{v}\| = \sqrt{V_a{}^2 + \cdots + V_\mu} = \sqrt{\frac{1}{T}\int_0^T \sum_{\mu=1}^m v_\mu^2 \, dt.} \tag{3-12}$$

- Balanced and Unbalanced Reactive Currents ($\underline{i}_r^b, \underline{i}_r^u$), (3-13).

$$\underline{i}_r^b = \frac{W}{\widehat{V}^2} \cdot \widehat{\underline{v}} \; ; \; \underline{i}_r^u = \underline{i}_r - \underline{i}_r^b \tag{3-13}$$

- Void Currents ($\underline{i}_v$), (3-14).

$$\underline{i}_v = \underline{i} - \underline{i}_a - \underline{i}_r \tag{3-14}$$

The current components are orthogonal to each other, (3-15):

$$I = \sqrt{I_a^2 + I_r^2 + I_v{}^2} \tag{3-15}$$

Thus, the apparent power is decomposed as follows in (3-16):

$$A = VI = \sqrt{P^2 + Q^2 + N^2 + D^2} \tag{3-16}$$

Where Q is the reactive power, N is the unbalance power and D is the distortion power.

3.2.3 Compensation Strategies

The CPT allows the detection of distinct components in the currents (Active, Reactive, Unbalance and Void). Therefore, the technique allows selective compensation of particular disturbing elements as shown in Table 3-3.

Table 3-3: Compensation Strategies using CPT

Balanced reactive current compensation	$\underline{i}_r{}^b{}_{comp} = -\underline{i}_r^b$
Unbalanced current compensation	$\underline{i}^u{}_{comp} = -\left(\underline{i}_a^u + \underline{i}_r^u\right)$
Void current compensation	$\underline{i}_{v\,comp} = -\underline{i}_v$
Non active (total) compensation	$i_{na\,comp} = -(\underline{i} - \underline{i}_a^b)$

Using an AAPF, any compensation can be applied in the control strategy. In this manner, the disturbing effects can be selected to be compensated, as shown in Figure 3-9.
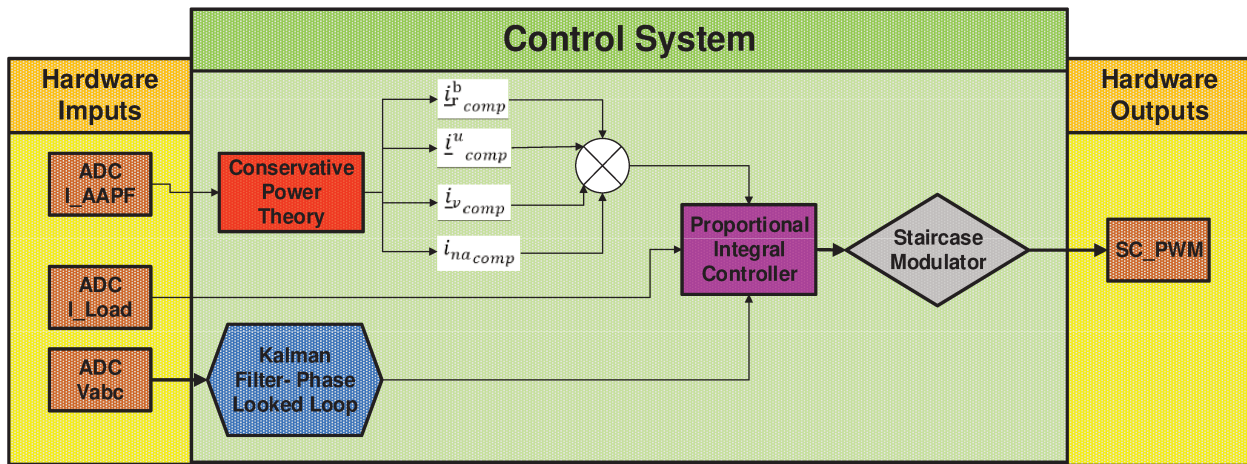
Figure 3-9: Selective Compensation Scheme

For enabling the total harmonic filtering, the load currents that must be eliminated by the AAPF are $\underline{i}_r^b, \underline{i}^u$ and $\underline{i}_v$, in other words, we will use the Non active (total) compensation ($i_{na_{comp}}$). Using this setup, the AAPF will cancel all the harmonics and reactive power demanded by the loads.

Thus, in order to validate the CPT application for AEPS, the next section shows the simulation of the CPT to AEPS.

3.2.4 Simulations of the CPT

The simulation of the CPT technique was developed in Matlab/Simulink, as represented in Figure 3-10.
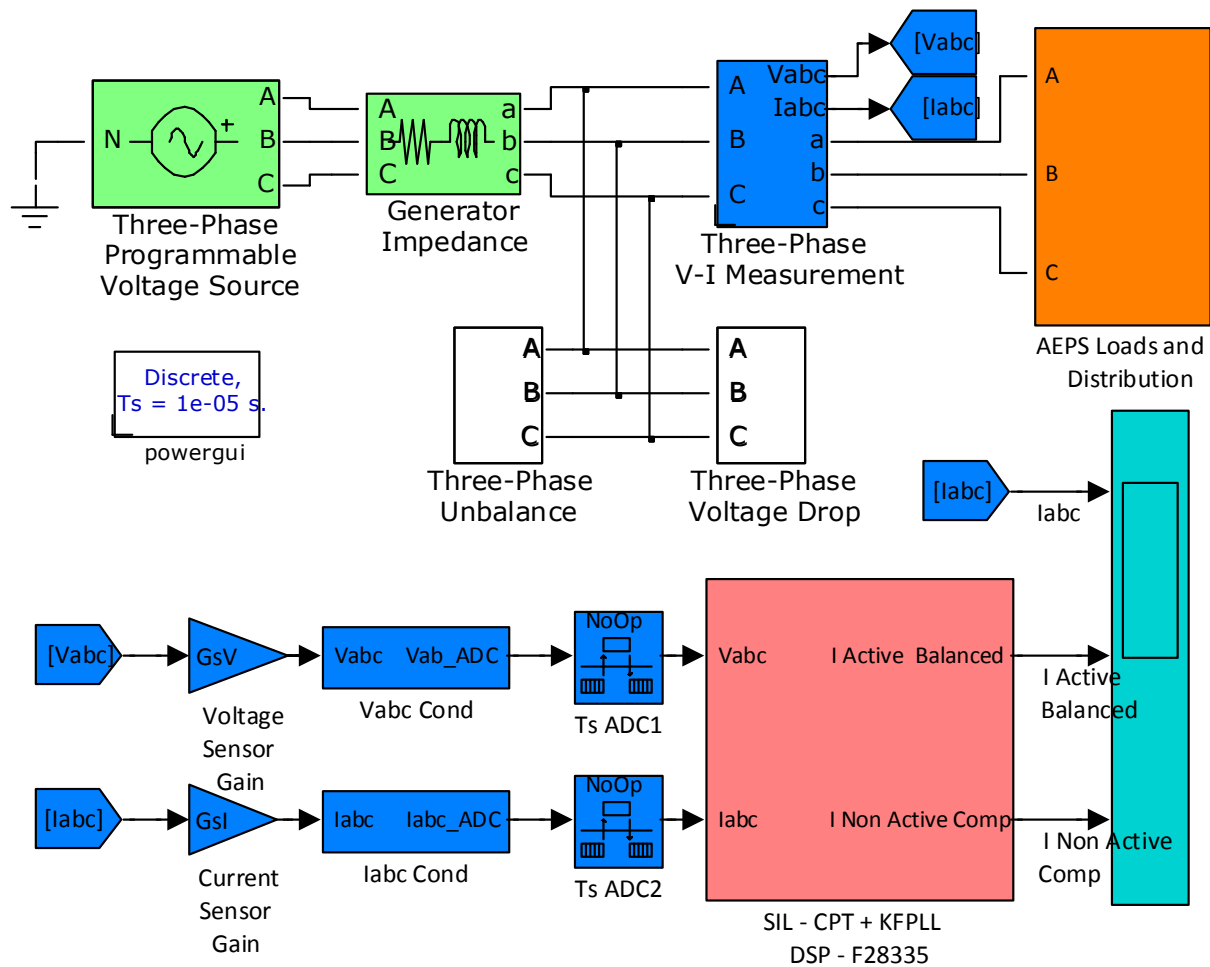
Figure 3-10: CPT + KF-PLL System overview

The simulation by SIL, hereafter the simulation using the generated code of the model, validates the code implemented to a real time microprocessor, Figure 3-11 shows the SIL – CPT + KF-PLL. This time, the PIL simulation will not be performed, it will be left to the end, when the control algorithm is complete.

Figure 3-11: CPT+KF-PLL

The block CPT performs the Non active (total) compensation as discussed in section 3.2.3. The implementation of this technique is shown in Figure 3-12.

Figure 3-12: Non active (total) compensation

The active power and three-phase voltage is calculated by the "Discrete 3-phase PLL-Driven Active Power" block. This block deploys equations (3-8), which calculates P and (3-12), which calculates V. These calculations are shown in Figure 2-13.
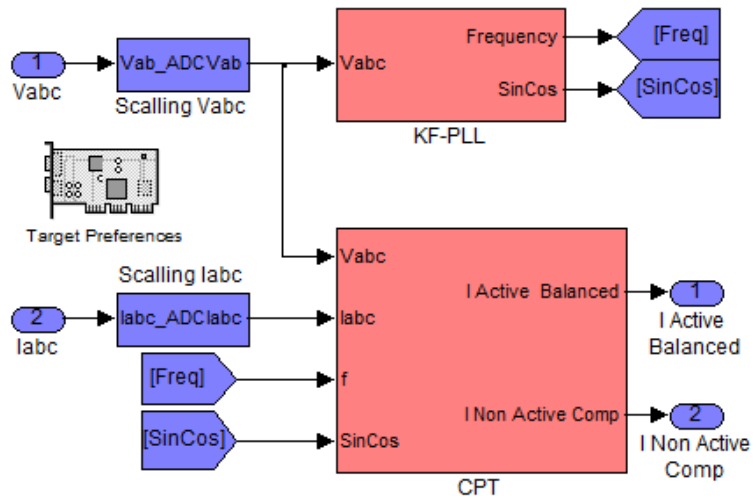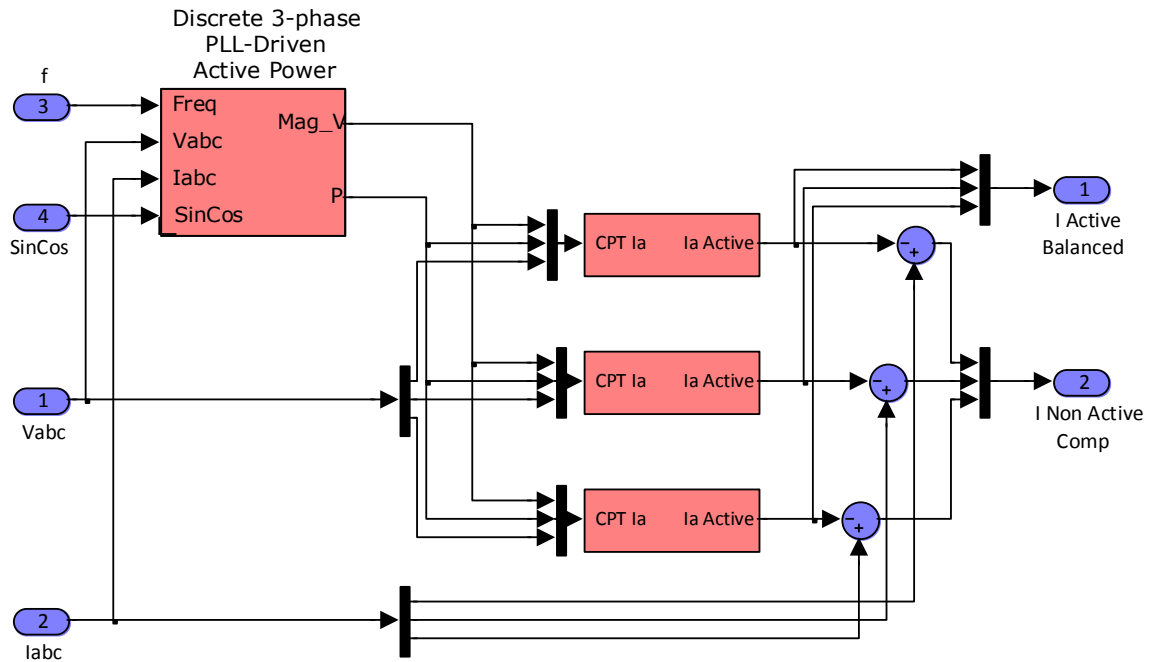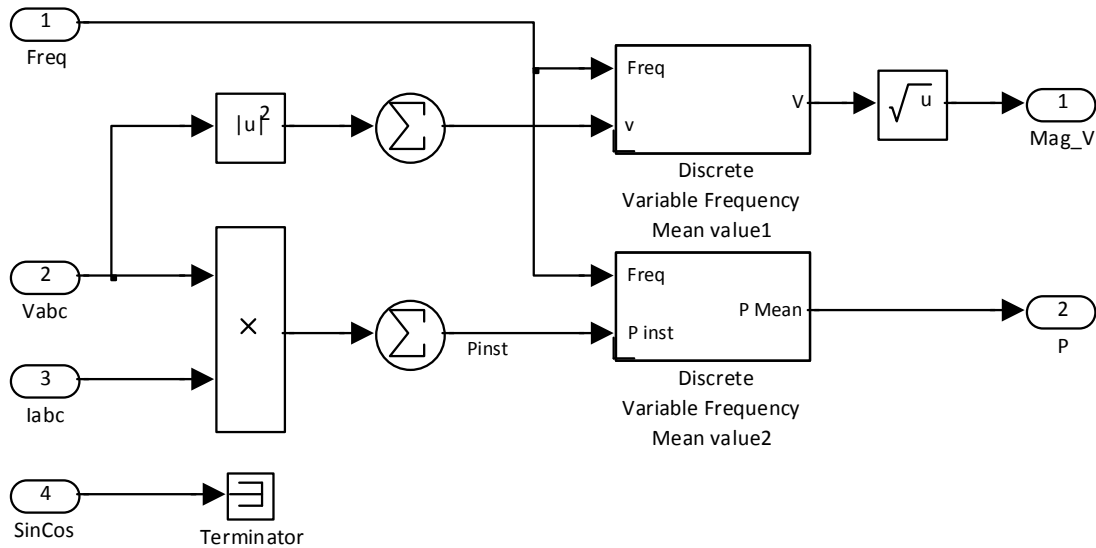

Figure 3-13 - Three-phase voltage and Active Power calculations

In order to demonstrate the algorithm dynamic response in the presence of perturbations that can occur in the AEPS, the same sequence of events of section 3.1.4 is applied. These events prove the CPT with the KF-PLL robustness to harmonics, unbalance, frequency variations, and voltage sags. Table 3-2 contains the parameters of the simulated AEPS.

Figure 3-14 shows the CPT response of the SIL – CPT + KF-PLL when the 11th order harmonic is inserted. The load currents, shown at Figure 3-14(b), do not change when the distortion is added. This happens because the load impedance mitigates this behavior, causing the load current to preserve its waveform. Note that the current of Figure 3-14(c) follows the form of the voltage. Additionally, the currents of Figure 3-14(d) represents the compensation currents, which should be added to the systems by an AAPF to extinguish the reactive and void currents.

Figure 3-14: Figure 3-14(a) scopes the voltage; Figure 3-14(b) represents the load current. Figure 3-14(c) shows the active balanced currents of the load due to CPT decomposition. Figure 3-14(d) represents the compensation currents

Figure 3-15 shows the moment when the unbalance is applied. At this point the load current becomes very high due to the voltage unbalance; the unbalance causes the appearance of zero sequence currents, as noted in the load currents. Note that the current of Figure 3-15(c) is not balanced due to the voltage unbalance. Furthermore, the currents of Figure 3-15 (d) represents the compensation currents which should be added to the systems by an AAPF to extinguish the reactive currents, the void currents and the unbalanced currents.
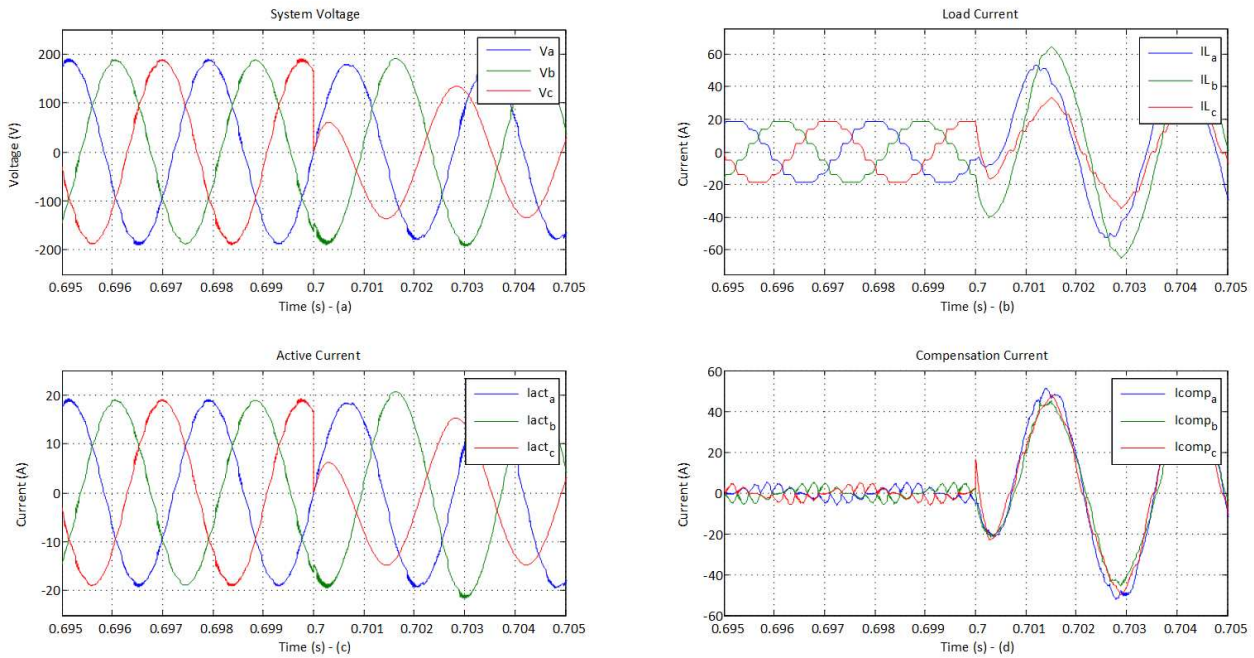
Figure 3-15: Figure 3-15 (a) scopes the voltage; Figure 3-15 (b) represents the load current. Figure 3-15(c) shows the active balanced currents of the load due to CPT decomposition. Figure 3-15 (d) represents the compensation currents

Figure 3-16 shows the response at the beginning of the $500 Hz/s$ frequency transient. The currents of Figure 3-16 (c) follows the form of the voltage. In addition, Figure 3-16 (d) represents the compensation currents which should be added to the systems by an AAPF to extinguish the reactive currents and the void currents.
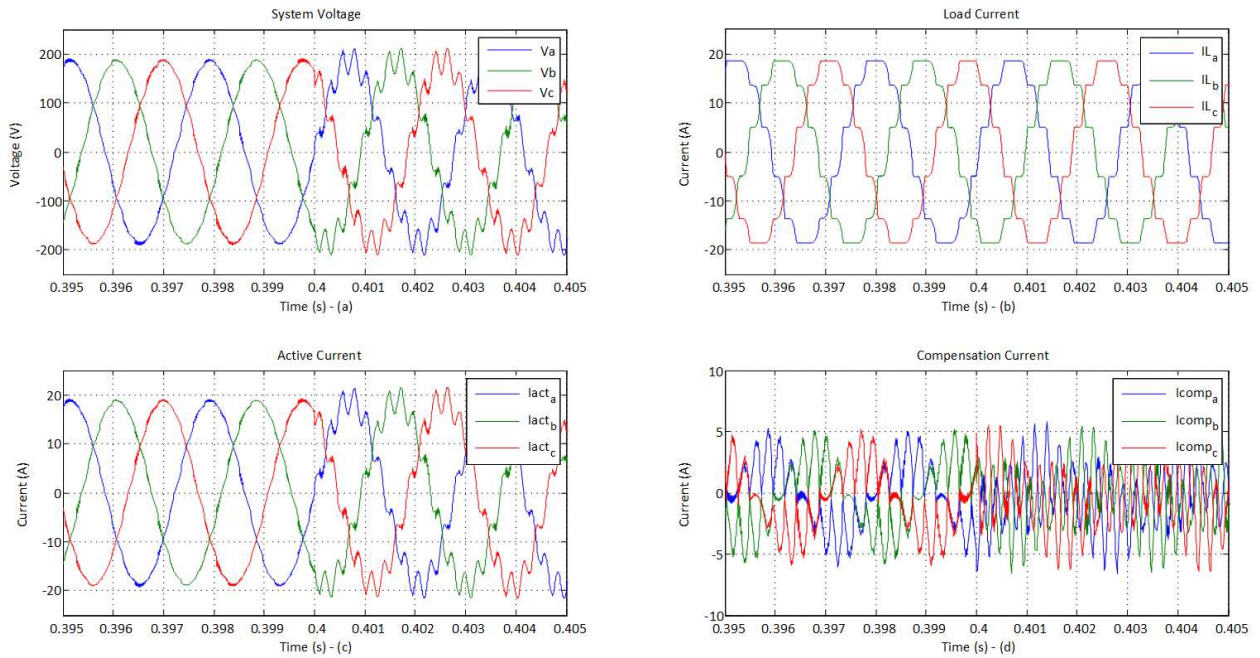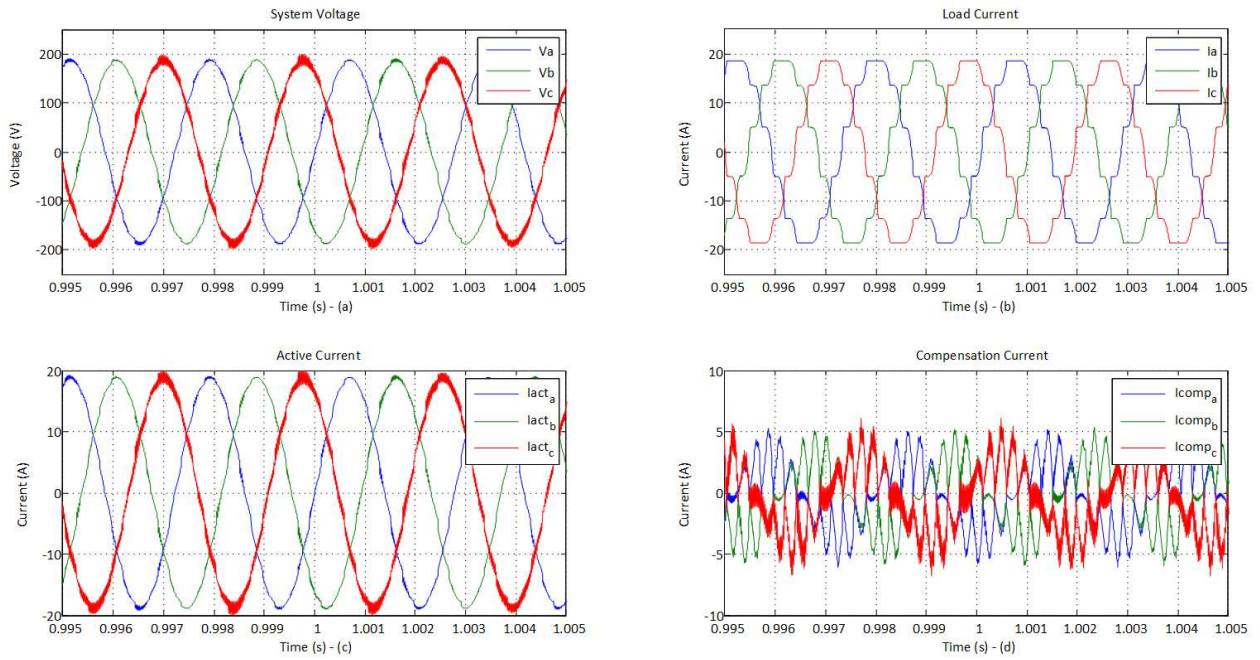
Figure 3-16: Figure 3-16 (a) scopes the voltage; Figure 3-16 (b) represents the load current. Figure 3-16 (c) shows the active balanced currents of the load due to CPT decomposition. Figure 3-16 (d) represents the compensation currents

Figure 3-17 shows the moment of the voltage drop. Still, the current of Figure 3-17 (c) follows the form of the voltage. Figure 3-17 (d) represents the Compensation Currents which are extinguished with the load current.
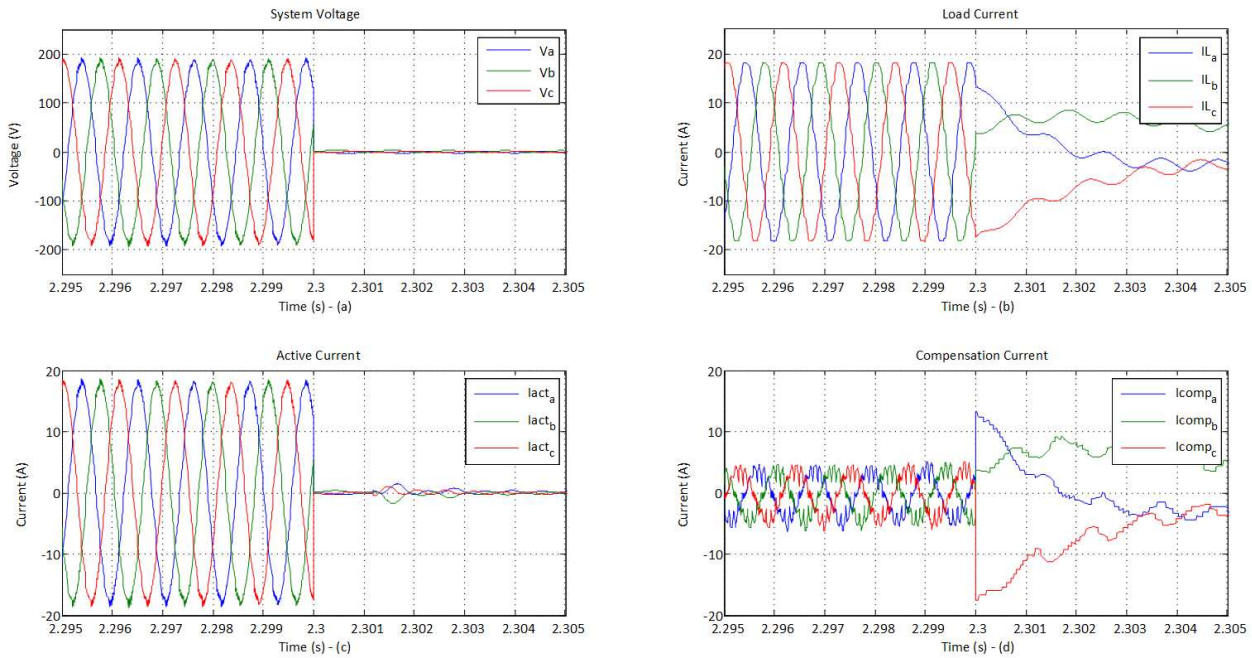
Figure 3-17: Figure 3-17 (a) scopes the voltage, Figure 3-17 (b) represents the load current which decreases within the time. Figure 3-17 (c) shows the active balanced currents of the load according to CPT decomposition. Figure 3-17 (d) represents the Compensation Currents

The above sequence of events proves the CPT reliability to be used when the source presents harmonics, under unbalanced conditions, under frequency transients and faults.

3.2.5 Conclusions

There are four possible compensation strategies based on the CPT current decomposition. As shown before, this feature is possible because of the orthogonally of the decomposed current components.

This section has shown the application of the non-active (total) compensation, to be used as control reference for an AAPF. In an AEPS, it is important that the generator works property, providing low reactive power and avoiding harmonics which can lead to electrical losses and mechanical vibrations and instabilities.

3.3 ASSYMETRICAL MULTILEVEL INVERTER

The Asymmetrical Multilevel Inverter (AMI) minimizes the output voltage high frequency components in the AC side due to the increased number of levels, the generated voltage has lower harmonics compared to the voltage generated by a PWM inverter, and consequently the inductance of the output filters can be reduced. There are drawback associated with these converters, such as several numbers of inverters and algorithm complexity.

3.3.1 AMI Topology

An AMI with three single-phase inverters, series connected, per phase was considered for this work as shown in Figure 3-18. It is mainly used to synthesize the desired voltage wave shape from several DC voltages sources.

Equation (3-17) calculates the number of levels that an AMI can produce if the voltage level of the lowest voltage partial cell is equals to Ucc and if the voltage of the other cells are multiple of this voltage, $m \cdot Ucc$.

The Staircase Modulation (SCM) [54] enables the generation of up to 27 voltage levels in the converter output when using the relation 3:1 for the voltage sources in each cell. Moreover, in this configuration, the switching frequency, and consequently the losses, is reduced in the higher voltage cells.

$$n = 1 + 2 \cdot \sum_{k=1}^{m} \frac{Ea_k}{Ucc} \qquad (3\text{-}17)$$
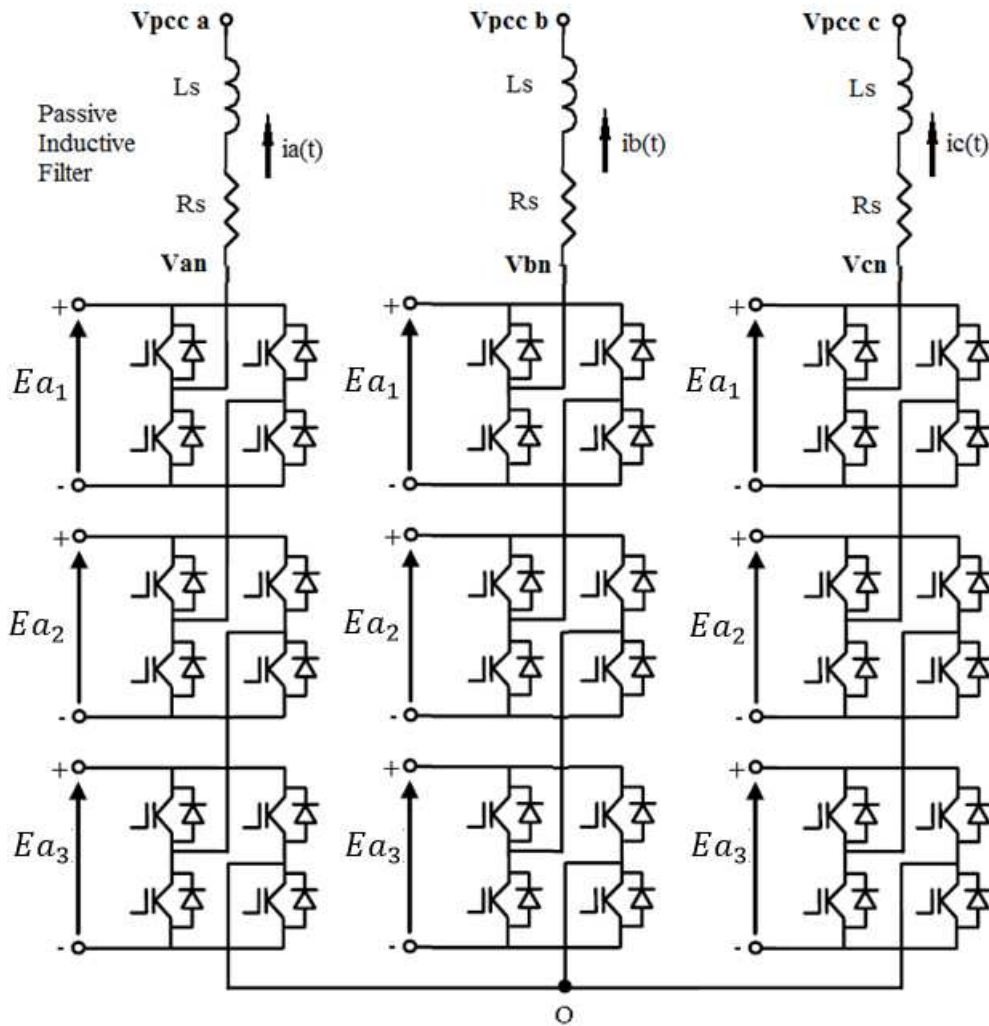
Figure 3-18: Multilevel Converter Topology

In order to extract the best characteristics of this converter the relation 3:1 was used .This ratio refers to the level of the voltages in each cell of the inverter and is represented by (3-18).

$$Ea_k = 3^{(k-1)} \cdot Ucc \tag{3-18}$$

Resulting in:

$$(Ea_1; Ea_2; Ea_3) = (Ucc; 3 \cdot Ucc; 9 \cdot Ucc)$$

Solving (3-17), $n = 27$ is obtained. The 27 voltage levels can only be achieved when the proper modulation algorithm is applied to the system. A staircase modulator was developed to the simulator to provide the switching signals that must be applied to each partial cell. The modulation technique is presented in Figure 3-19.

Figure 3-19: Staircase Modulation

Using the AMI of Figure 3-18 with the modulation of Figure 3-19 it is possible to have a voltage controlled AAPF able to follow the voltage references with the minimum output distortion, as well as increased performance comparing to three-phase inverters.
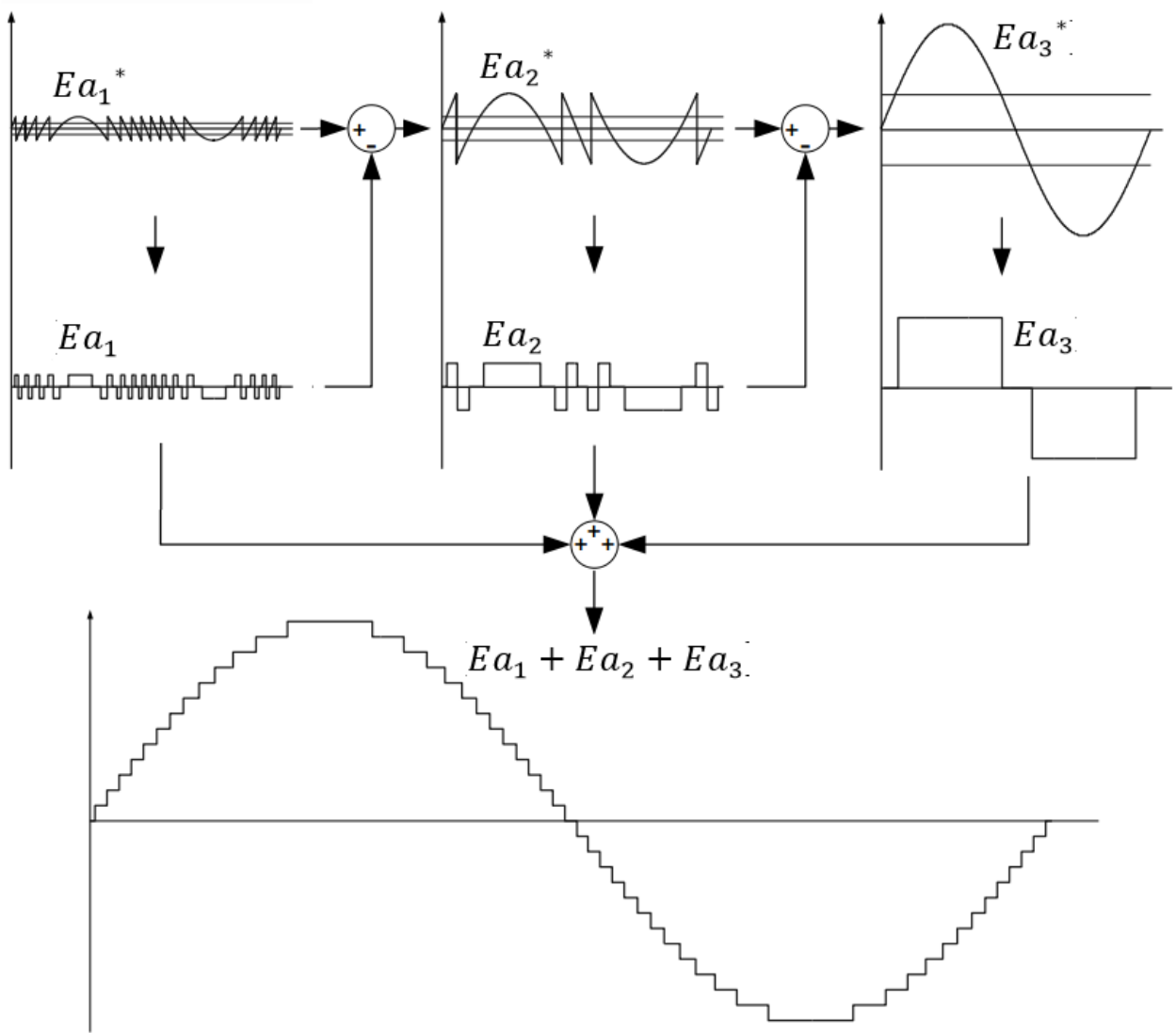
3.3.2 Model of the AMI

In an AEPS the voltage changes frequently, while the controller must be always synchronized. Performing the modelling of the AMI [55], [56] , the small-signal transfer function is obtained, which is valid for each phase.

3.3.2.1 Small-signal modelling

The objective is to determine the small-signal transfer function that relates the converter current to the duty-cycle of the switches.

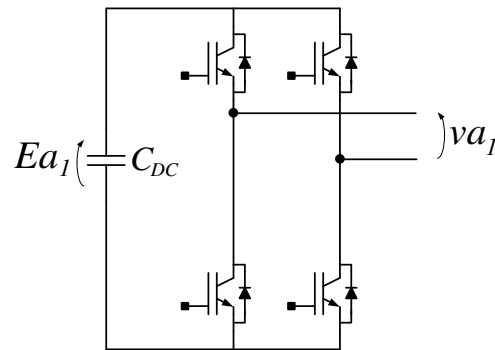Figure 3-20 shows one single-phase cell from the nine normally used in a three phase AMI.

Figure 3-20: Single-phase cell of an AMI

Applying a duty cycle $D(t)$ to the cell of Figure 3-20, $va_1(t)$ is obtained, (3-19).

$$va_1(t) = Ea_1[2D(t) - 1] \tag{3-19}$$

Based on (3-19), each arm of the AMI can be represented as Figure 3-21.
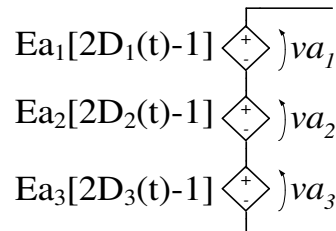

Figure 3-21: Single-phase Model of the AMI

Rearranging Figure 3-21, and connecting the single-phase AMI to the PCC, Figure 3-22 is obtained.

$[Ea_1+Ea_2+Ea_3][2D_t(t)-1]$
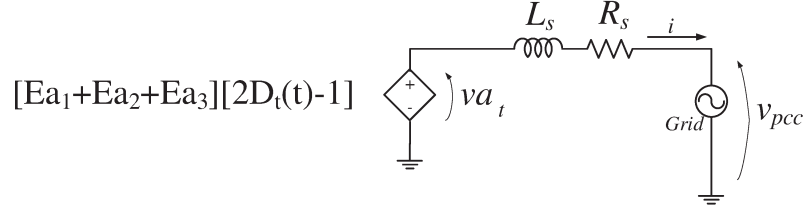
Figure 3-22: Single-phase AMI connected to PCC

For modelling the AMI, the following assumptions are considered:

1. The total duty cycle is defined as in (3-20), [55]:

$$D_t(t) = D_1(t) + D_2(t) + D_3(t) \qquad (3\text{-}20)$$

Applying Kirchhoff's law to the system of Figure 3-22, it is deducted the three-phase differential equation of the AMI, (3-21).

$$[Ea_1 + Ea_2 + Ea_3] \cdot \left[2\overrightarrow{D(t)} - 1\right] = L_s \cdot \frac{d\overrightarrow{i(t)}}{dt} + R_s \cdot \overrightarrow{i(t)} + \overrightarrow{V_{pcc}} \qquad (3\text{-}21)$$

Where,

$$\overrightarrow{D_t(t)} = \begin{bmatrix} D_1(t) \\ D_2(t) \\ D_3(t) \end{bmatrix}$$

$$\overrightarrow{i(t)} = \begin{bmatrix} i_a(t) \\ i_b(t) \\ i_c(t) \end{bmatrix}$$

$$\overrightarrow{v_{pcc}(t)} = \begin{bmatrix} v_{pcc\_a}(t) \\ v_{pcc\_b}(t) \\ v_{pcc\_c}(t) \end{bmatrix}$$

Equation (3-21) is referenced in the Park's reference frame (pq) by means of (3-22).

$$\overrightarrow{Y_{abc}(t)} = \overrightarrow{Y_{dq}(t)} \cdot e^{j \cdot E(t)} \qquad (3\text{-}22)$$

Where,

$$\overrightarrow{Y_{dq}(t)} = Y_d + j \cdot Y_q;$$

69

$$\frac{dE(t)}{dt} = \omega_{dq}$$

Solving the derivatives terms of (3-22), (3-23) is obtained.

$$[Ea_1 + Ea_2 + Ea_3] \cdot \left[2\overrightarrow{D_{t_{dq}}}(t) \cdot e^{j \cdot E(t)} - 1 \right]$$

$$= L_s \cdot \left\{ \frac{\overrightarrow{di_{dq}}(t)}{dt} \cdot e^{j \cdot E(t)} + j \cdot \omega \cdot \overrightarrow{i_{dq}}(t) \cdot e^{j \cdot E(t)} \right\} + \qquad (3\text{-}23)$$

$$R_s \cdot \overrightarrow{i_{dq}}(t) \cdot e^{j \cdot E(t)} + \overrightarrow{V_{pcc\_dq}} \cdot e^{j \cdot E(t)}$$

Equation (3-23) is non-linear due to the inverter's behavior. To linearize, a perturbation must be added to the equation. In this manner (3-23) is separated in the average value and a small signal variation, as shown in (3-24), (3-25) and (3-26).

$$\overrightarrow{D_{t\_dq}}(t) = \overline{\overrightarrow{D_{t\_dq}}} + \widetilde{\overrightarrow{d_{t\_dq}}}(t) \qquad (3\text{-}24)$$

$$\overrightarrow{i_{dq}}(t) = \overline{\overrightarrow{I_{dq}}} + \widetilde{\overrightarrow{i_{dq}}}(t) \qquad (3\text{-}25)$$

$$\overrightarrow{V_{pcc_{dq}}}(t) = \overline{\overrightarrow{V_{pcc_{dq}}}} \qquad (3\text{-}26)$$

Note that (3-26) does not have a small signal perturbation. We obtain (3-27) after replacing (3-24), (3-25) and (3-26) in (3-23).

$$[Ea_1 + Ea_2 + Ea_3] \cdot \left[2 \cdot \left(\overline{\overrightarrow{D_{t\_dq}}} + \widetilde{\overrightarrow{d_{t\_dq}}}(t) \right) \cdot e^{j \cdot E(t)} - 1 \right]$$

$$= L_s \cdot \left[\frac{\widetilde{\overrightarrow{di_{dq}}}(t)}{dt} \cdot e^{j \cdot E(t)} + j \cdot \omega \cdot \left(\overline{\overrightarrow{I_{dq}}} + \widetilde{\overrightarrow{i_{dq}}}(t) \right) \cdot e^{j \cdot E(t)} \right] + \qquad (3\text{-}27)$$

$$R_s \cdot \left(\overline{\overrightarrow{I_{dq}}} + \widetilde{\overrightarrow{i_{dq}}}(t) \right) \cdot e^{j \cdot E(t)} + \overline{\overrightarrow{V_{pcc_{dq}}}} \cdot e^{j \cdot E(t)}$$

Isolating the average terms and the small signal terms, (3-28) is obtained. This is the small signal differential equation of the system in the Park's reference frame.

$$[Ea_1 + Ea_2 + Ea_3] \cdot \left[2 \cdot \widetilde{\overrightarrow{d_{t_{dq}}}}(t) \cdot e^{j \cdot E(t)} \right]$$

$$= L_s \cdot \left[\frac{\widetilde{\overrightarrow{di_{dq}}}(t)}{dt} \cdot e^{j \cdot E(t)} + j \cdot \omega \cdot \widetilde{\overrightarrow{i_{dq}}}(t) \cdot e^{j \cdot E(t)} \right] + \qquad (3\text{-}28)$$

$$R_s \cdot \widetilde{\overrightarrow{i_{dq}}}(t) \cdot e^{j \cdot E(t)}$$

Simplifying (3-28), (3-29) is obtained.

$$[Ea_1 + Ea_2 + Ea_3] \cdot \left[2 \cdot \overrightarrow{\widetilde{d_{t_{dq}}}}(t)\right]$$

$$= L_s \cdot \left[\frac{d\widetilde{\overrightarrow{i_{dq}}}(t)}{dt} + j \cdot \omega \cdot \overrightarrow{\widetilde{i_{dq}}}(t)\right] + R_s \cdot \overrightarrow{\widetilde{i_{dq}}}(t) \qquad (3\text{-}29)$$

Expanding (3-29), (3-30) is obtained.

$$[Ea_1 + Ea_2 + Ea_3] \cdot \left[2 \cdot \widetilde{d_{t_d}}(t) + j \cdot 2 \cdot \widetilde{d_{t_q}}(t)\right]$$

$$= L_s \cdot \left[\frac{d\left(\widetilde{i_d}(t) + j \cdot \widetilde{i_q}(t)\right)}{dt} + j \cdot \omega \cdot \left(\widetilde{i_d}(t) + j \cdot \widetilde{i_q}(t)\right)\right] + \qquad (3\text{-}30)$$

$$R_s \cdot \left(\widetilde{i_d}(t) + j \cdot \widetilde{i_q}(t)\right)$$

Isolating the real and imaginary parts, it is deducted the equations for the d (3-31) and q (3-32) axis.

$$[Ea_1 + Ea_2 + Ea_3] \cdot \left[2 \cdot \widetilde{d_{t_d}}(t)\right] = L_s \cdot \left[\frac{d\widetilde{i_d}(t)}{dt} - j \cdot \omega \cdot \widetilde{i_q}(t)\right] + R_s \cdot \widetilde{i_d}(t) \qquad (3\text{-}31)$$

$$[Ea_1 + Ea_2 + Ea_3] \cdot \left[2 \cdot \widetilde{d_{tq}}(t)\right] = L_s \cdot \left[\frac{d\widetilde{i_q}(t)}{dt} + j \cdot \omega \cdot \widetilde{i_d}(t)\right] + R_s \cdot \widetilde{i_q}(t) \qquad (3\text{-}32)$$

Equation (3-31) and (3-32), are coupled. Authors [57], [58] assume that these terms are very weakly coupled and can be eliminated. This leads to (3-33) and (3-34).

$$[Ea_1 + Ea_2 + Ea_3] \cdot \left[2 \cdot \widetilde{d_{t_d}}(t)\right] = L_s \cdot \left[\frac{d\widetilde{i_d}(t)}{dt}\right] + R_s \cdot \widetilde{i_d}(t) \qquad (3\text{-}33)$$

$$[Ea_1 + Ea_2 + Ea_3] \cdot \left[2 \cdot \widetilde{d_{tq}}(t)\right] = L_s \cdot \left[\frac{d\widetilde{i_q}(t)}{dt}\right] + R_s \cdot \widetilde{i_q}(t) \qquad (3\text{-}34)$$

Applying Laplace transformation, the transfer function of the system is obtained (3-35), which is valid for both d and q axis. Therefore, the AMI small-signal transfer function is obtained, which is valid for all phases.

$$\frac{\widetilde{i_d}(s)}{d_{t\_d}(s)} = G_i(s) = \frac{2 \cdot G_m \cdot [Ea_1 + Ea_2 + Ea_3]}{S \cdot L_s + R_s} \qquad (3\text{-}35)$$

Where $d_{t\_d}(s)$ symbolizes slights variations in the value of the duty cycle $D_t(t)$ and G_m the sensor gain.

3.3.2.2 Design of the PI Controller

It is important to find a relation between the voltage levels of the cells and the inductance of the passive filter. Low voltage levels may limit the capability to filter high harmonic orders; the same applies to high inductance of the passive filter, which is also responsible to the current ripple. The AAPF shall be able to compensate harmonics when the AEPS is at $800 Hz$; therefore the di/dt in the inductor must be fast enough.

3.3.2.2.1 Voltage Levels of the Partial Cells

Accordingly to Table 3-2 the system voltage is $230\ Vrms$ (phase to phase), therefore the peak voltage (phase to ground) is equals to (3-36).

$$Vpeak = \sqrt{2} \cdot \frac{230}{\sqrt{3}} = 187.8\ V \qquad (3\text{-}36)$$

For the purposes of the AAPF, its maximum voltage will be chosen 50% higher than the system voltage. The system frequency is very high, therefore, in order to guarantee that the current variations is enough fast, the filter peak voltage will be $(187.8 + \frac{187.8}{2} = 281.7\ V)$. The voltage levels of the partial cells are defined as in (3-38).

$$Ucc + 3 \cdot Ucc + 9 \cdot Ucc = 281.7\ V \qquad (3\text{-}37)$$

Thus,

$$Ucc = \frac{281.7}{13} = 21.66\ V \qquad (3\text{-}38)$$

3.3.2.2.2 Passive Filter Inductance

In order to set the AAPF inductance, the load current worst case scenario (highest harmonic distortion) must be taken. As seen in Figure 3-5, the THD at $800 Hz$ is 5.3%, this happens because Load 1 and Load 2 are balanced therefore the 5th and 7th harmonics are cancelled. The worst case

scenario happens when Load 2 or Load 1 is disconnected; Figure 2-23 shows the current spectrum of this case.
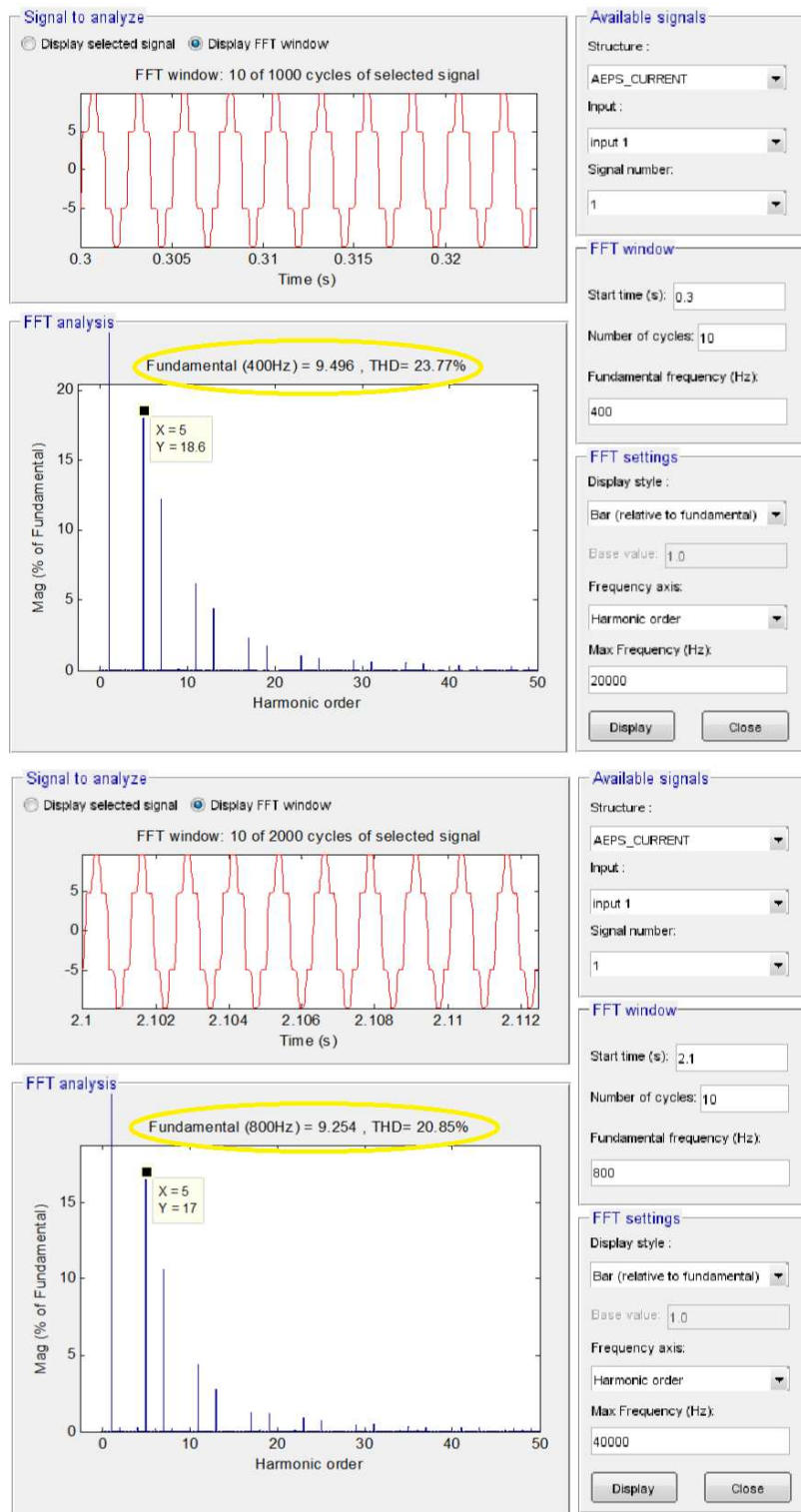

Figure 3-23: Load Spectrum

73

The most representative harmonic is the 5th (17% of fundamental at $800Hz$). The 5th harmonic amplitude is $I_5 = 1.57\ A$, the active filter must be able to cancel part of this current though the inductance. Considering the harmonic currents limitations of Table 2-3, I_5 must be mitigated as in (3-39).

$$I_{5\ max} = 0.02 \cdot I_1 \qquad (3\text{-}39)$$

As shown in Figure 3-23 the fundamental component of the load current at $800Hz$ is $I_1 = 9.254\ A$. Therefore, the maximum value of the 5th harmonic is $I_{5\ max} = 0.185A$. Thus, the active filter must synthetize a current of $I_{AAPF} = I_5 - I_{5\ max} = 1.388A$.

Due to the staircase modulation, the low and middle voltage cell will switch to compensate the 5th harmonic. Hence, the maximum reactance of the inductive filter can be estimated by (3-41).

$$X_L = \frac{Ucc + Ucc \cdot 3}{I_{AAPF}} = \frac{21.66 \cdot 4}{1.388} = 62.416\ \Omega \qquad (3\text{-}40)$$

Where,

$$X_L = \omega \cdot L = 2 \cdot \pi \cdot f_5 \cdot L \qquad (3\text{-}41)$$

When the system is at $800Hz$ the 5th harmonic is at $4000Hz$, therefore the maximum value of the inductance is calculated by (3-42).

$$L = \frac{X_L}{2 \cdot \pi \cdot f_5} = \frac{62.416}{2 \cdot \pi \cdot 4000} = 2.483 \cdot 10^{-3}H \qquad (3\text{-}42)$$

The loads of an AEPS are constantly changing, thus, in order to avoid the operation of the AAPF close to the maximum limits, the parameters were chosen as shown in Table 3-4.

Table 3-4: Parameters of the AMI

Parameters of the AMI	Value
Ls	$1.2\ mH$
Rs	$0.1\ \Omega$
$(Ea_1; Ea_2; Ea_3)$	$(22.2; 66.6; 200)\ V$
$Sensor\ Gain\ (G_m)$	$1/200$

Including the parameters of Table 3-4 in the transfer function (3-35), (3-43) is obtained.

$$G_i(s) = \frac{2.889}{S \cdot 1.2 \cdot 10^{-3} + 0,1} \tag{3-43}$$

The frequency response technique was used to tune the PI controller. Equation (3-44) allows the tuning of the PI controller in a desired cut-off frequency (f_c). This frequency is chosen some decades lower than the switching frequency to damp the ripple and to avoid phase delays.

$$\begin{cases} K_p = 10^{\frac{|G_i(fc)|}{20}} \\ K_i = \dfrac{K_p}{10} \end{cases} \tag{3-44}$$

Choosing $f_c = 31.2kHz$ and inspecting the Gain and Phase margins diagrams of Figure 3-24, K_p and K_i are obtained. For the cutoff frequency chosen, the AAPF will be able to compensate up to the 39th harmonic if the system frequency is at $800Hz$. The switching frequency chosen was $100kHz$.
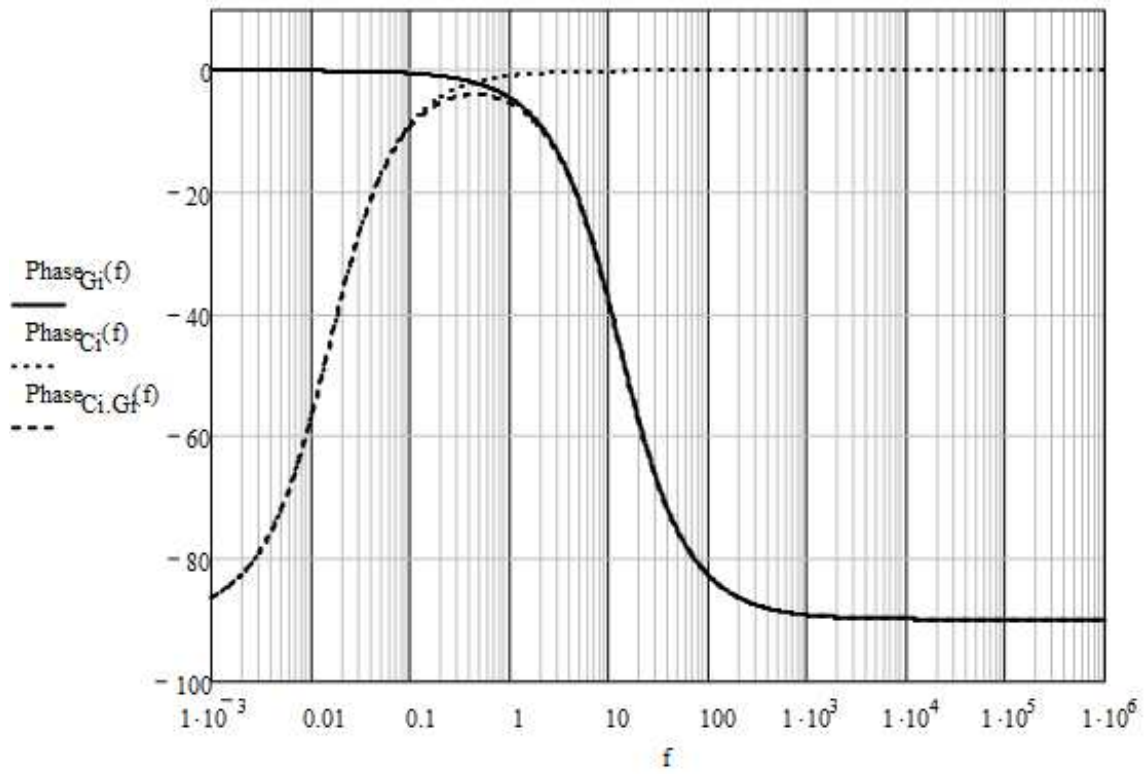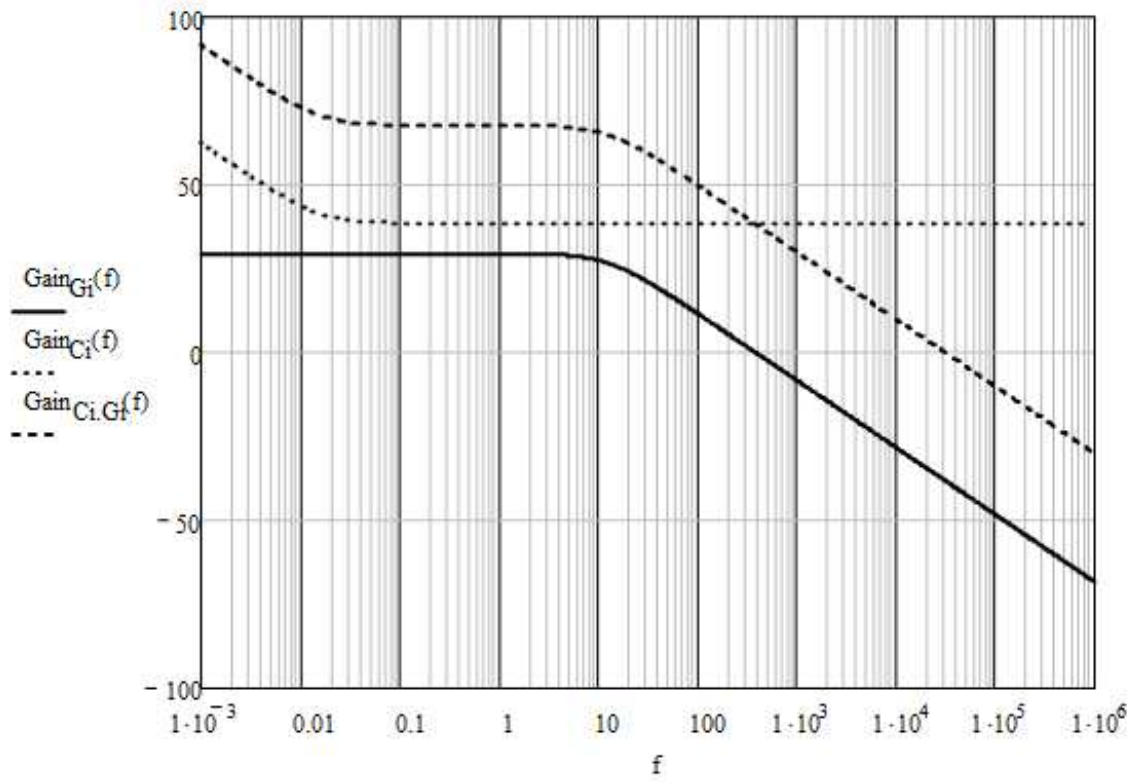
Figure 3-24: Gain and Phase Margins

76

The controller transfer function is obtained, (3-45). Analyzing the diagrams, it can be seen that the controller has the desired characteristics for the application.

$$CPI(S) = 81.438 + \frac{8.1438}{S} \qquad (3\text{-}45)$$

The PI was converted into the discrete domain using the Forward Euler method for digital implementation (3-46).

$$CPI(z) = 81.438 + \frac{8.1438 \cdot Ts}{z - 1} \qquad (3\text{-}46)$$

Where, Ts is the sampling time.

3.3.3 Simulations of the AMI

The simulation of the Stair Case Modulation (SCM) with the Asymmetrical Multileve Inverter (AMI) was developed in Matlab/Simulink, as represented in Figure 3-25.
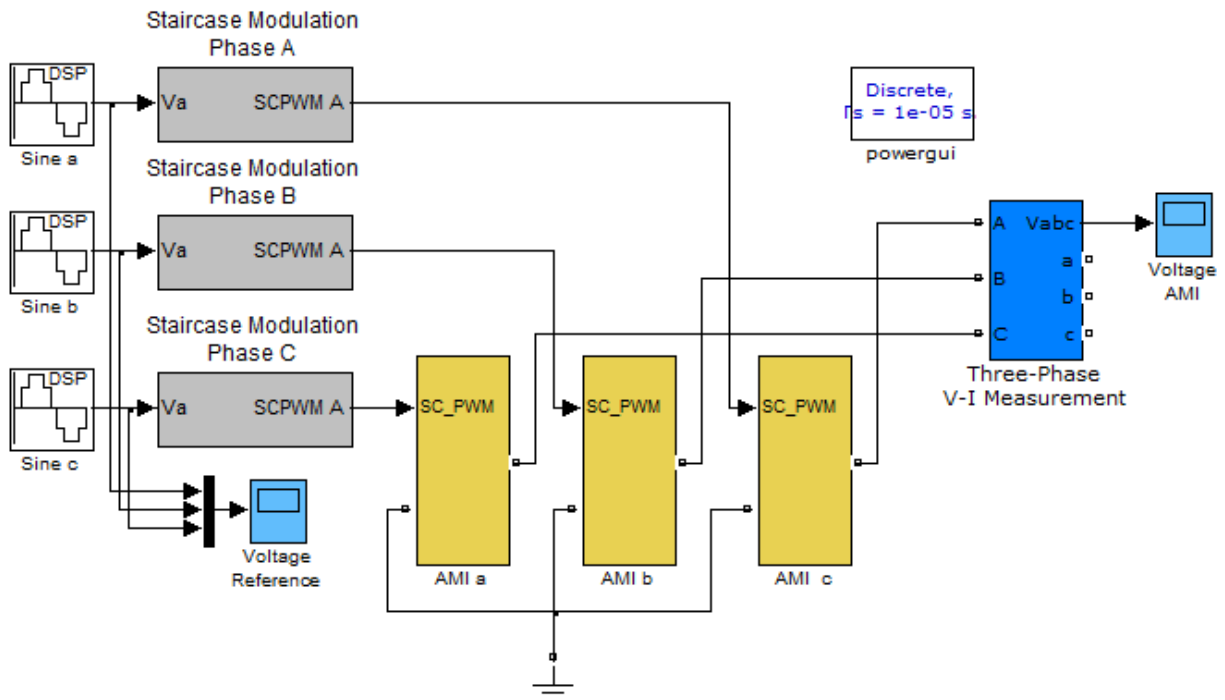

Figure 3-25: Staircase + AMI System Overview

77

The block "AMI a,b,c" implements the inverter of Figure 3-18 and the blocks "Staircase Modulation Phase a,b,c" performs the SCM, as shown in Figure 3-19. The blocks "Sine a,b,c" generate a 3 phase voltage reference, the amplitudes are equal to the sum of $(Ea_1 + Ea_2 + Ea_3 = 22.2 + 66.6 + 200 = 290.33V)$.

For demonstrating the AMI operation, the simulation is run using the parameters of Table 3-4. Figure 3-26 shows what is scoped in "Voltage Reference" and "Voltage AMI".
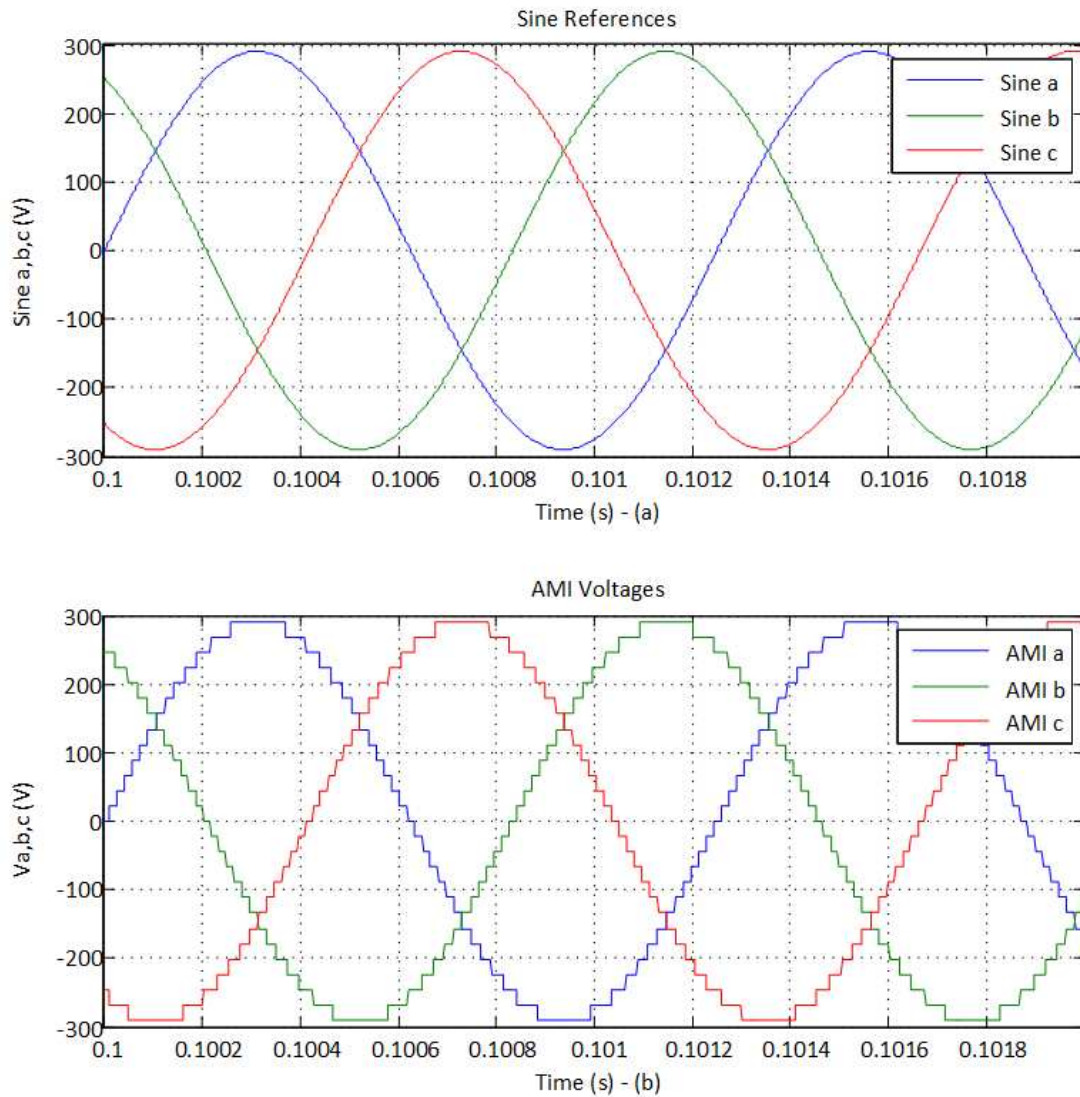

Figure 3-26: Sine References and AMI Voltages

Inspecting Figure 3-26 it can be seen that the voltage generated by the AMI is very similar to the voltage reference, this feature is only possible because the AMI is able to generate 27 levels when the SCM is used. Figure 3-27 shows the spectrum of the voltage of Figure 3-26.
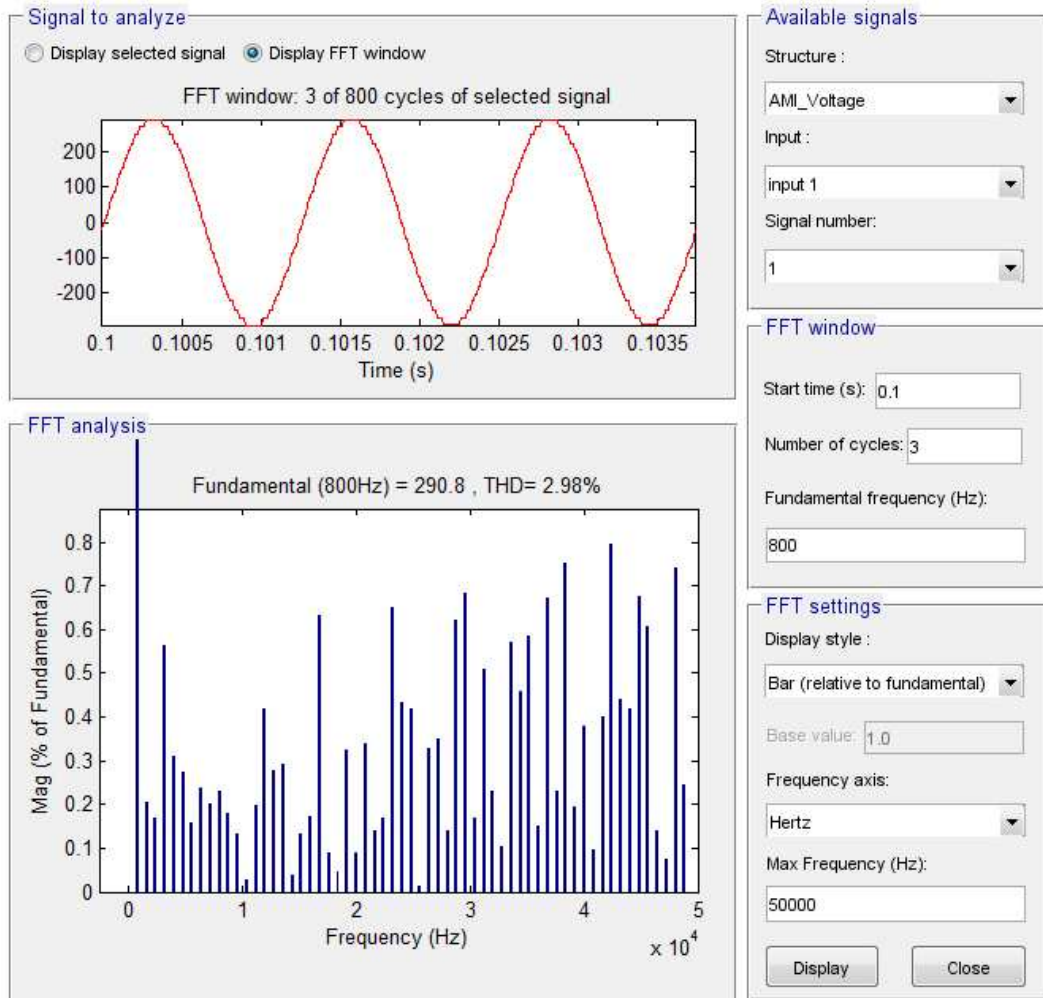
78

Figure 3-27: Spectrum of the AMI Voltage

The THD of the AMI voltage is 2.98%, which is considered low. When connected to the PCC, the AMI will generate lower voltage distortion compared to most inverters.

3.3.4 Conclusions

This section has shown the model and control of an AMI as well as the application of the Staircase Modulation. For an AAPF connected to an AEPS it is fundamental to have low output distortion and a very fast response. The SCM and AMI not only decrease the switching frequency of the inverter but also reduces the size of the output filter which connects the AAPF to the grid.

4 SIMULATIONS OF THE AERONAUTICAL ACTIVE POWER FILTER

After the development of the most important structures of the Aeronautical Active Power Filter (AAPF), a high fidelity simulator was built in Matlab/Simulink. A comprehensive model of the VSVF Aircraft Electrical Power Systems (AEPS) was modeled in order to study the performance of the filter over a frequency range of operation from $333.3 Hz$ to $800 Hz$. Fig. 6 shows the schematics representation of it.
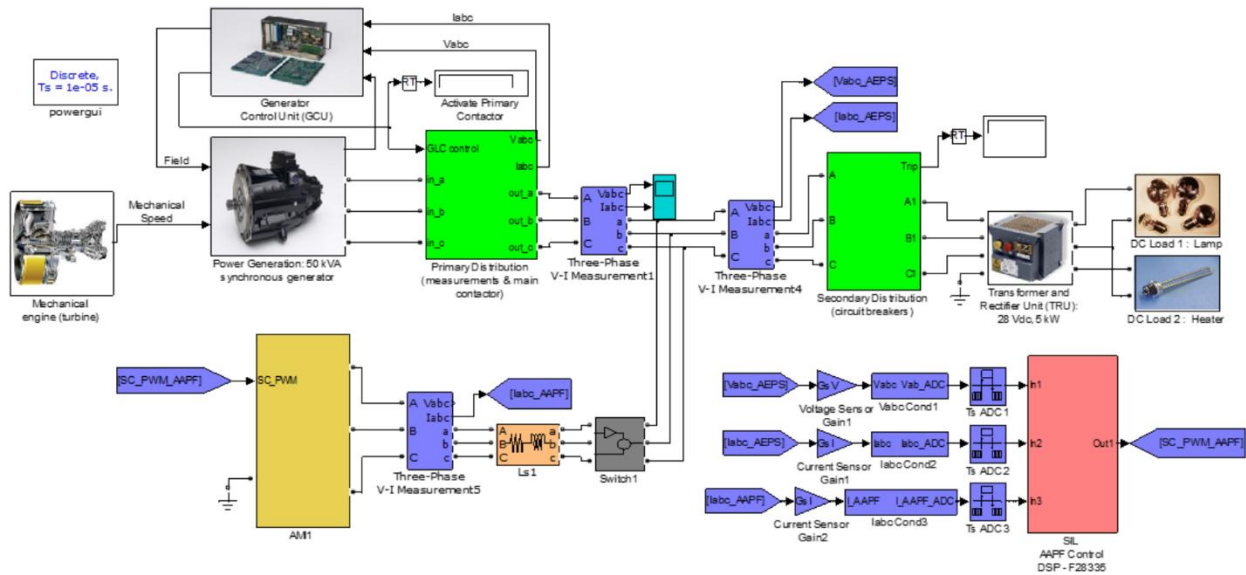

Figure 4-1: AAPF and Aircraft Power Generation and Distribution System

4.1 CIRCUIT DESCRIPTION

The circuit of Figure 4-1 illustrates a basic AEPS with generation and distribution. The AC bus is VSVF, which means that the frequency is variable and depends on the engine speed. The "Mechanical Engine" represents the generator mechanical drive and is modeled by a signal builder, which provides the mechanical speed of the engine shaft. The "Power Generator" represents the AC generator. It is modelled as a synchronous machine, and rotates in the same frequency as the engine speed. The "Generator Control Unit" regulates the voltage of the generator to 230 volts line to line.

The "Primary Distribution" contains three current and voltage sensors. A 3-phase contactor, controlled by the "Generator Control Unit", is placed to avoid under frequencies. The "Secondary Power Distribution" system is composed by circuit breakers. As nonlinear loads, there is a 5 kW Transformer and Rectifier Unit which supplies $28V$ DC to a $2.5kW$ lamp and a $2.5kW$ heater. The above load is similar to the load of Figure 3-4.

Table 4-1 contains the parameters of the simulated system.

Table 4-1: Parameters of the System

Permanent Magnet Synchronous Generator	Parameters
Nominal Power	$50kVA$
Line-to-Line Voltage	$230V$RMS
Nominal Frequency	$400Hz$
Pair of Poles	2
Internal Impedance	$R = 0.0204\ \Omega;$ $L = 0.08104mH$
Inertia	$J = 0.02Kg \cdot m^2$
Loads	
DC	$5kW$
AMI	
Ls	$1.2mH$
Rs	$0.1\ \Omega$
$(Ea_1; Ea_2; Ea_3)$	$(22.2; 66.6; 200)V$
$Sensor\ Gain\ (G_m)$	$1/200$

The other blocks of Figure 4-1 implement the AAPF. The block "AMI" implements the multilevel inverter (section 3.3.3) and the block "SIL AAPF Control" implements the control algorithm shown in Figure 4-2.
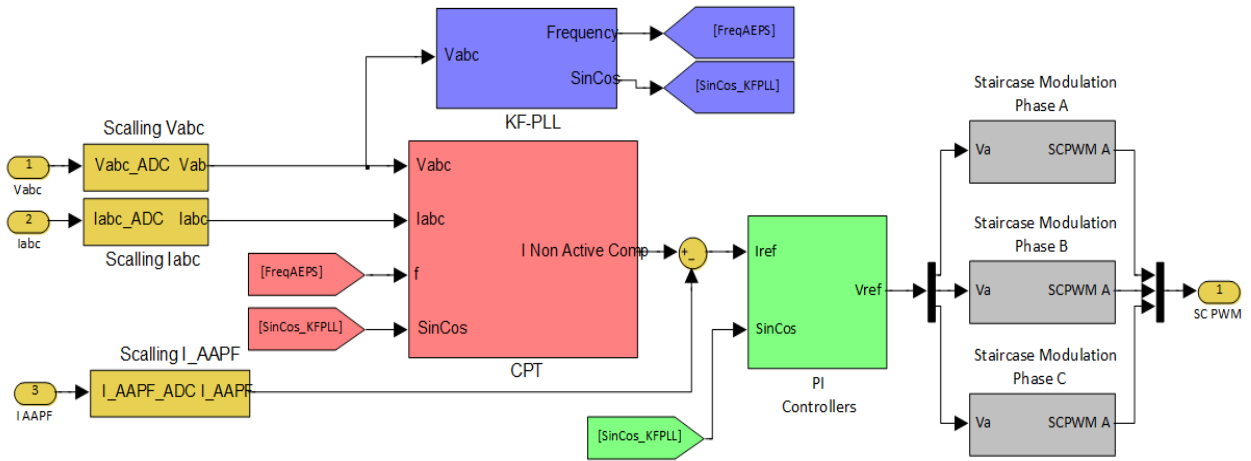
Figure 4-2: AAPF Control Algorithm

The block "PI Controllers" has 3 PIs in the Park reference frame, Figure 4-3. This was done to render the control algorithm robust to frequency variatios. Additionally, each of the controllers has an anti-windup loop to avoid saturations of the voltage reference "Vref".
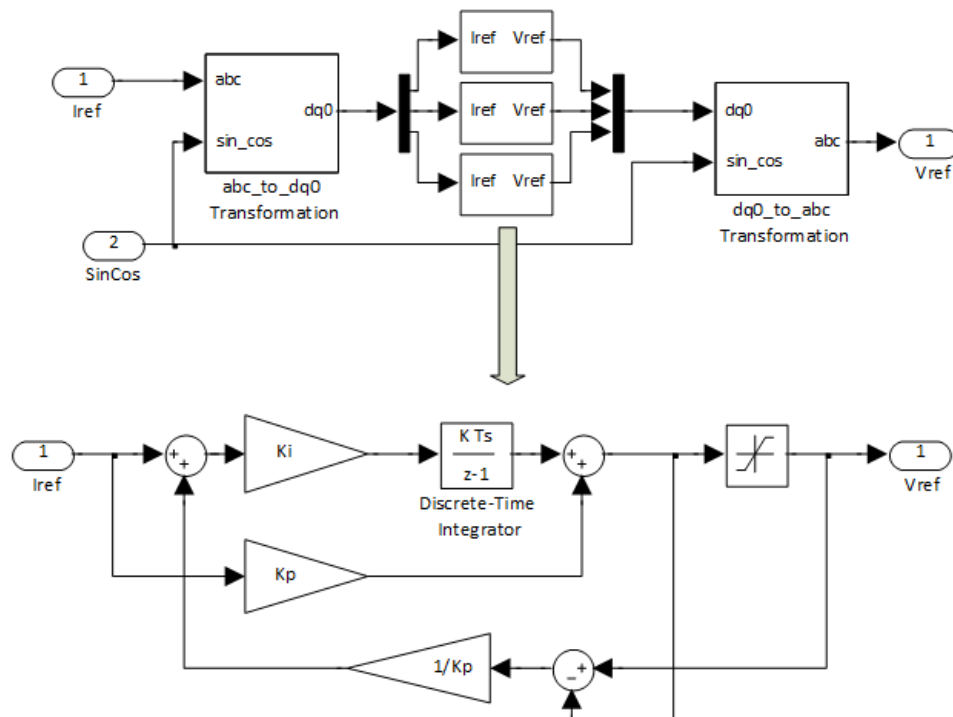

Figure 4-3: PI Controllers

4.2 SEQUENCE OF EVENTS

The AAPF and the AEPS of Figure 4-1 have been simulated during 6 seconds for representing different situations that can occur in the AEPS. The turbine speed is represented by Figure 4-4 and the sequence of events is:

1. At $t = 0s$, the engine accelerates from $0rpm$ to $12000rpm$ in 0.4 seconds. This represents a variation of $0Hz$ to $400Hz$ in the electrical system. At $t = 0.3s$, the speed reaches the threshold of $9000\ rpm$ $(300Hz)$. The Generator Control Unit activates the primary contactor, which enables the AC power on the aircraft. All the resistive loads are now online. The DC bus voltage increases to $28V$.

2. At $t = 2s$, the engine speed decelerates from $12000\ rpm$ $(400Hz)$ to $10000rpm$ $(333.3Hz)$ in 1 second. At $t = 3.1s$, the engine accelerates from $10000rpm$ $(333.3Hz)$ to $24000rpm$ $(800Hz)$ in 1.4 second.

3. At $t = 4.6s$, the engine speed decelerates from 24000 rpm (800 electrical Hz) to 0 rpm in 1.4 seconds. At $t = 5.48s$, the speed reaches the threshold of $8900\ rpm$ $(296Hz)$. So the GCU de-activates the primary contactor. The GCU regulates the AC voltage during the whole simulation period.
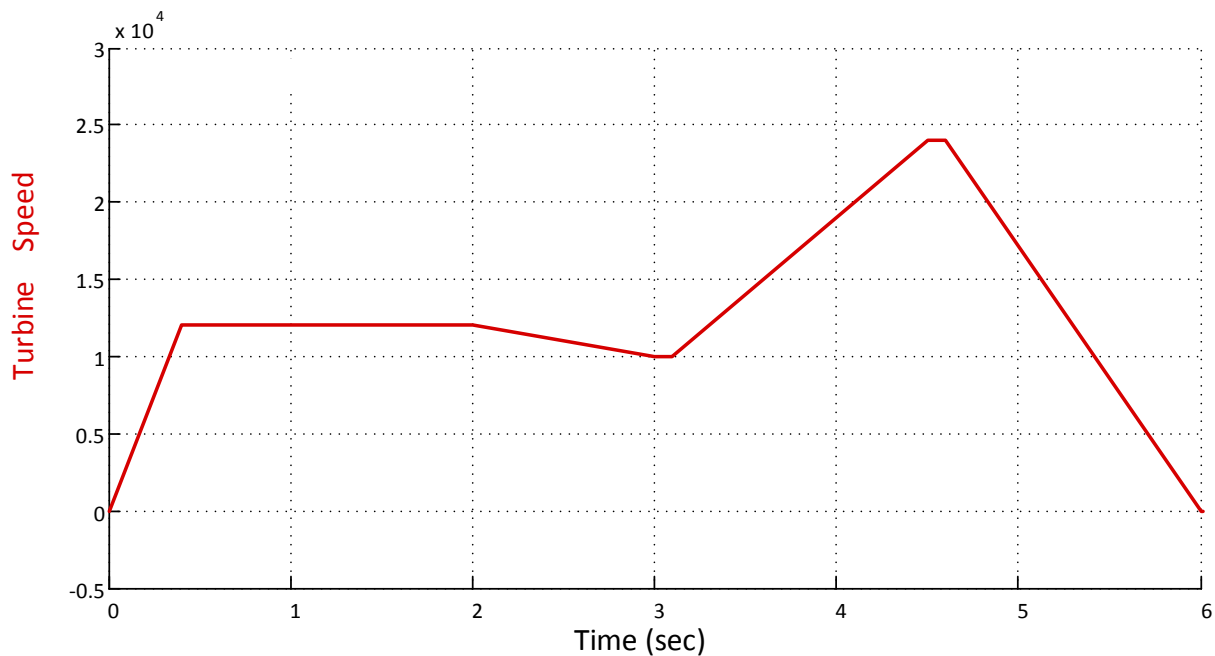

Figure 4-4: Turbine Speed

84

4.3 SIMULATION RESULTS

In order to render the simulation close to reality, Matlab/Simulink has been setup to run at a Fixed-Step Discrete solver, with $fs = 100kHz$ sampling rate, this rate representing the power and the control variables with fidelity. Figure 4-5 shows the frequency tracking response of the Kalman Filter Phase-Locked Loop (KF-PLL).
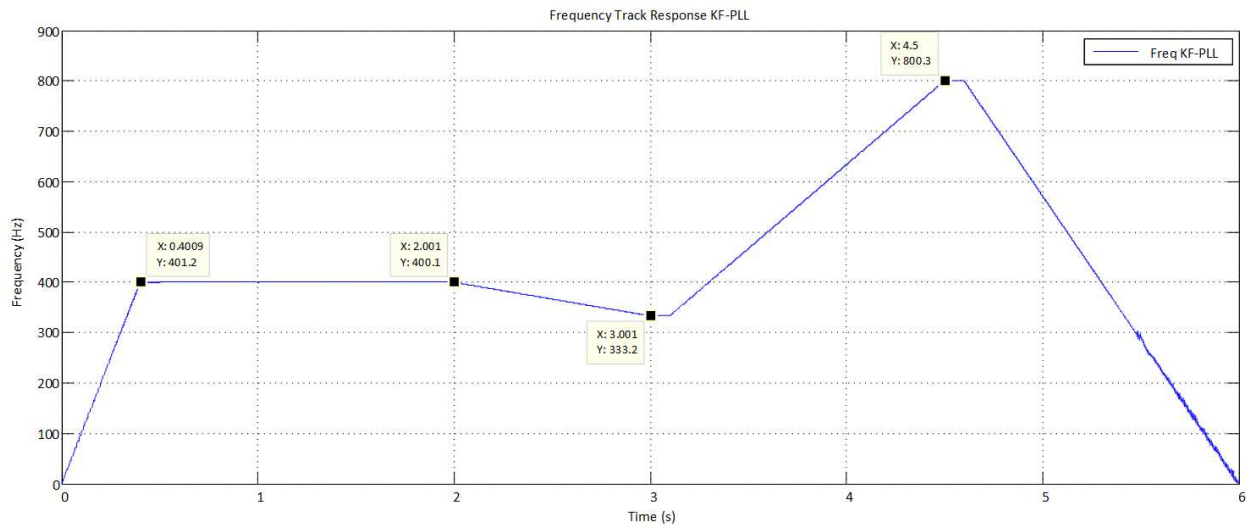

Figure 4-5: Response of the KF-PLL

As the KF-PLL frequency response is very faithful, so is the synchronization signal. As shown by the data tips, the KF-PLL could track the system frequency variations as well as reject the voltage ripple in an accurate manner.

Figure 4-6 shows the AEPS and AAPF voltages and currents at $400Hz$, it is shown in detail the moment when the AAPF is activated, at $t = 0.5s$.
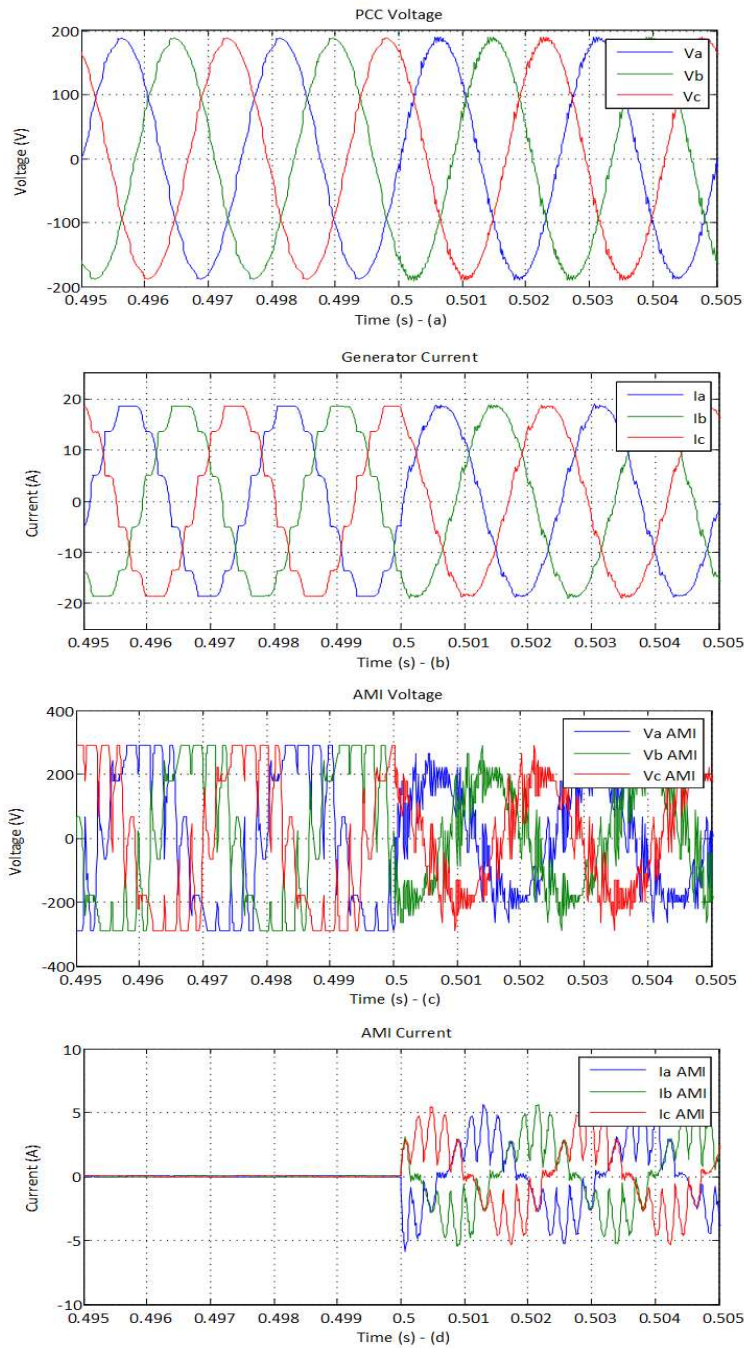
Figure 4-6: AEPS and AAPF Waveforms (400Hz)

Inspecting Figure 4-6-b, it is possible to see that the AAPF mitigates the distortion. Nonetheless, the voltage, shown in Figure 4-6-a has low ripple, this is due to the waveform of the AAPF voltage, presented in Figure 4-6-c. Hence, the harmonics and power factor are compensated with the generation of the compensation currents, Figure 4-6-d.

86

Through the harmonic spectra shown in Figure 4-7 and Figure 4-8, it is observed that the AAPF reduces the THD (Total Harmonic Distortion) of the PCC voltage from 2.46% to 2.44%, while the current THD is reduced from 7.91% to 3.53%.

It is important to remark that the active power was $5210W$ before and $5250W$ after connection of the AAPF. This verifies that the AAPF is mitigating basically the non-active power.
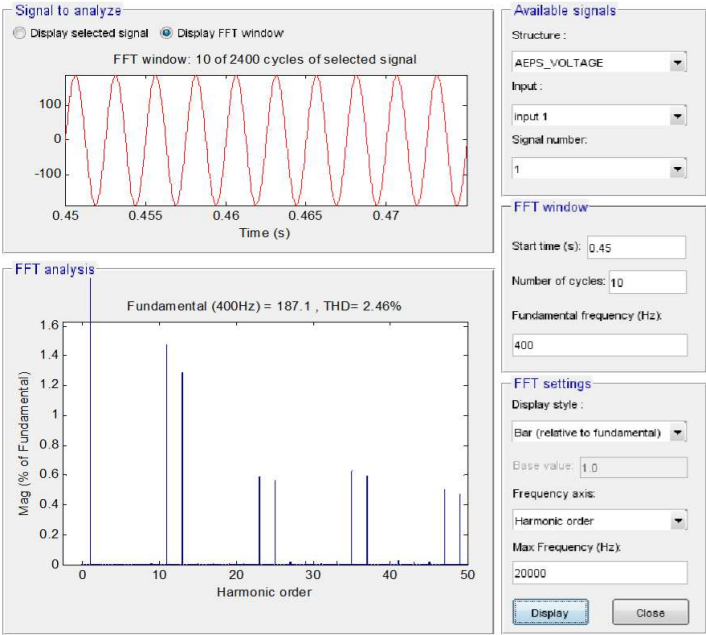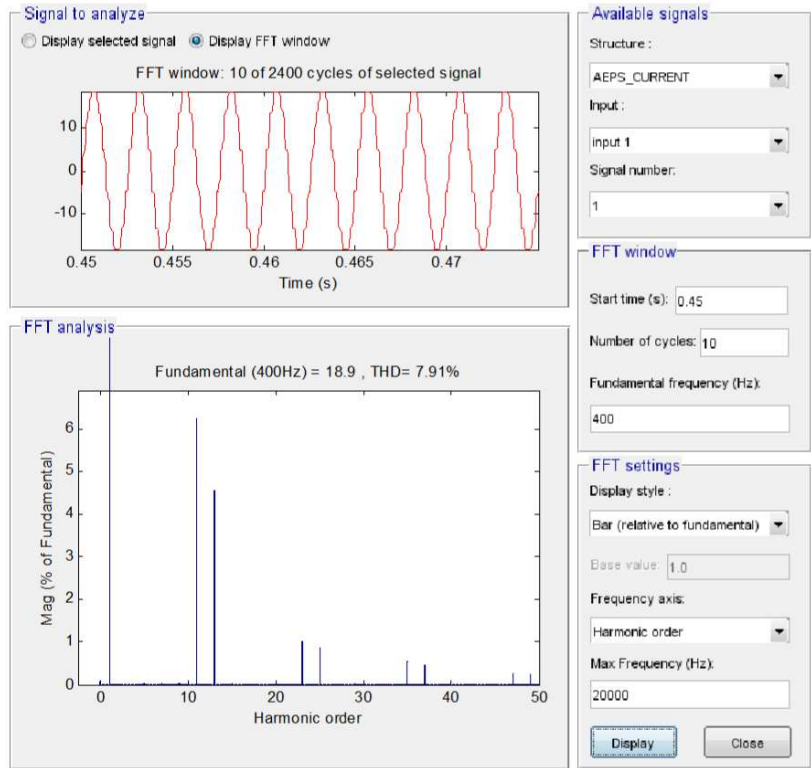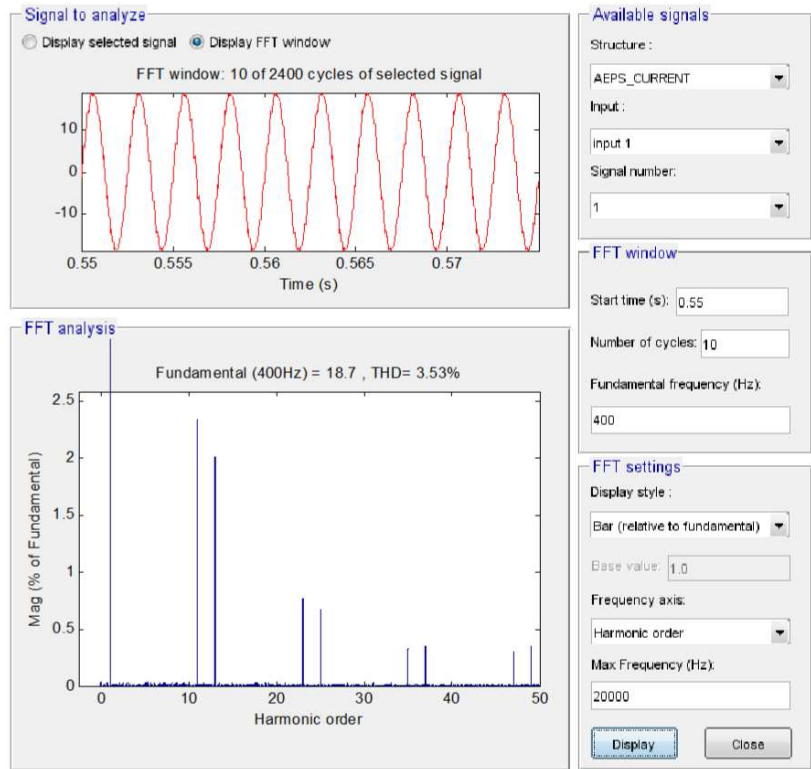

a) Voltage Spectrum before Filtering
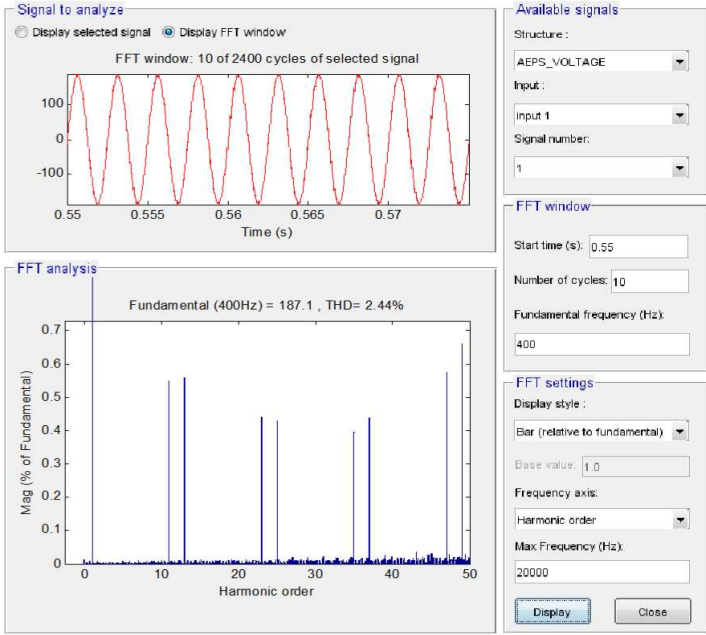
b) Voltage Spectrum after Filtering

Figure 4-7: Harmonic Spectra of the AEPS (400 Hz)

a) Current Spectrum before Filtering

b) Current Spectrum after Filtering

Figure 4-8: Harmonic Spectra of the AEPS (400 Hz)

88

Figure 4-9 shows the AEPS and AAPF voltages and currents at $333.3\,Hz\,(t = 3\,s)$. It is shown in detail that the AAPF tracking system and control remain working properly.
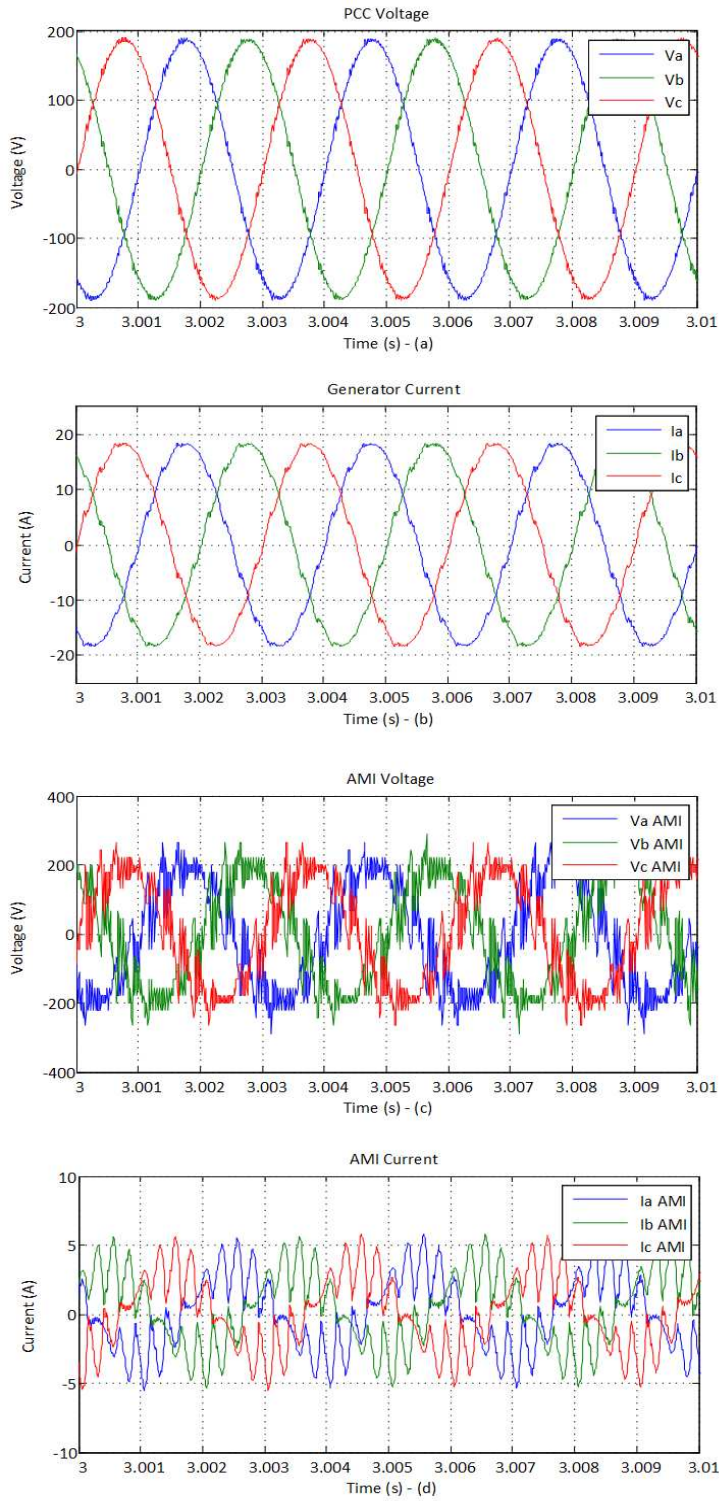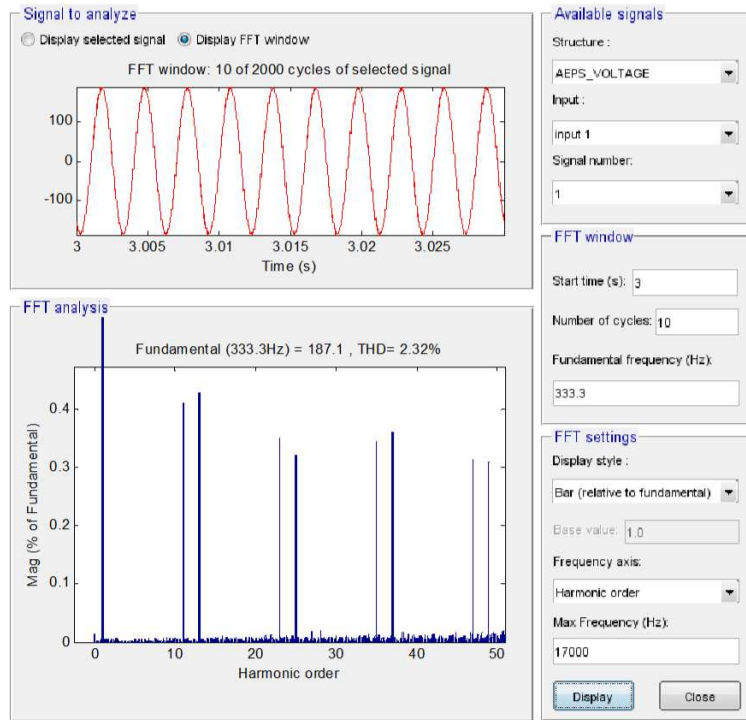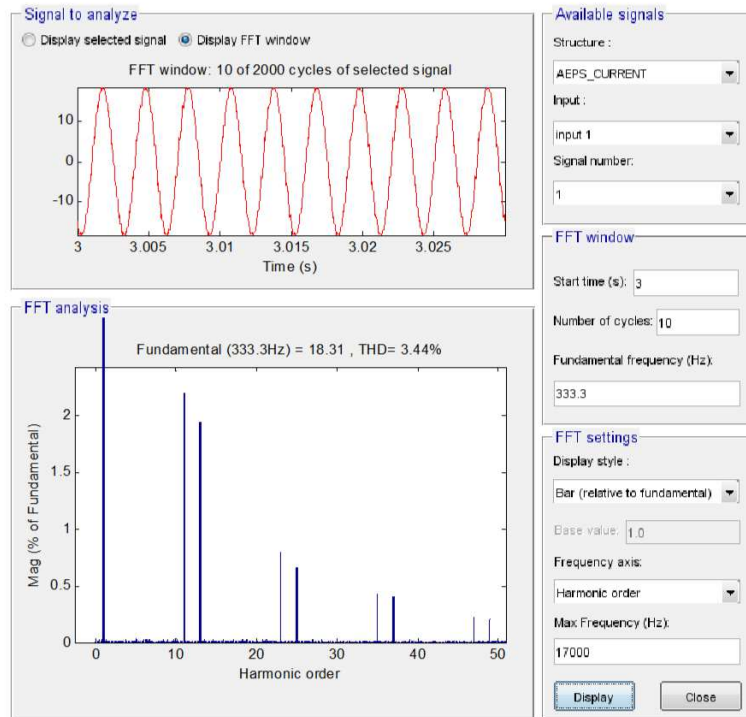

Figure 4-9: AEPS and AAPF Waveforms (333,3 Hz)

Through the harmonic spectra shown in Figure 4-10, it is observed that the THD of the PCC voltage is 2.32%, while the current THD is 3.44%.

a) Filtered Voltage Spectrum at 333.3Hz

b) Filtered Current Spectrum at 333.3Hz

Figure 4-10: Harmonic Spectra of AEPS (333.3Hz)

Figure 4-11 shows the AEPS and AAPF voltages and currents at $800Hz$ ($t = 4.5\,s$), it is shown in detail that the AAPF tracking system and control remain working properly.
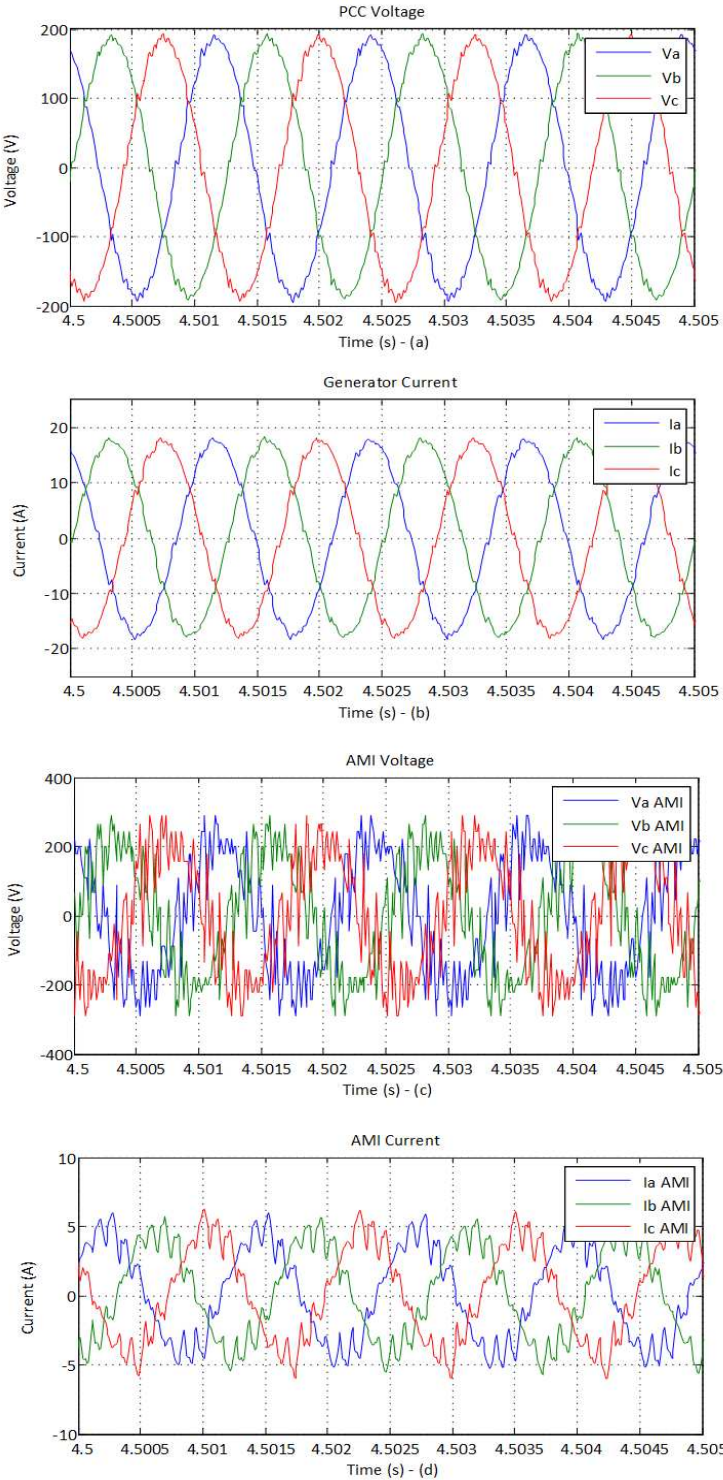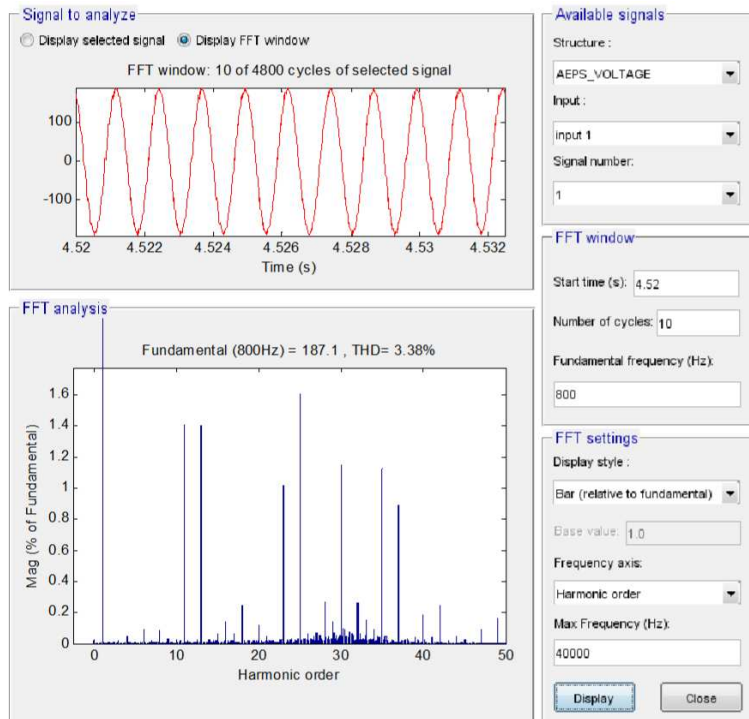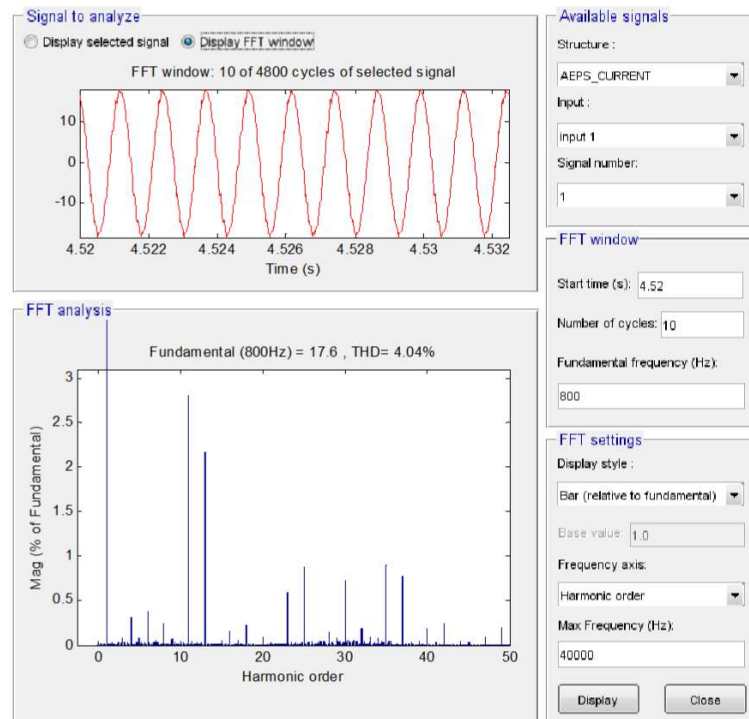

Figure 4-11: AEPS and AAPF Waveforms (800 Hz)

Through the harmonic spectra shown in Figure 4-12, it is observed that the THD of the PCC voltage is 3.38%, while the current THD is 4.04%.

a) Filtered Voltage Spectrum at 800Hz

b) Filtered Current Spectrum at 800Hz

Figure 4-12: Harmonic Spectra of AEPS (800Hz)

Table 2-2), the TDH$_v$ must be less than 5%. Therefore the proposed AAPF makes the AEPS meet the minimum distortion factor requirements.

Moreover, according to Table 2-3, the AAPF succeeds to reach the compliance of the THD$_i$ for all harmonic orders.

The power factor (PF) of the system remains stable and close to 1 during the period witch the filter remains connected to the PAC. Equation (4-1) shows the PF formula and Figure 4-13 shows the PF of the filter during the simulation time.

$$PF = \frac{P}{S}$$
(4-1)

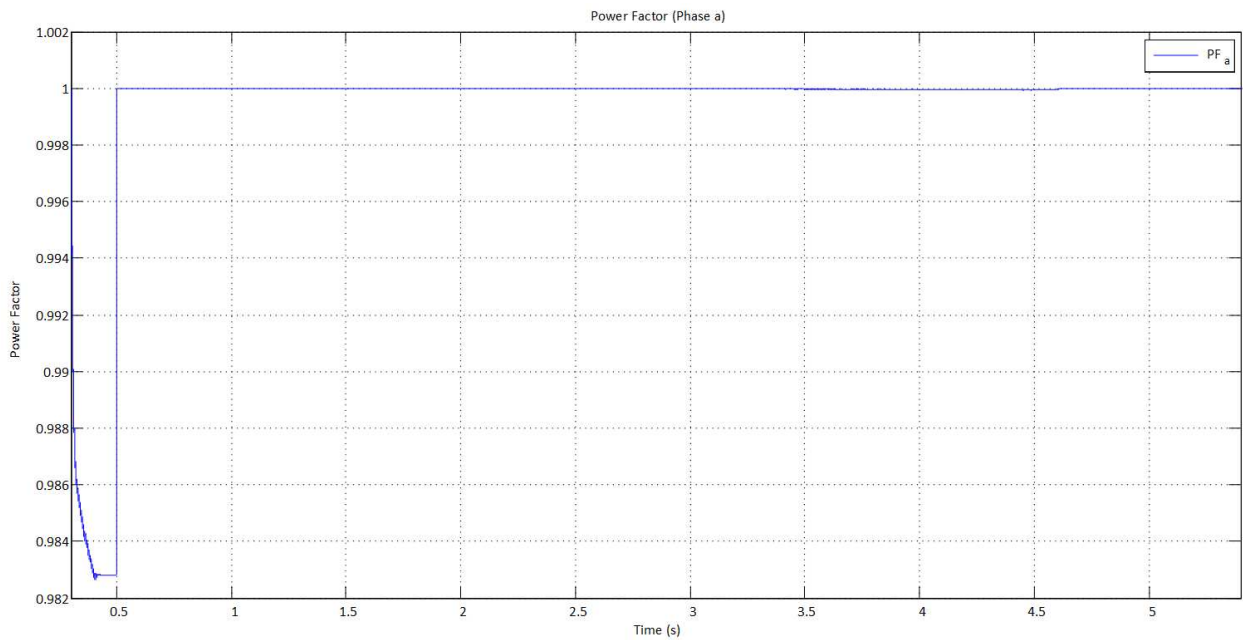Where, P, defined in (3-8) is the active is power, and $S = V \cdot I$, is the apparent power.

Figure 4-13: Power Factor during the simulation

Inspecting Figure 4-13, the PF remains around 0.982 before $0.5s$, once the AAPF is connected to the system it increases to values close to 1, therefore reaching the power factor limits of Table 2-4.

4.4 CONCLUSIONS

The simulation results clearly show that the control system applied to the AAPF can actually provide an overall good dynamic response for all system frequencies. After validating the control algorithm by Software in the Loop (SIL) simulation, therefore validating the C code generated by Matlab/Simulink Embedded Coder, a prototype of an AAPF was built in laboratory. Chapter 5 presents details of the AAPF prototype.

5 PROTOTYPE EXPERIMENTS

The development of the Aeronautical Active Power Filter (AAPF) prototype was done in two steps: first, a single-phase low power setup, which proved the feasibility of the AAPF, and finally a three-phase, four-wire setup.

5.1 SINGLE-PHASE AAPF

5.1.1 Prototype Description

Figure 5-1 shows the laboratory prototype is composed by three SEMIKRON modules: one SEMIX453GB12E4S for the high voltage cell, one SEMIX202GB12E4S for the middle voltage cell and one SK260MB10 for the low voltage cell.
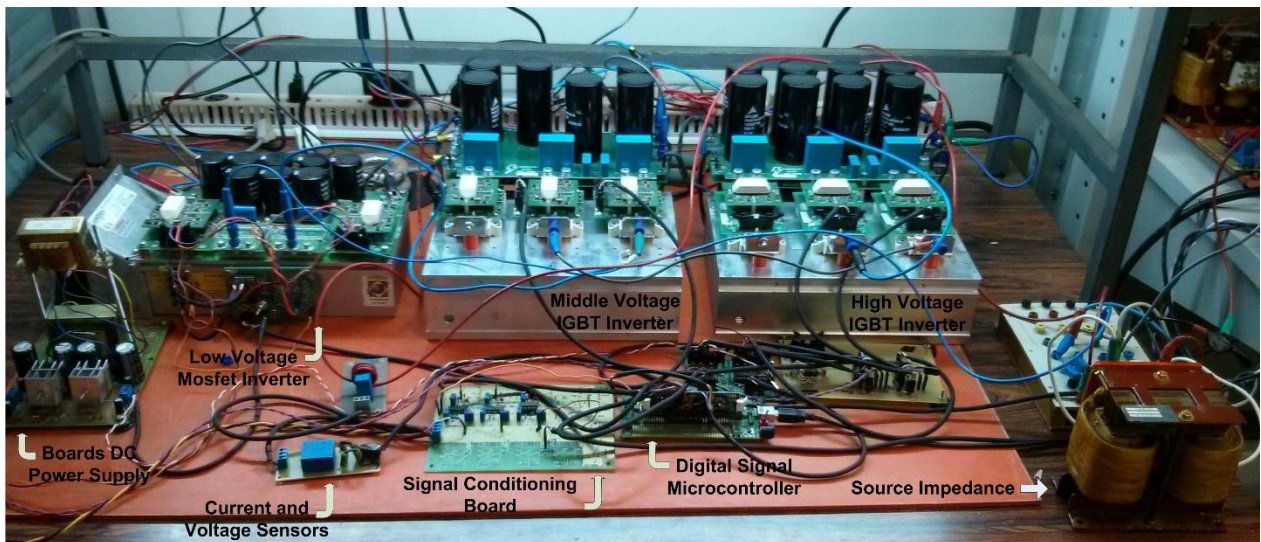

Figure 5-1: Single -Phase AMI

The schematic diagram of the prototype is presented in Figure 5-2. Table 5-1 contains the parameters. The Aircraft Power Supply is emulated by a California Instruments variable frequency power source (v_s).

The voltages and currents are sensed by LEM Hall Sensors and connected to a Texas Instruments DSP TMS320F28335 through a signal conditioning board. All control functions and protection are done, either embedded in the control card and via analog control chips. A drive board is placed for each cell, for connection of the gate driver to the DSP.
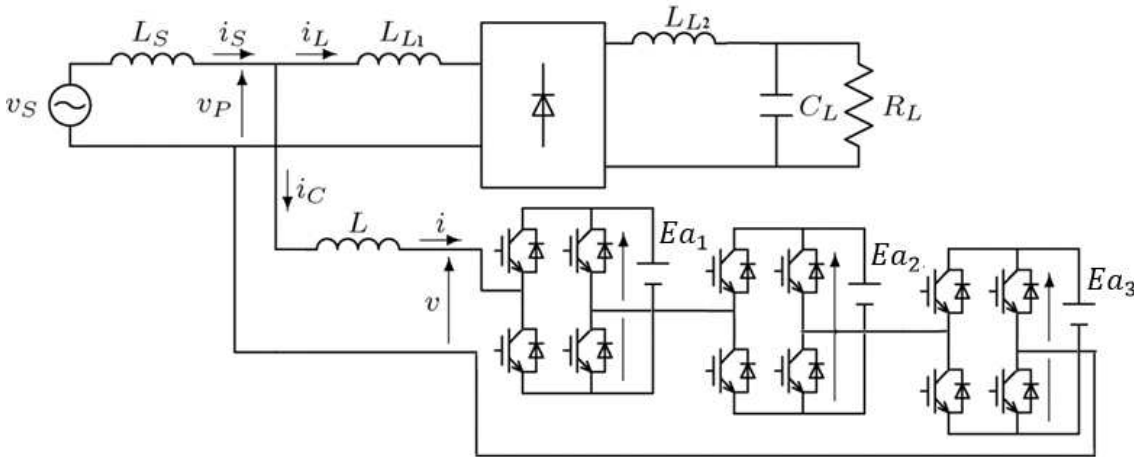
Figure 5-2: Single-Phase AAPF Prototype setup

The parameters of the single-phase AAPF are shown in Table 5-1.

Table 5-1: Parameters of the single-phase Prototype

Variable	Parameters
Phase to Ground Voltage	$50\ Vpeak$
Nominal Frequency	$100Hz$
Ls	$1.5mH$
L_{L1}	$4.58mH$
L_{L2}	$1.5mH$
C_L	$470\mu F$
R_L	250Ω
L	$4.25mH$
$(Ea_1; Ea_2; Ea_3)$	$(4.4; 13.3; 40)V$

5.1.2 Digital Control System

A control system was developed in Matlab/Simulink for the single-phase implementation. Figure 5-3 shows the control system.
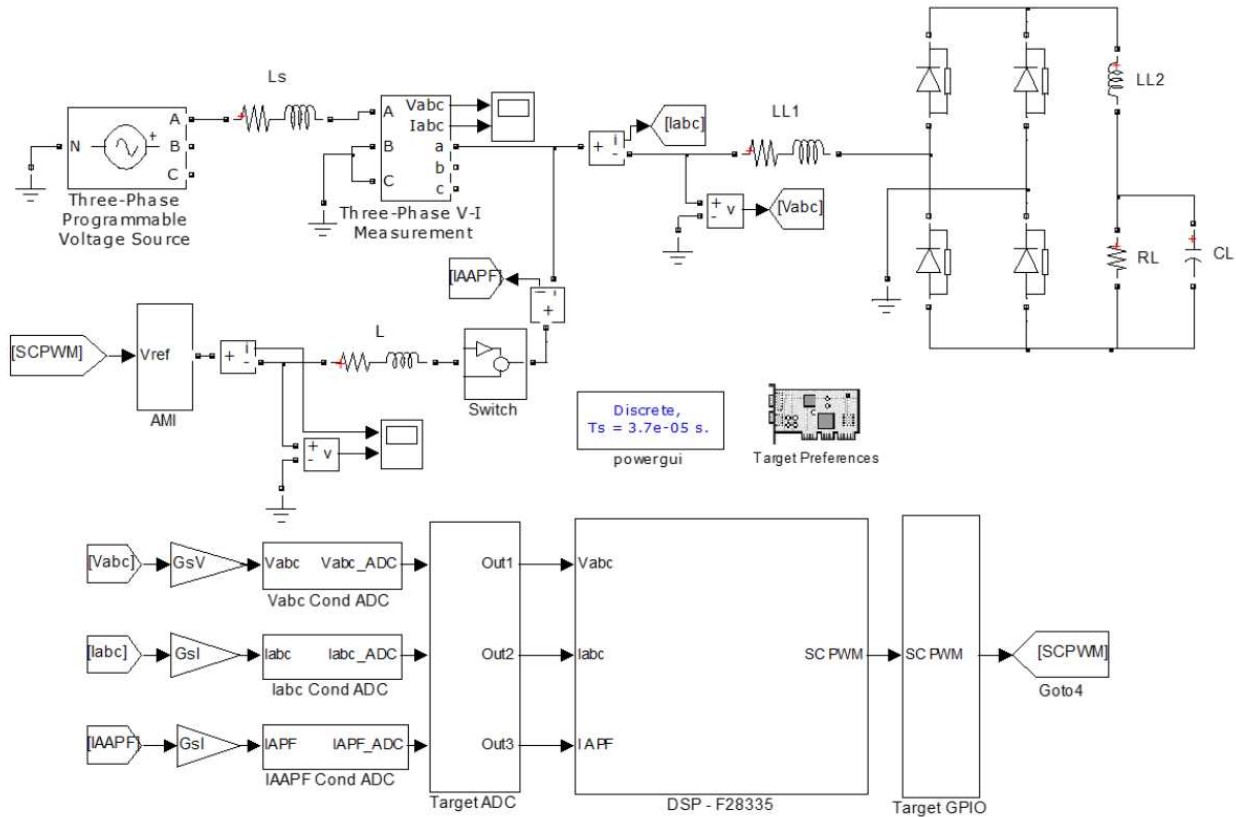

Figure 5-3: Single-Phase Control System Setup

For single-phase implementation the control system was not setup in the park reference frame, therefore no synchronization by PLL is needed. Figure 5-4 shows details of the block "DSP – F28335".
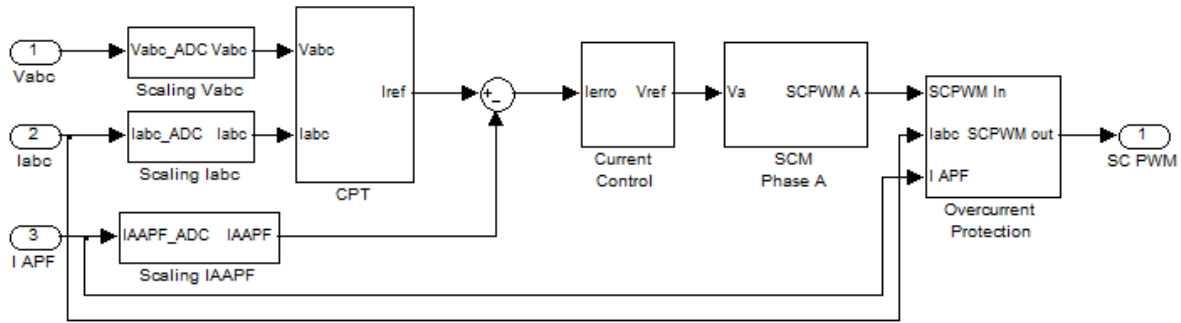
Figure 5-4: Single-Phase Control System

The control system diagram was used to generate the code for a TMS320F28335 microprocessor. Matlab/Simulink can generate the maximum execution time of the code by running it in the target. The maximum execution time of the code was $35.87\mu s$. Therefore, the ADC Sampling time and maximum switching frequency is defined as $Ts = 37\mu s$ in the simulation.

A new controller was calculated based on the values of Table 5-1 and the formulas of section 3.3. The new transfer function is shown in (5-1).

$$G_i(s) = \frac{0.577}{S \cdot 4.25 \cdot 10^{-3} + 0.1} \tag{5-1}$$

Thus, the new controller is shown in (5-2).

$$\text{CPI}(z) = 108.258 + \frac{10.82 \cdot \text{Ts}}{z - 1} \tag{5-2}$$

5.1.3 Simulation

The simulation was done for $100Hz$ using the parameters given in the previous section. Figure 5-5 illustrates the moment when the single-phase filter is connected to the PCC.
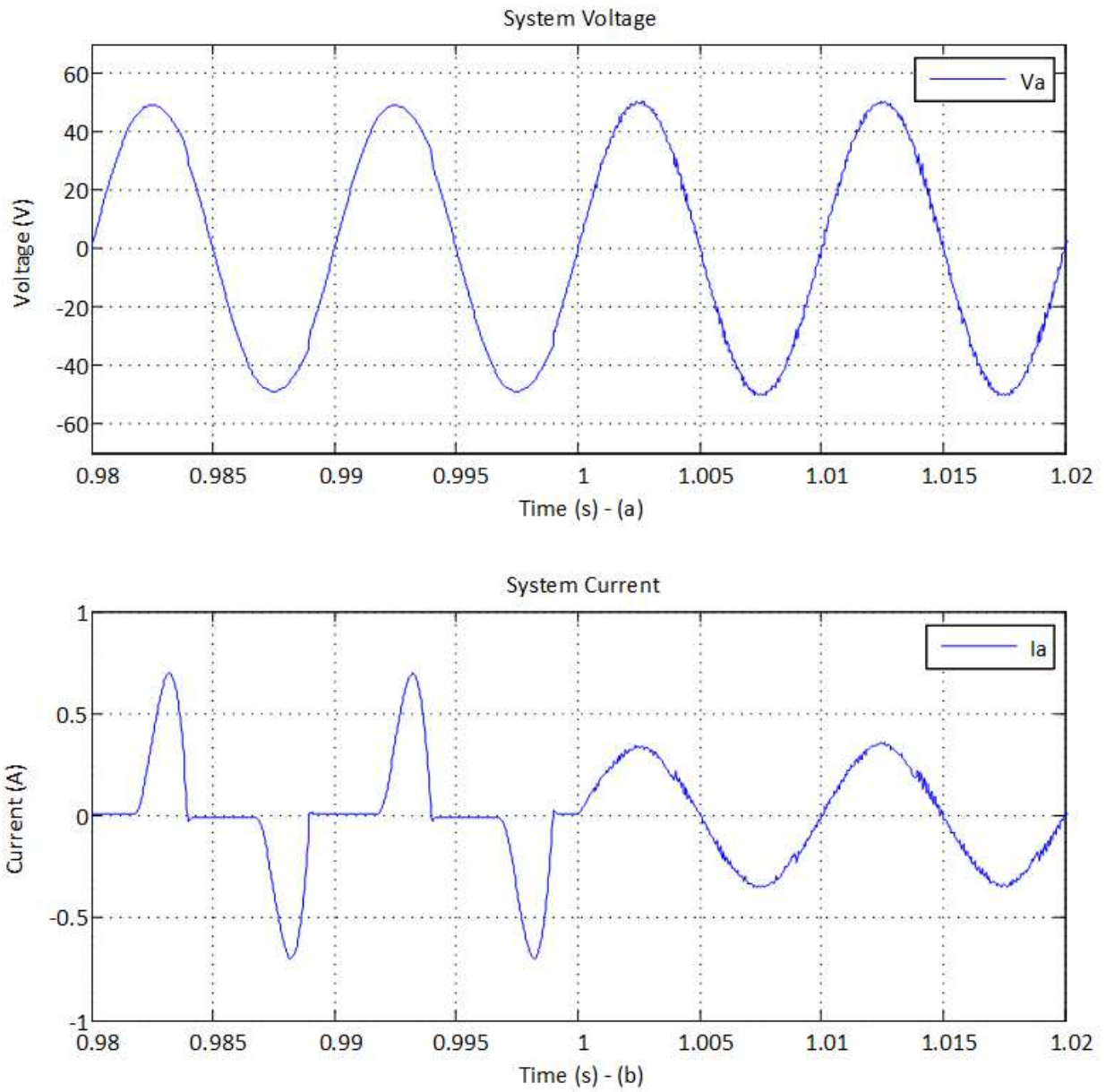
98

Figure 5-5: System Waveforms (Voltage and Current) - (100Hz)

The total harmonic distortion was reduced from 82.98% to 4.49%. Figure 5-6 shows the voltage and current in the active filter.

Figure 5-6: System Waveforms (Inverter Voltage and Current) - (100Hz)

The active power before and after $1s$ was $7.85W$ and $8.1W$ respectively. The active power validates the CPT and the PI tuning, as soon as very low active power is injected by the AAPF.

The simulation was equally done for $150Hz$. Figure 5-7 displays the moment when the single-phase filter is connected to the PCC.

Figure 5-7: System Waveforms (Voltage and Current) – 150Hz

The total harmonic distortion was reduced from 74.73% to 5.33%. Figure 5-8 shows the voltage and current in the active filter.
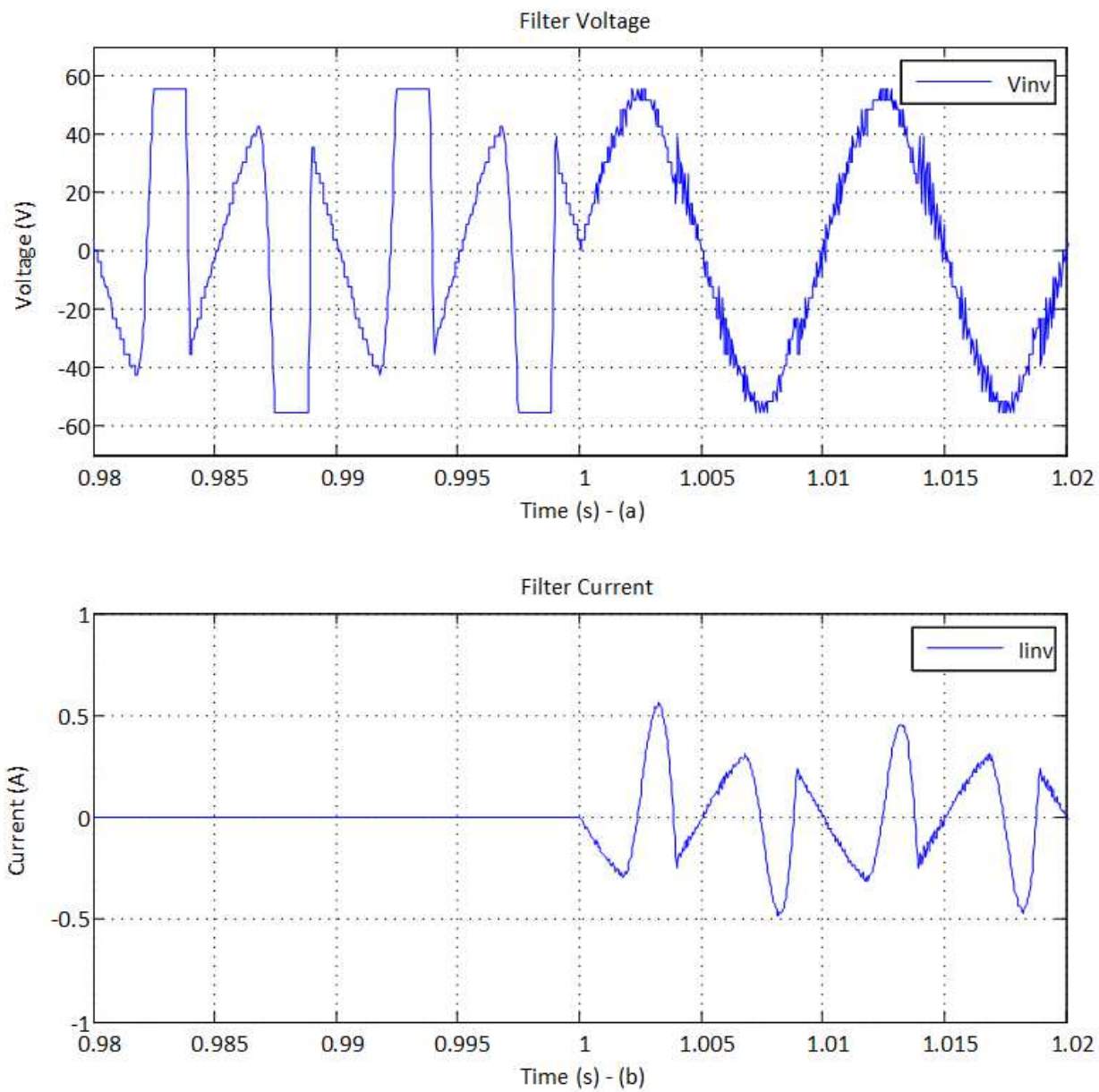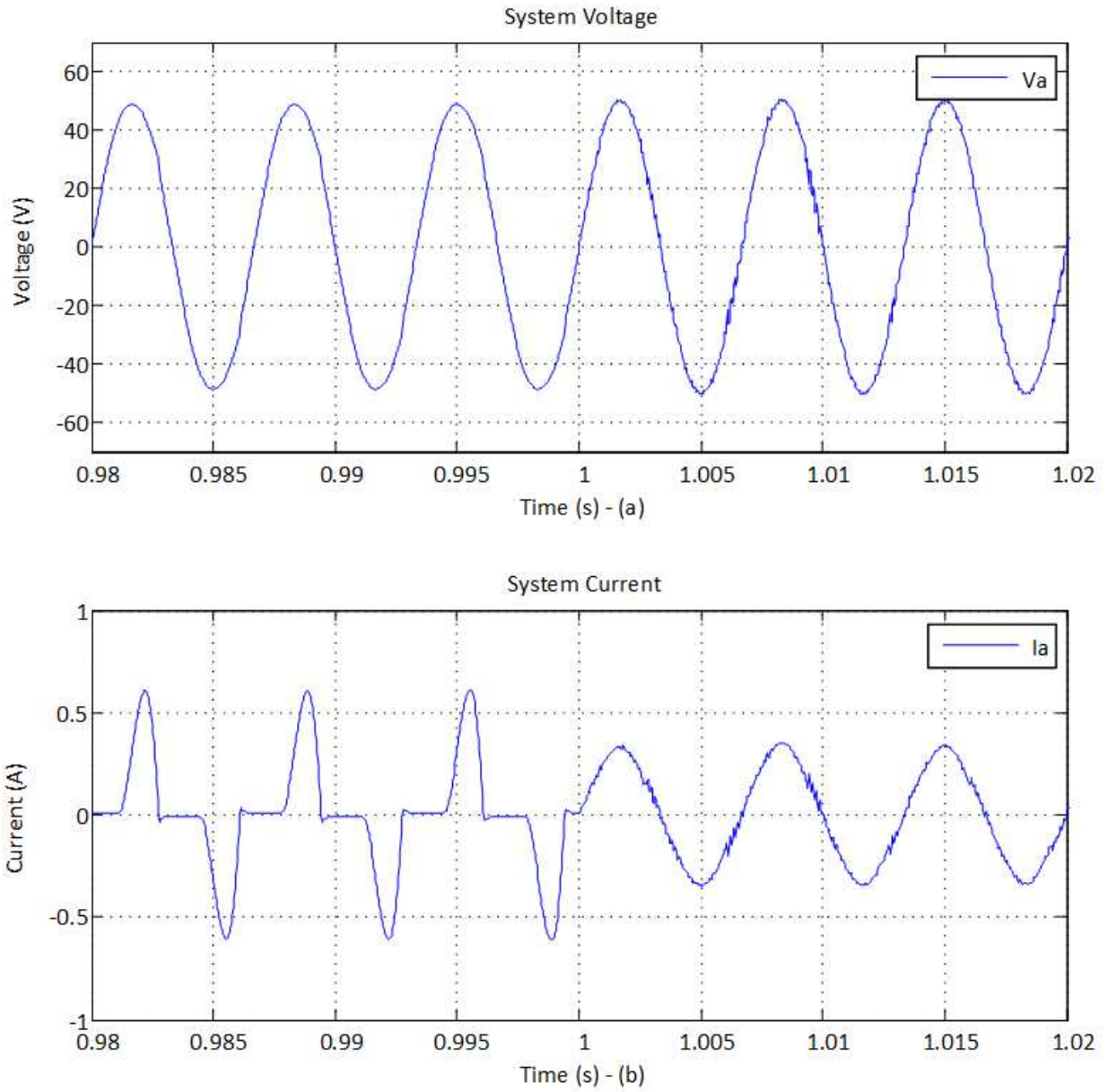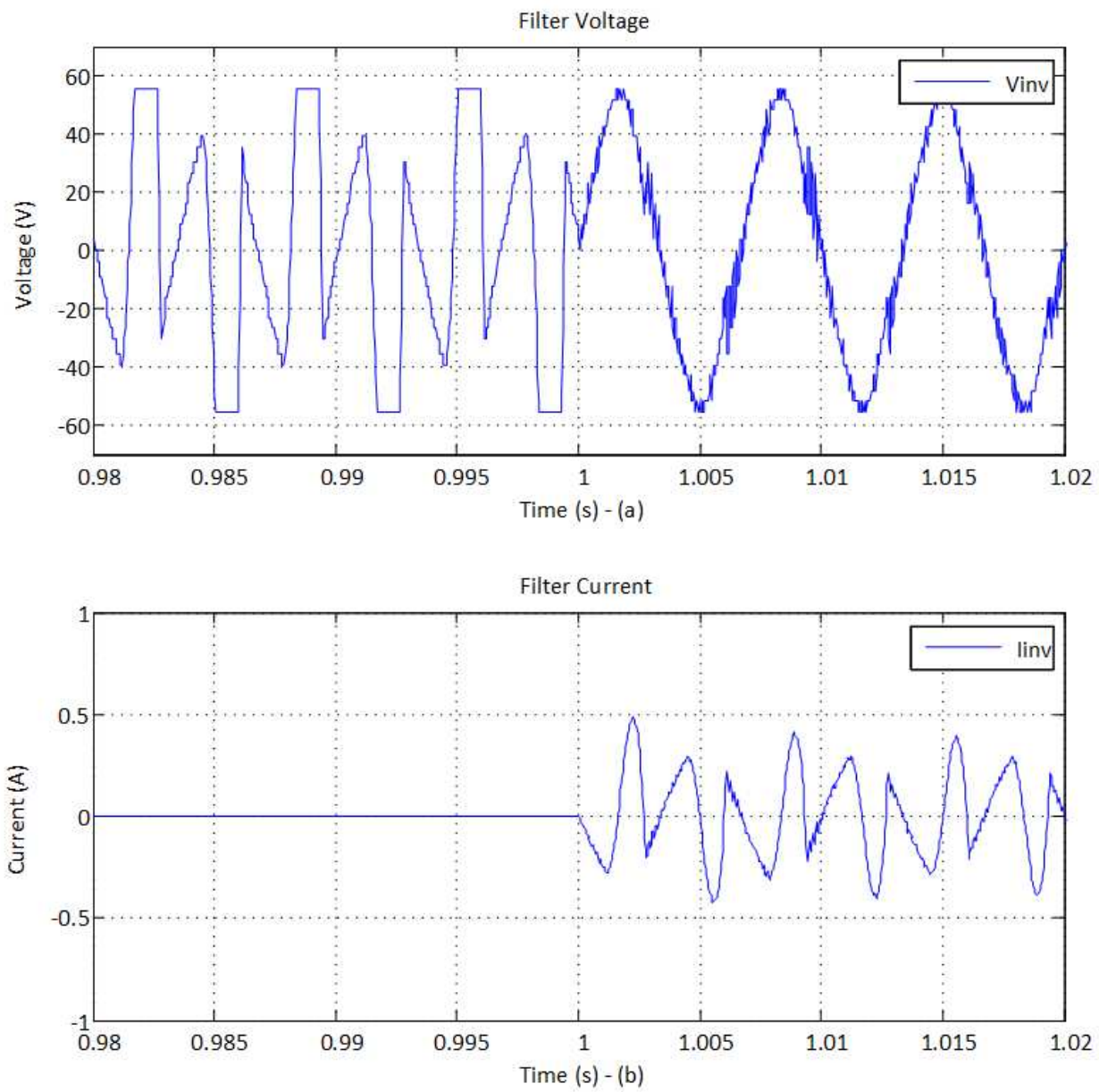
Figure 5-8: System Waveforms (Inverter Voltage and Current) – (150Hz)

The active power before and after $1s$ was $7.45W$ and $7.9W$ respectively. It is important to remark that the simulations was done once at $100Hz$ and once at $150Hz$.

5.1.4 Single-Phase Prototype Case Study

Since the switching frequency of each inverter cell is very different, the algorithm execution was limited to $27kHZ$. This limits the switching frequency of the lower voltage module, which can switch at up to $50kHz$. The system waveforms were obtained by an Agilent Oscilloscope.

The experiment shows comprehensive filtering at $100Hz$. Figure 5-9 shows the load current (i_L), source current (i_S) and source voltage (v_S). Figure 5-10 shows the AAPF current (i_C) and voltage (v).
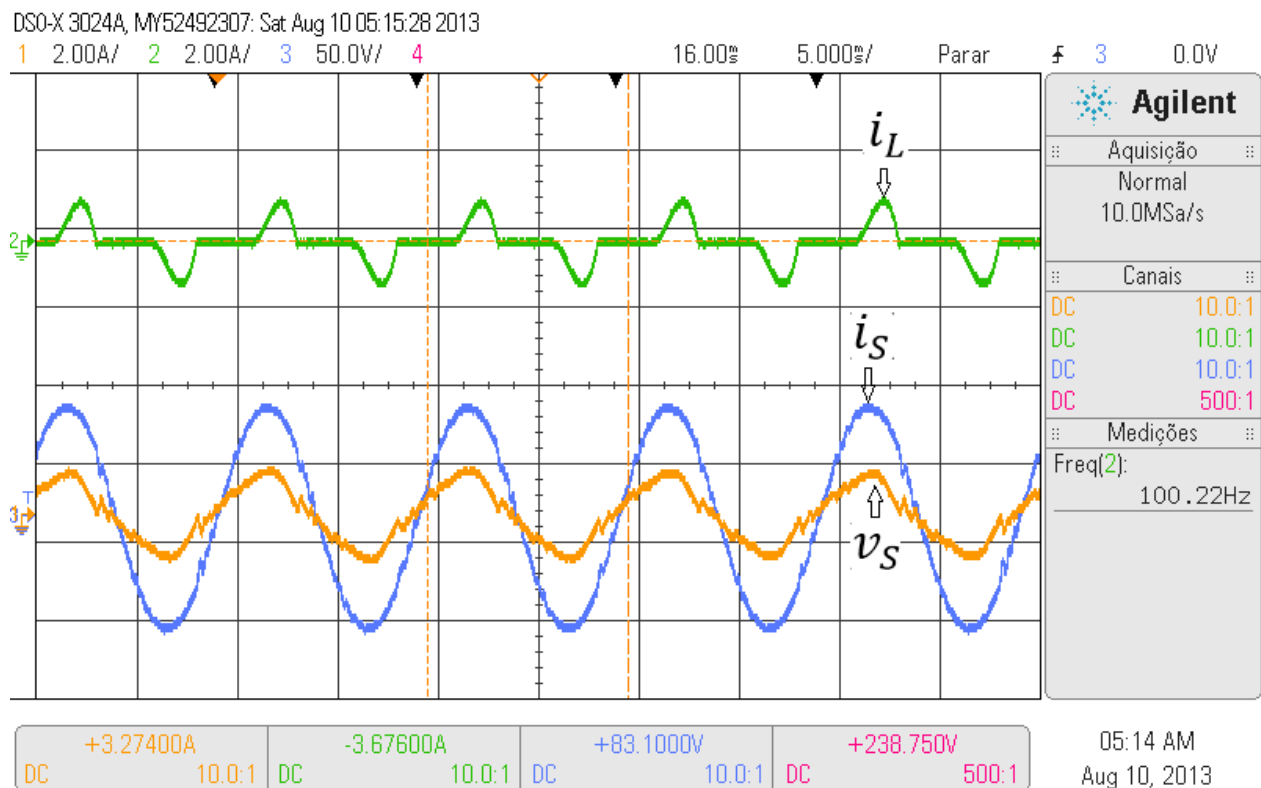

Figure 5-9: System Waveforms (Voltage and Currents) – (100Hz)

It is observed that the AAPF succeed to filter the currents, the THD is mitigated and the reactive energy is compensated. Due to the staircase modulation low voltage ripple is injected.
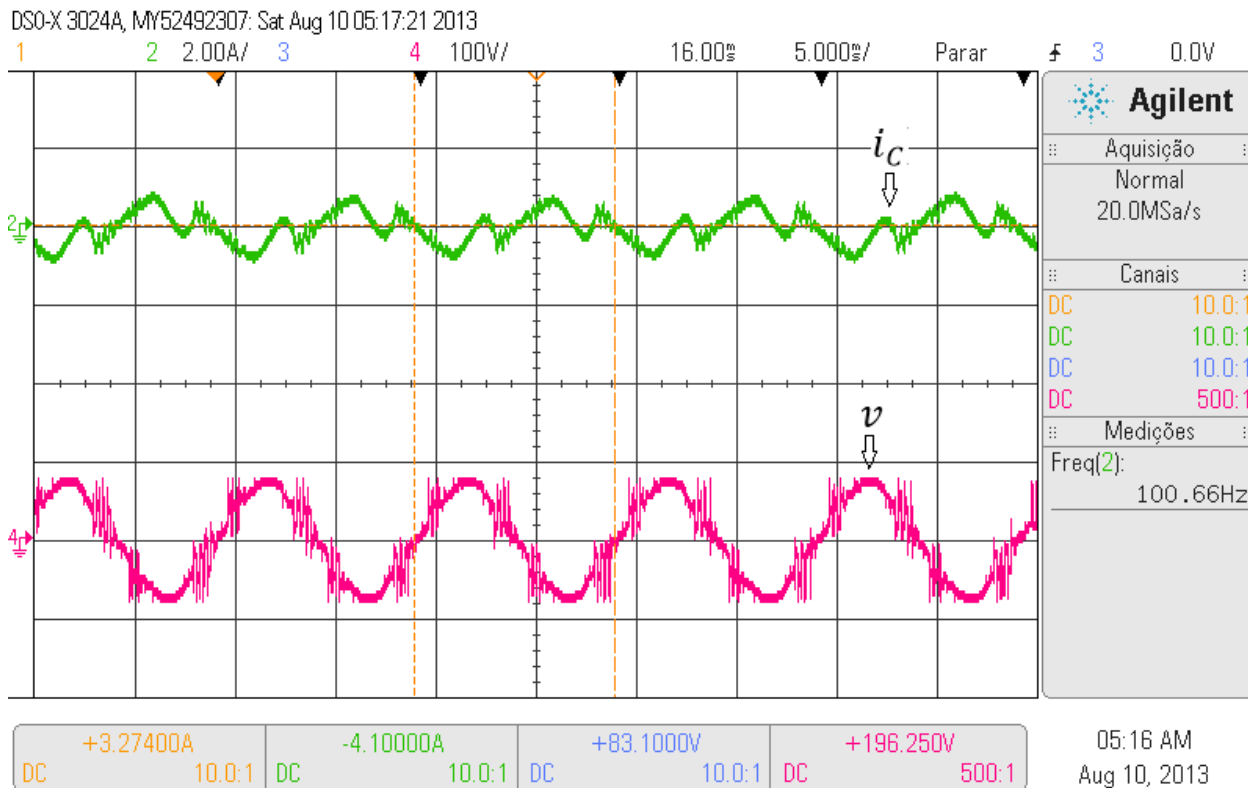
Figure 5-10: System Waveforms (Inverter Voltage and Current) – (100Hz)

The performance of the AAPF decreases when the frequency increase this is due to the PI controllers, which are not in a rotatory reference frame (Park transformation). The experiment shows comprehensive filtering at $150Hz$. Figure 5-11 shows the load current (i_L), source current (i_S) and source voltage (v_S). Figure 5-12 shows the AAPF current (i_C) and voltage (v).

It is observed in the prototype that the inverter voltage presents instability when the current crosses zero, therefore the filtering performance is weaker compared to the simulations. The switching frequency of $27kHz$, which is above the nominal to the IGBTs, may contribute to this characteristic.

Figure 5-11: System Waveforms (Voltage and Currents) – (150Hz)

At this time, the AAPF filters the currents, however the THD is less mitigated and the reactive energy is less compensated. Nevertheless, due to the staircase modulation very low voltage ripple is injected.
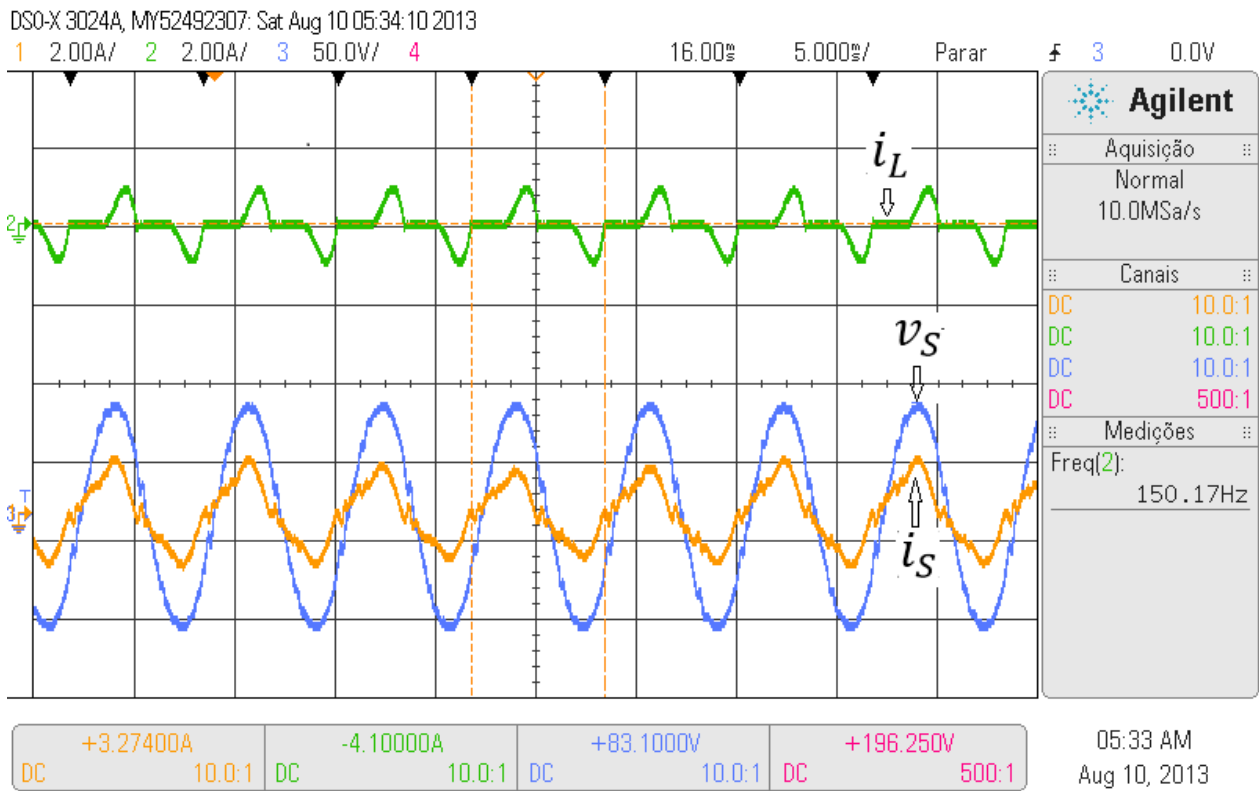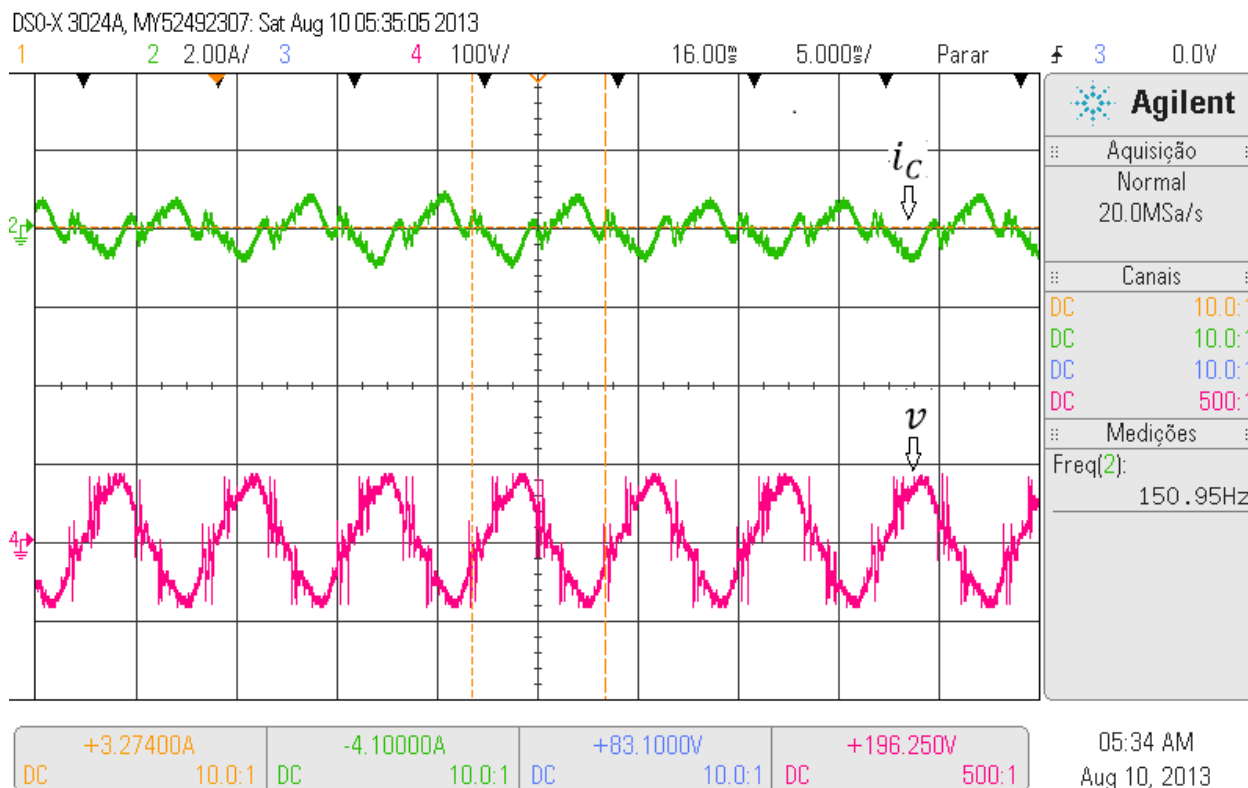
Figure 5-12: System Waveforms (Inverter Voltage and Current) – (150Hz)

In this test, the prototype presents the same drawback than in $100Hz$ fundamental, the zero crossing of the current stress the control, therefore the inverter voltage is compromised.

5.1.5 Conclusions

The single-phase configuration of Figure 5-2 limits the AAPF performance, due to the control algorithm. For the three-phase topology, the PI controller is placed in a rotating reference frame (by the use of the Park transformation). This technique increases the effectiveness of the control. However, in a single-phase configuration, the response of the control algorithm is affected by the fundamental frequency. The frequency sweep was done from $100Hz$ to $150Hz$ and equivalent filtering characteristics was obtained. Hence, better results are expected for the three-phase prototype, which is shown in the next section.

5.2 THREE PHASE AAPF

5.2.1 Prototype Description

A three-phase AAPF is built in the laboratory for testing in low power and low frequency, Figure 5-13. The laboratory setup is composed by:

- One California Instruments variable frequency power source;
- 9 Semix4 Semikron modules for implementing the Asymmetrical Multilevel Inverter (AMI);
- 9 Voltage sources to power the DC links of each cell;
- 9 Power resistors to burn regenerative energy of the DC links;
- One three-phase non-linear load;
- One Texas Instruments DSP (TMS320F28335);
- 9 DSP-Gate Driver interface boards to the Skyper Drivers;
- One signal conditioning boards with 9 channels and DC power supplies;
- 6 LEM Hall Effect current sensors;
- 3 LEM Hall Effect voltage sensors.

The laboratory prototype is shown in Figure 5-13, and more details are presented in appendix b.

One Texas Instruments DSP (TMS320F28335)
9 DSP-Gate Driver interface boards
One signal conditioning board
6 LEM Hall Effect current sensors
3 LEM Hall Effect voltage sensors

9 Semix4 Semikron Modules

California Instruments power source

9 Voltage Sources to Power the DC links

Three-Phase non-linear load

9 Power Resistors
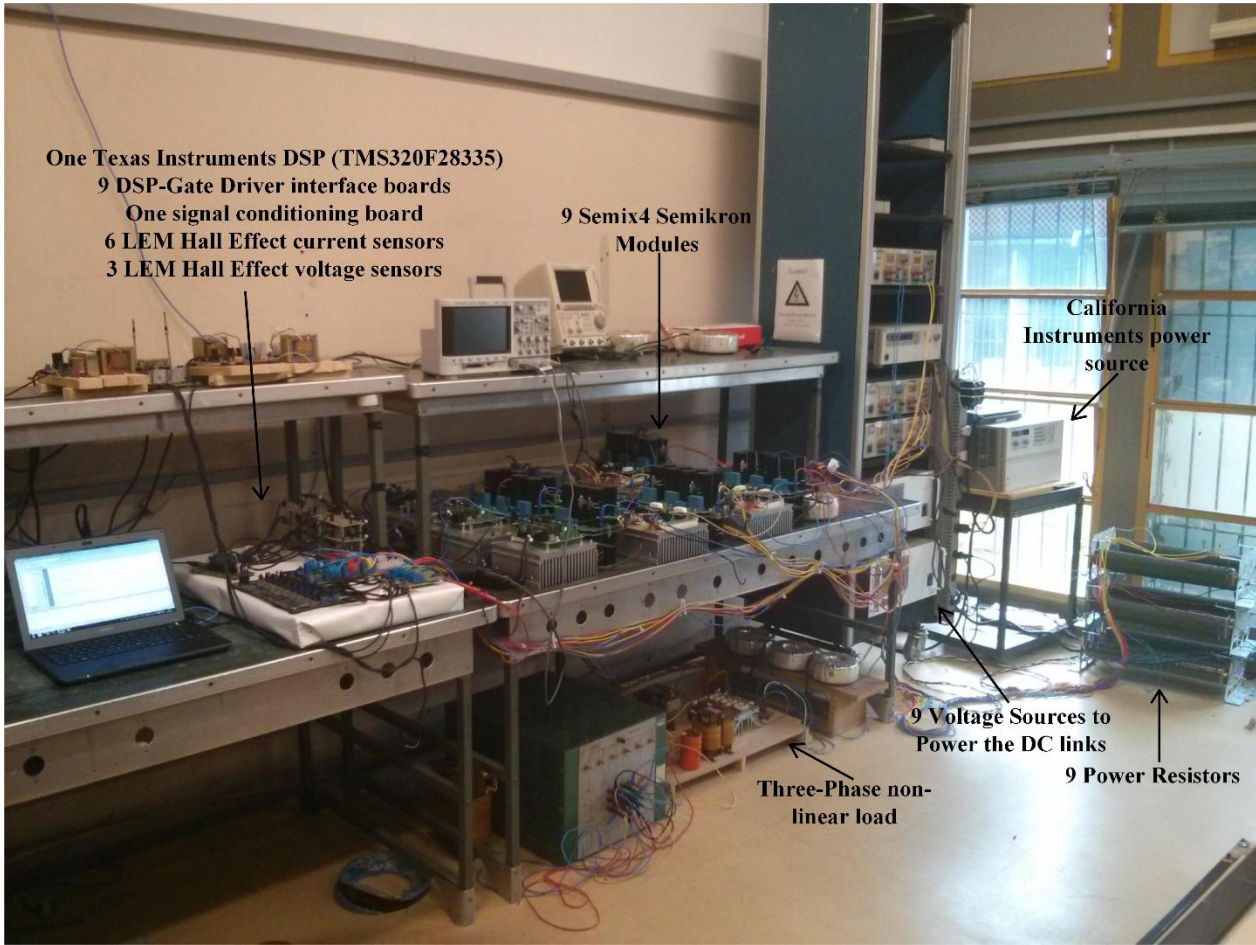
Figure 5-13: Laboratory Prototype

The hardware setup of the prototype is shown in Figure 5-14, Table 5-2 contains the parameters.

Figure 5-14: Hardware Setup of the Three-Phase AAPF Prototype

Table 5-2: Three-Phase Prototype Parameters

Variable	Parameters
Phase to Ground Voltage	$70V$rms
Nominal Frequency	$60Hz$
Ls	$0.001mH$
L_{L1}	$8.5mH$
L_{L2}	$4mH$
C_L	$16mF$
R_L	50Ω
L	$8.5mH$
$(Ea_1; Ea_2; Ea_3)$	$(11.11; 33.33; 100)V$

5.2.2 Digital Control System

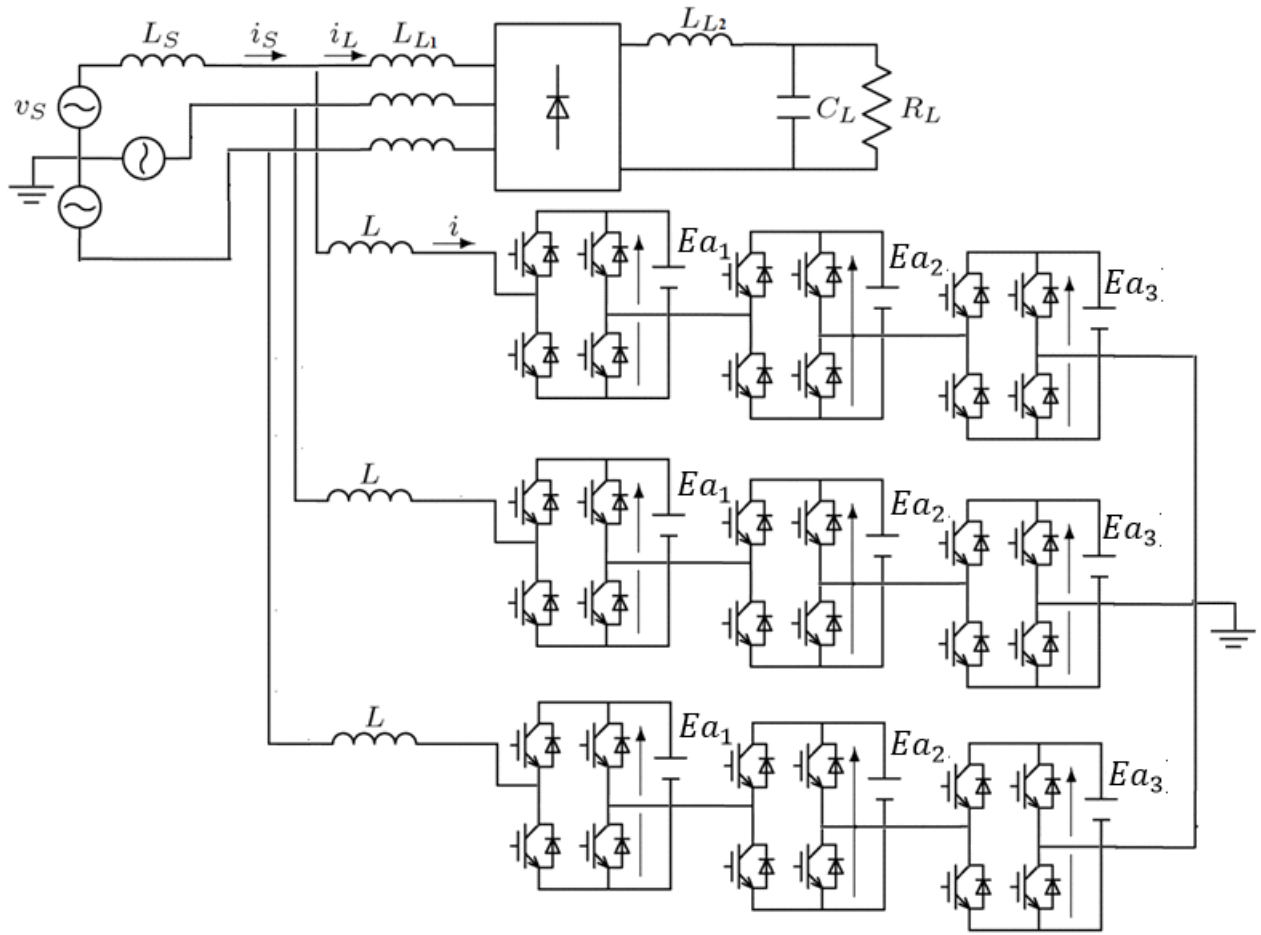The control system used for the firmware implementation is identical of the one described in section 4, yet with different controller parameters.

The control system diagram was used to generate code for a TMS320F28335 microprocessor. Matlab/Simulink can generate the maximum execution time of the code by running it in the target, the maximum execution time of the code was $109.17\mu s$. Therefore, the ADC Sampling time and maximum switching frequency is defined as $Ts = 110\mu s$ in the simulation.

A new controller was calculated based on the values of Table 5-2 and the formulas of section 3.3. The new transfer function is shown in (5-3).

$$G_i(s) = \frac{1,444}{S \cdot 8,5 \cdot 10^{-3} + 0,1} \tag{5-3}$$

The new controller is shown in (5-4).

$$\text{CPI(z)} = 86,52 + \frac{8,652 \cdot \text{Ts}}{z-1} \tag{5-4}$$

5.2.3 Simulation

Since low switching frequency $(\sim 9\,kHz)$ can be achieved, the simulation was done for $60Hz$ using the parameters given in the previous section. Figure 5-15 shows the moment when the AAPF is connected to the PCC.
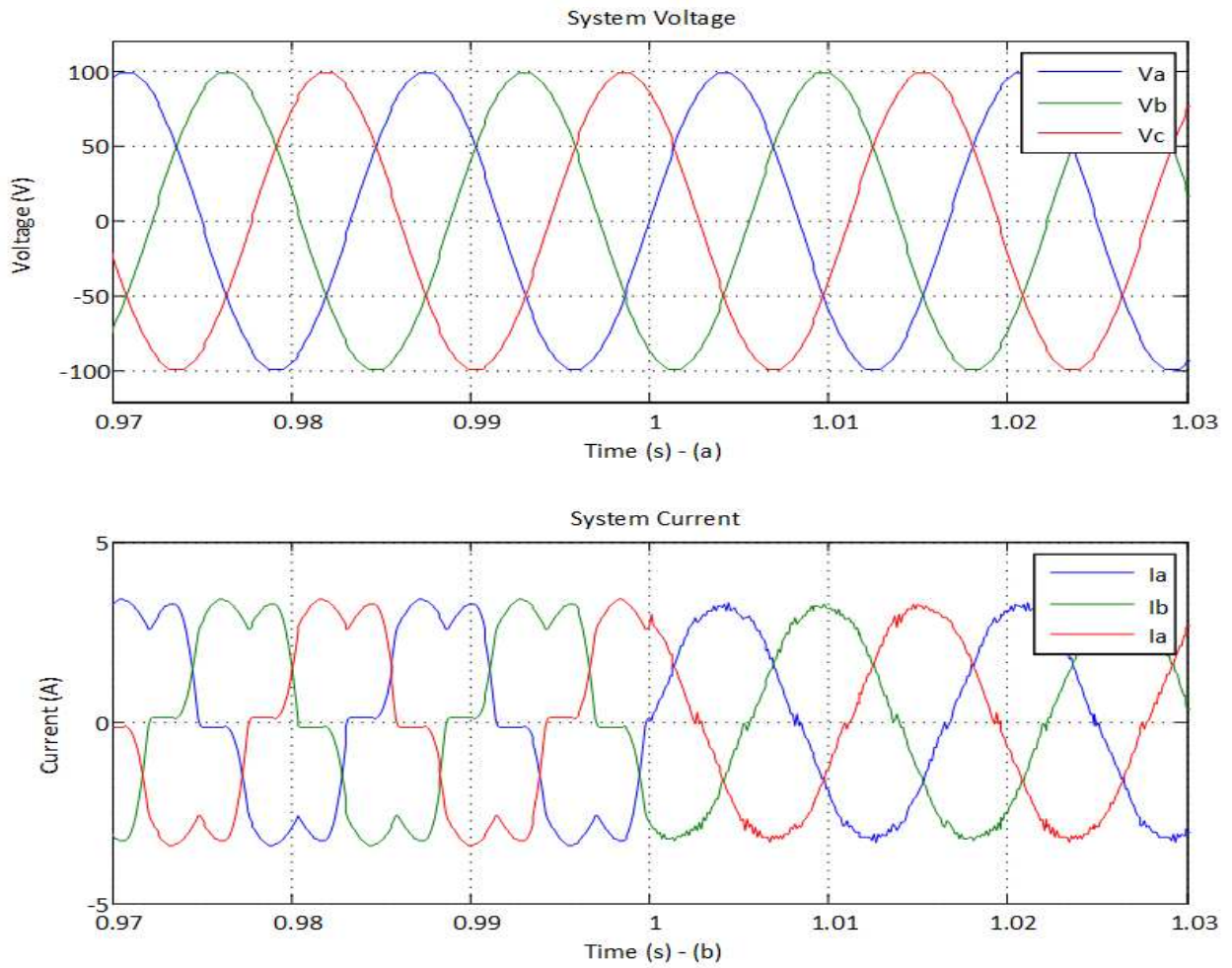
Figure 5-15: System Waveforms (Voltages and Currents) – (60Hz)

The total harmonic distortion was reduced from 23.17% to 4.7%. Figure 5-16 shows the voltage and current in the active filter.
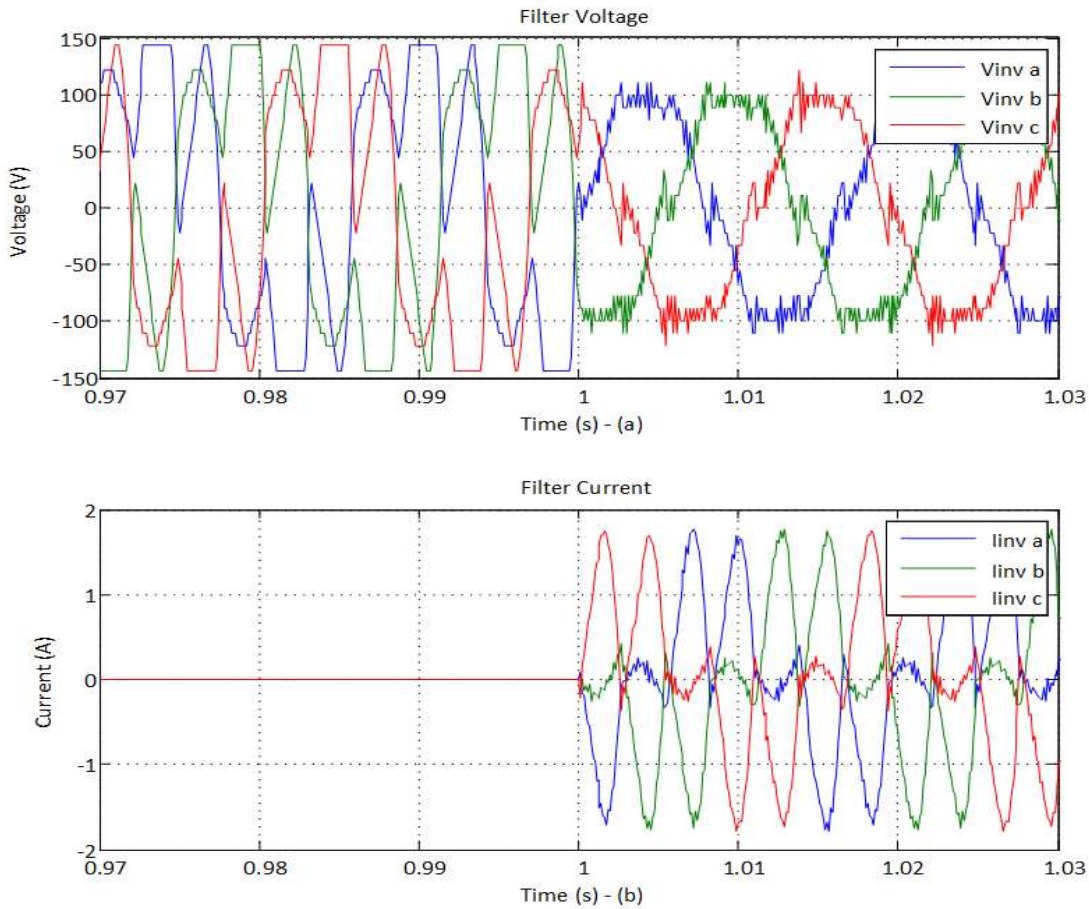
Figure 5-16: System Waveforms (Inverter Voltages and Currents) – (60Hz)

The active power before and after $1\ s$ was $479W$ and $483W$ respectively.

5.2.4 Three-Phase Prototype Case Study

5.2.4.1 Phase Locked-Loop

The Kalman Filter Phase-Locked Loop KF-PLL was tested in the physical prototype under variable frequency. Figure 5-17 shows the response of the KF-PLL tracking starting from $60\ Hz$ to $400\ Hz$ (the measurement tab shows the frequency of each waveform). The pink waveform is the PCC voltage and the synchronizing signal (yellow waveform) is obtained by means of a DAC, which is connected to the F28335 microprocessor thought a SPI channel.

112
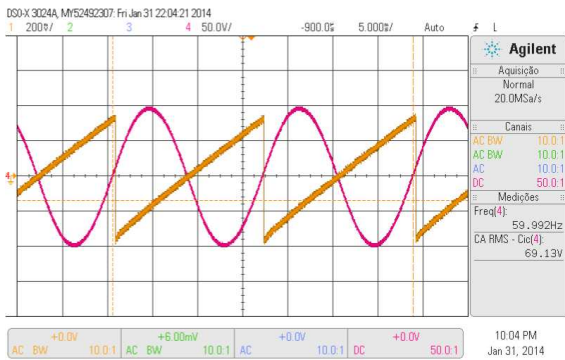
a) KF-PLL at 60Hz

b) KF-PLL at 100Hz
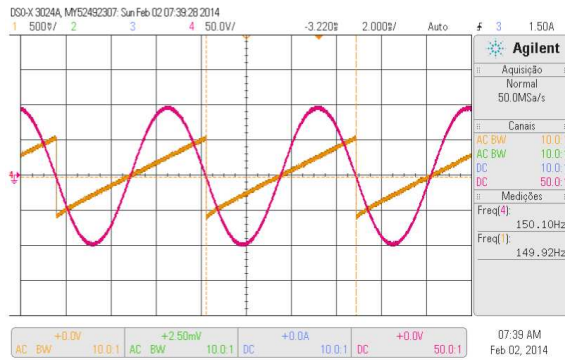
c) KF-PLL at 150Hz

d) KF-PLL at 2000Hz

e) KF-PLL at 250Hz
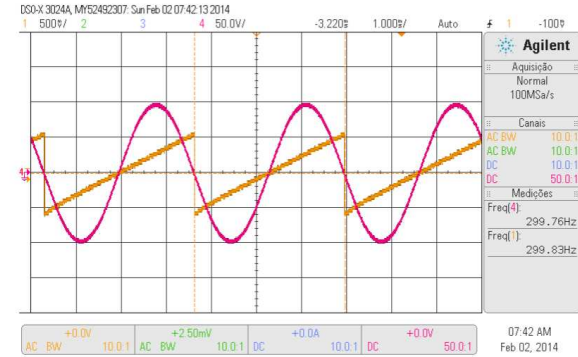
f) KF-PLL at 300Hz
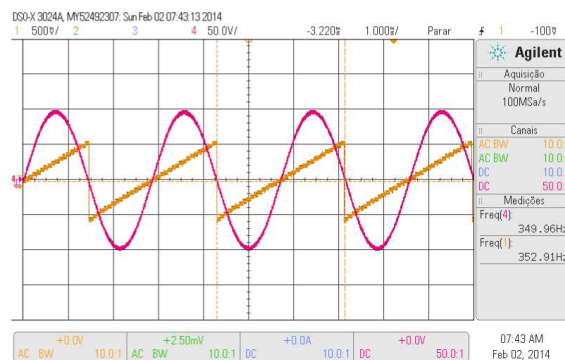
g) KF-PLL at 350Hz
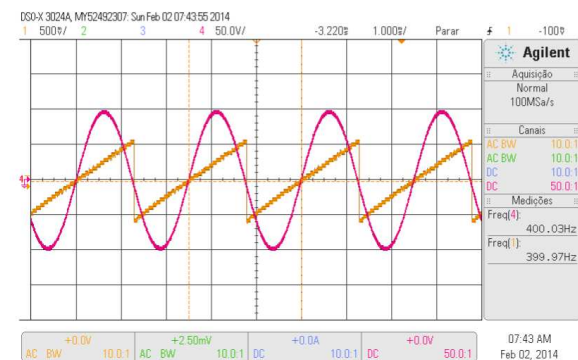
h) KF-PLL at 400Hz

Figure 5-17: KF-PLL Tracking

113

5.2.4.2 AMI and SCM

The operation of the 27 level Asymmetrical Multilevel Inverter (AMI) was tested to verify that the hardware Asymmetrical Multilevel Inverter (AMI) and software Staircase Modulation (SCM) setu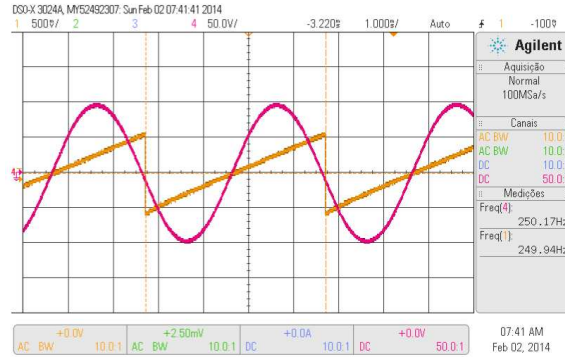ps are working properly. Figure 5-18 shows the response of the AMI to the SCM in $60Hz$ Figure 5-18 (a), $250Hz$ - Figure 5-18 (b), $500Hz$ - Figure 5-18 (c), and $750Hz$ - Figure 5-18 (d).

a) AMI at 60Hz

b) AMI at 250Hz

c) AMI at 500Hz

d) AMI at 750Hz
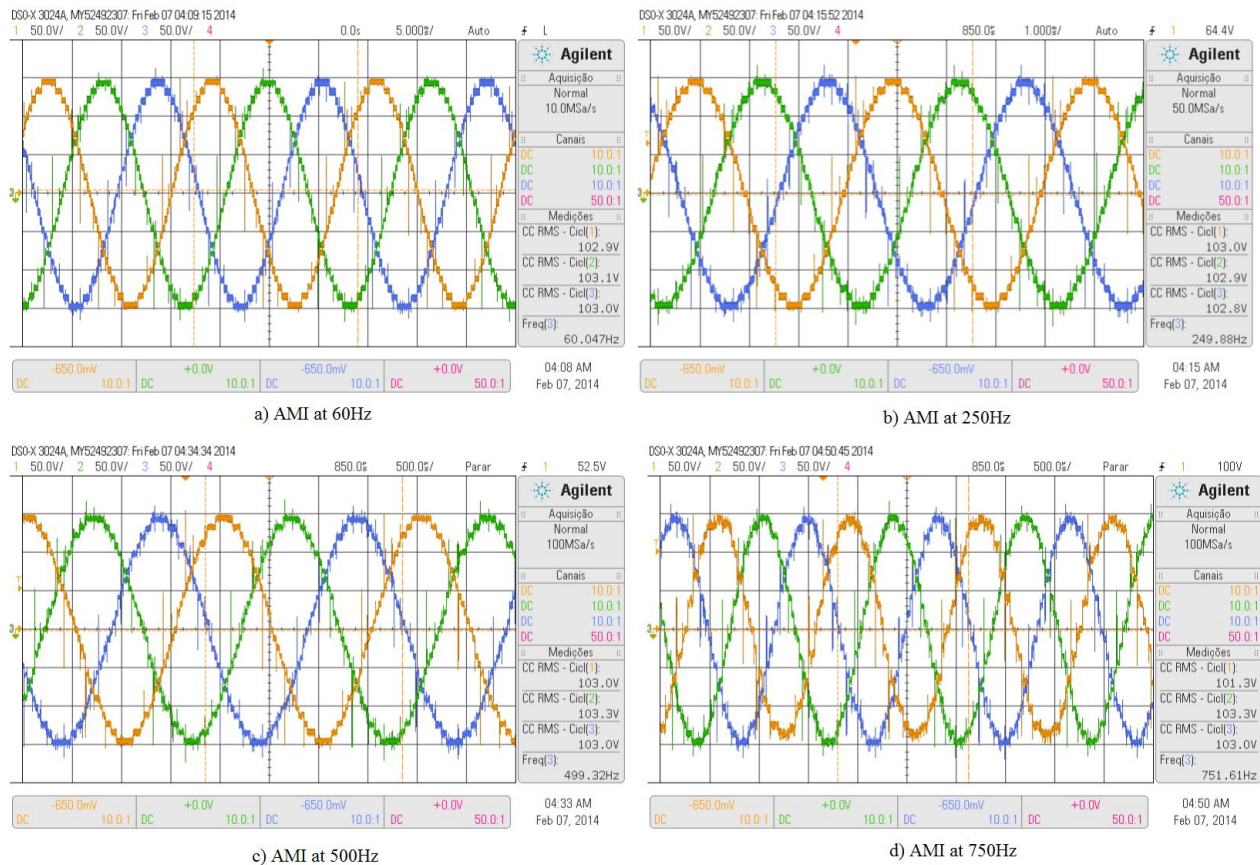
Figure 5-18: Three-phase AMI Waveforms

Note that the AMI is synthetizing approximately a sinusoidal voltage waveform using $(Ea_1; Ea_2; Ea_3) = (11.11; 33.33; 100)V$ as voltage levels. When the AMI achieves $750\ Hz$, the quality of the synthetized waveform decreases, this is due to the IGBTs low switching frequency.

5.2.4.3 Aeronautical Active Power Filter

In the beginning of the testing phase, the AAPF was tested in low frequency. Figure 5-19 shows the moment when the AAPF is connected to the PCC. The orange waveform represents the active filter current.
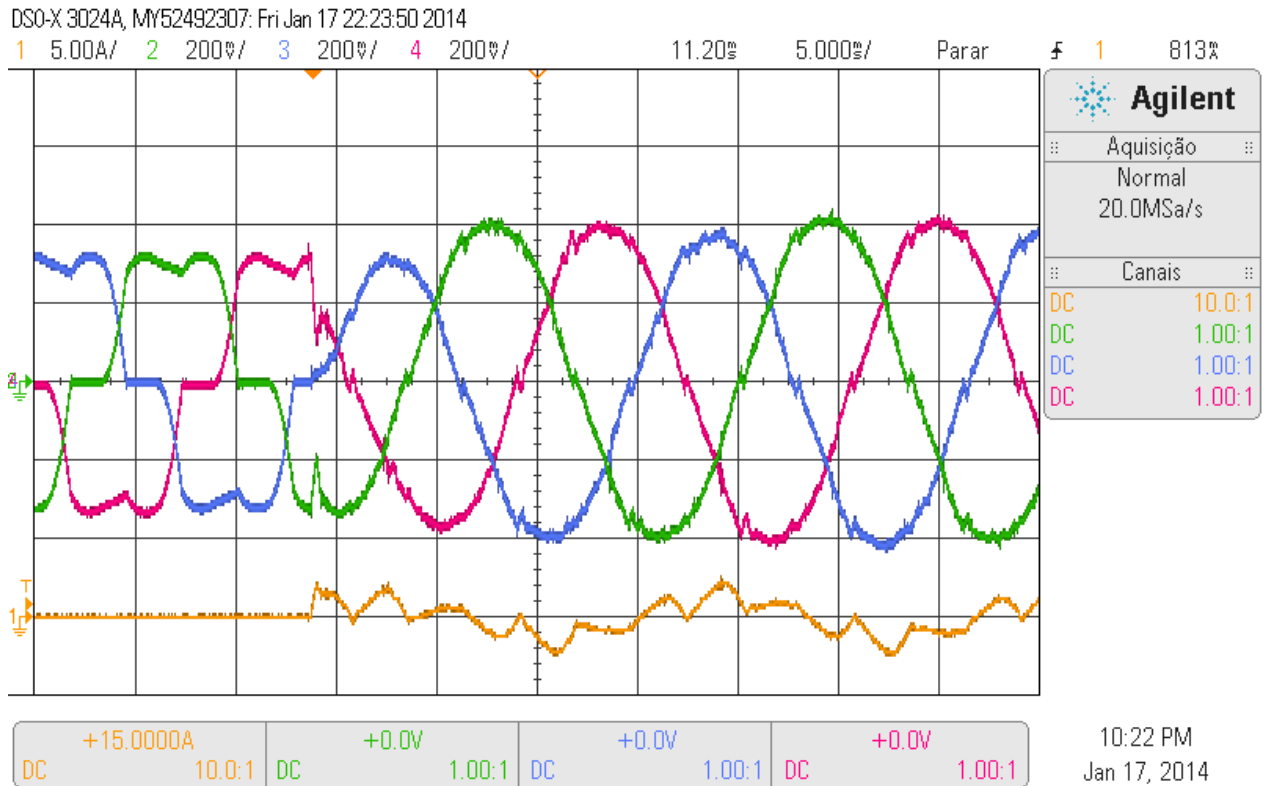
Figure 5-19: Three-phase source currents and inverter current (60Hz)

As shown in Figure 5-19, the AAPF was able to filter the nonlinear currents with comprehensive quality. Note that due to some gain mistake, the AAPF did not compensate the integrity of the non-active currents, as a consequence, some fundamental current remains.

Unfortunately, after this test, the power source was damaged by a reverse overcurrent. This current was caused by an attempt to optimize the code for reducing the execution time. The overcurrent damaged the phase b of the power source, excluding the possibility of further three-phase tests.

5.2.5 Single-Phase compensation with Three-Phase Control

5.2.5.1 Low Frequency Case study (60 Hz)

One phase of the power source was damaged, further testing could only be done in single phase, yet, the control remained in three-phase. At this point, the voltage references of the KF-PLL are obtained thought phases a and c.

In this manner, the three-phase load was overwritten by a single-phase load and the below tests were done. Figure 5-20 and Figure 5-21 shows the PCC voltage (v), source current (i_S), load current (i_L) and instantaneous active power (p) before and after active filtering.

Figure 5-20: System waveforms (Voltage and Currents) before Active Filtering (60Hz)
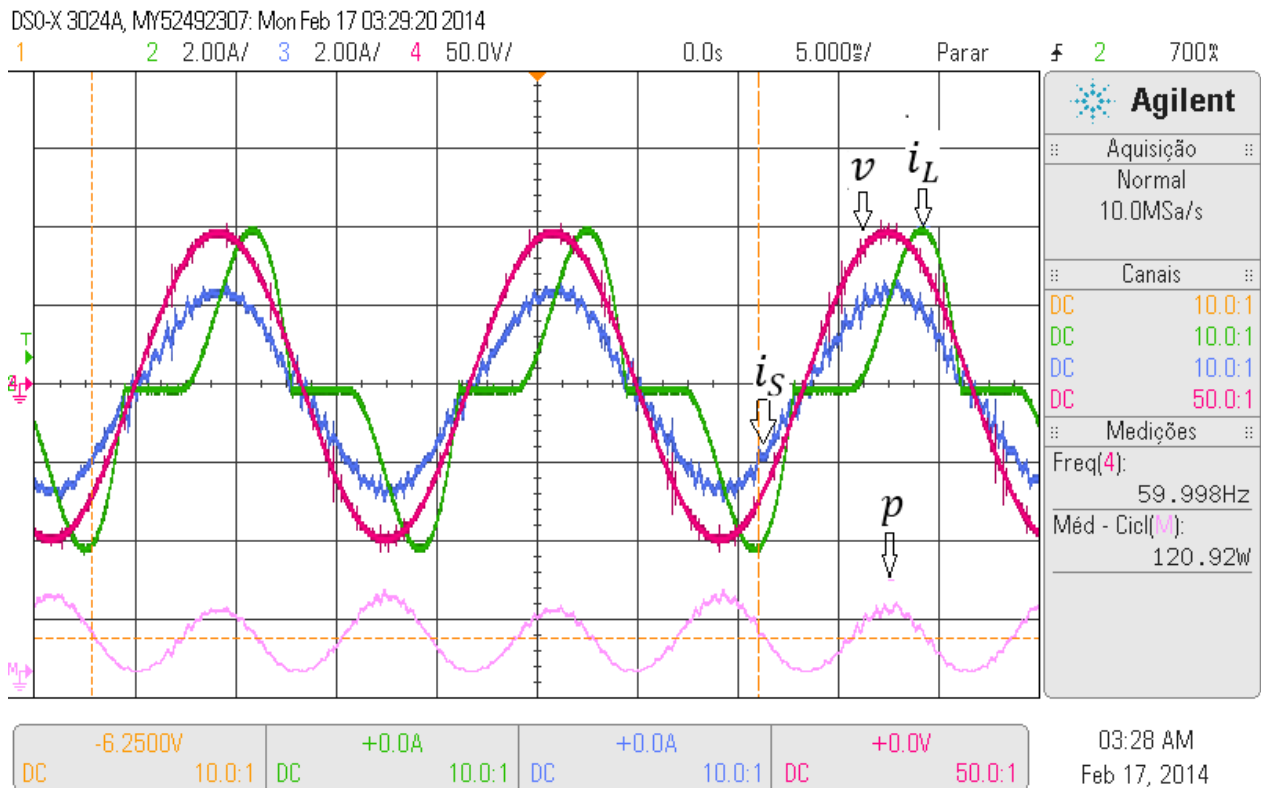
Figure 5-21: System waveforms (Voltage and Currents) after Active Filtering (60Hz)

Inspecting the above figures, the active filter injects high current ripple, this is due to the low switching frequency achieved. Figure 5-22 shows the inverter voltage (v_{inv}) and inverter current (i_{inv}). Note that the active power is practically the same before and after active filtering. This proves that the CPT is working properly.
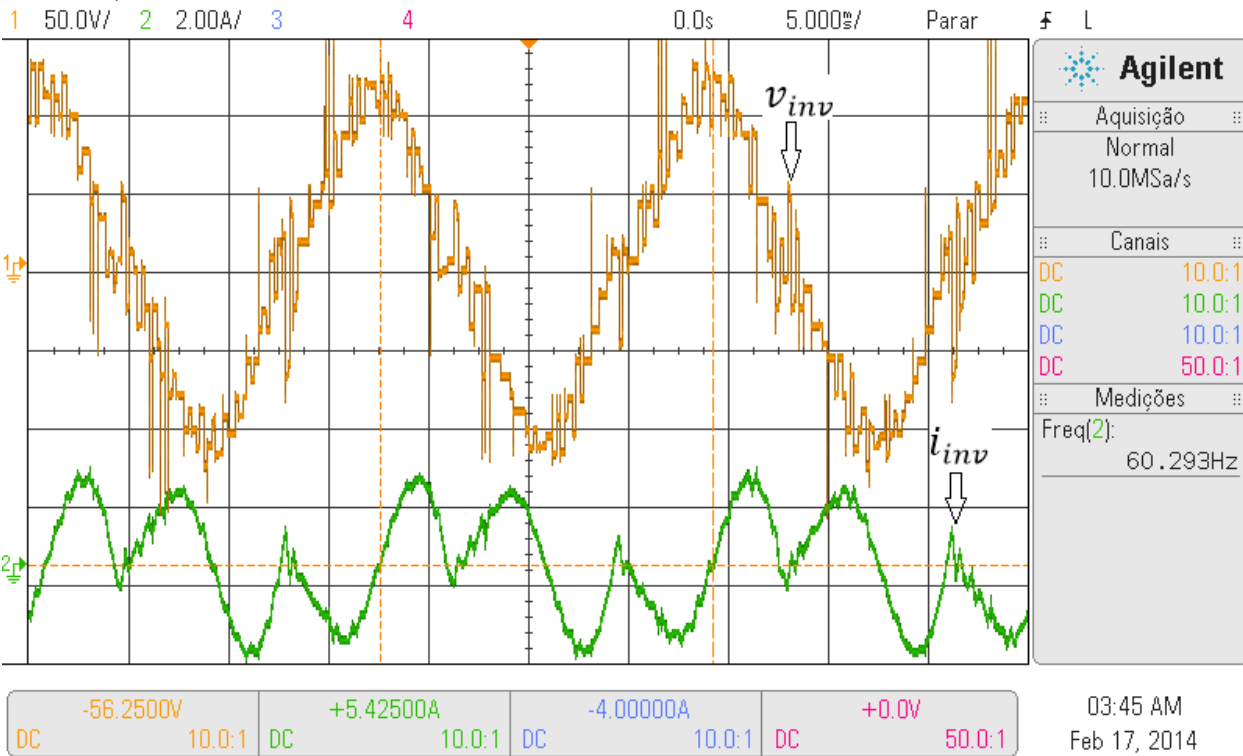
Figure 5-22: Inverter Voltage and Current (60Hz)

Figure 5-23 and Figure 5-24 shows the current spectrum (pink) before and after active filtering.
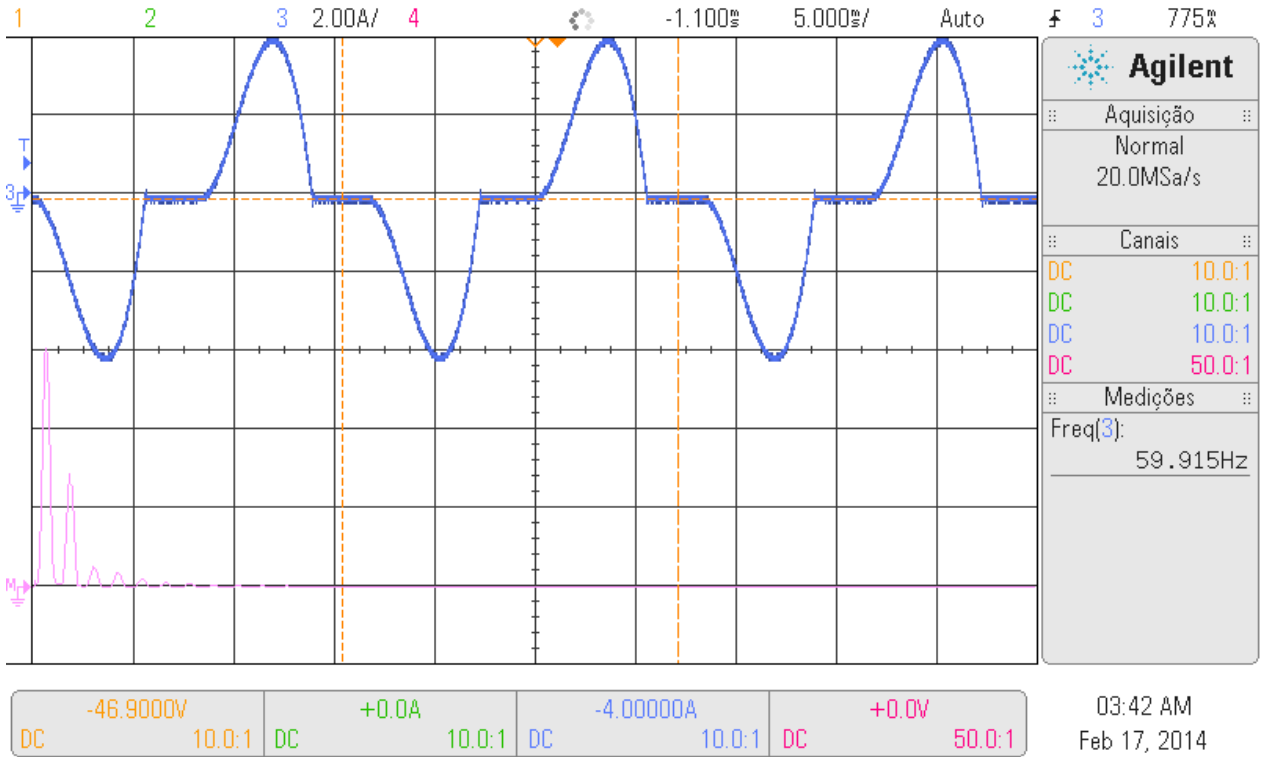
Figure 5-23: Non-Linear Current Spectrum (60Hz)
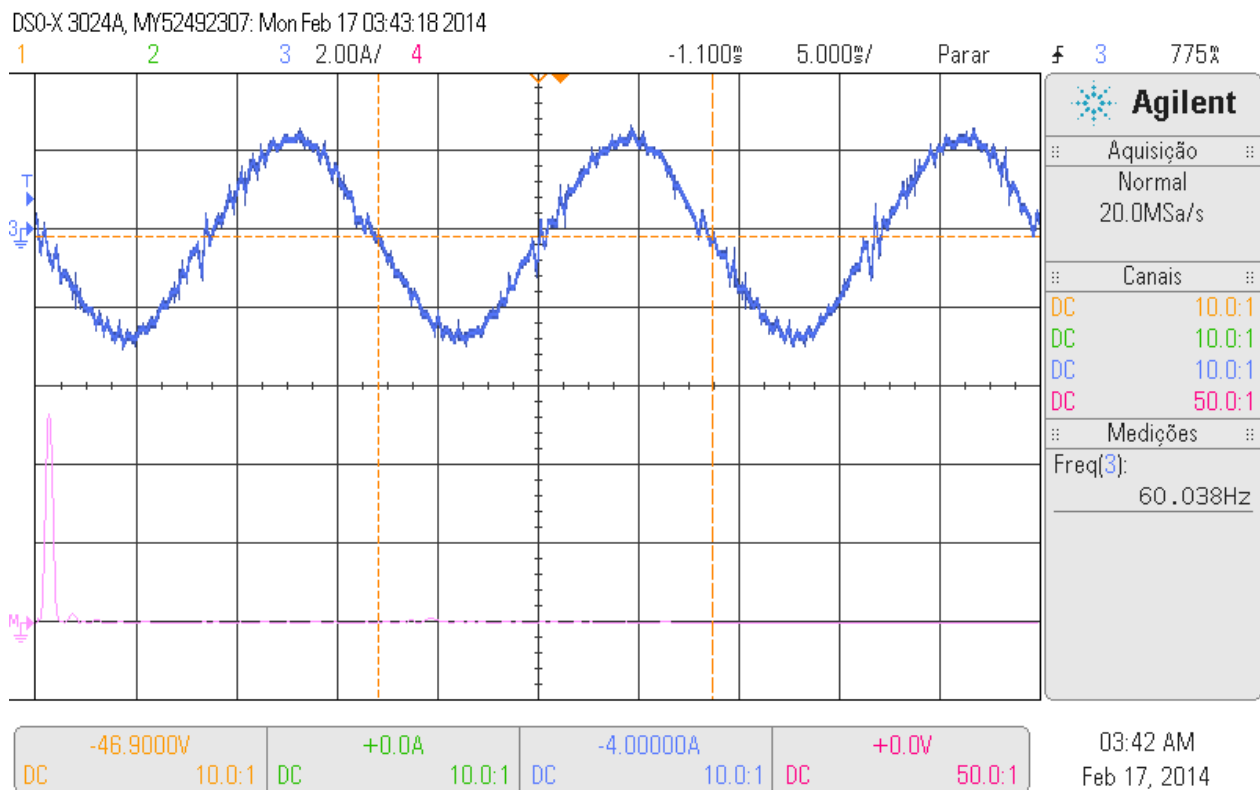
Figure 5-24: Filtered Current Spectrum (60Hz)

Despite some low components in the spectrum, it is observed that the AAPF is able to compensate most of the non-active currents, however the filtering quality is weak.

5.2.5.2 Low Frequency Case study (100 Hz)

In order to verify the AAPF performances in higher frequencies, the frequency was increased from 60 Hz to 100 Hz. Figure 5-25 shows the PCC voltage (v), source current (i_S), load current (i_L) and instantaneous active power (p) after active filtering.
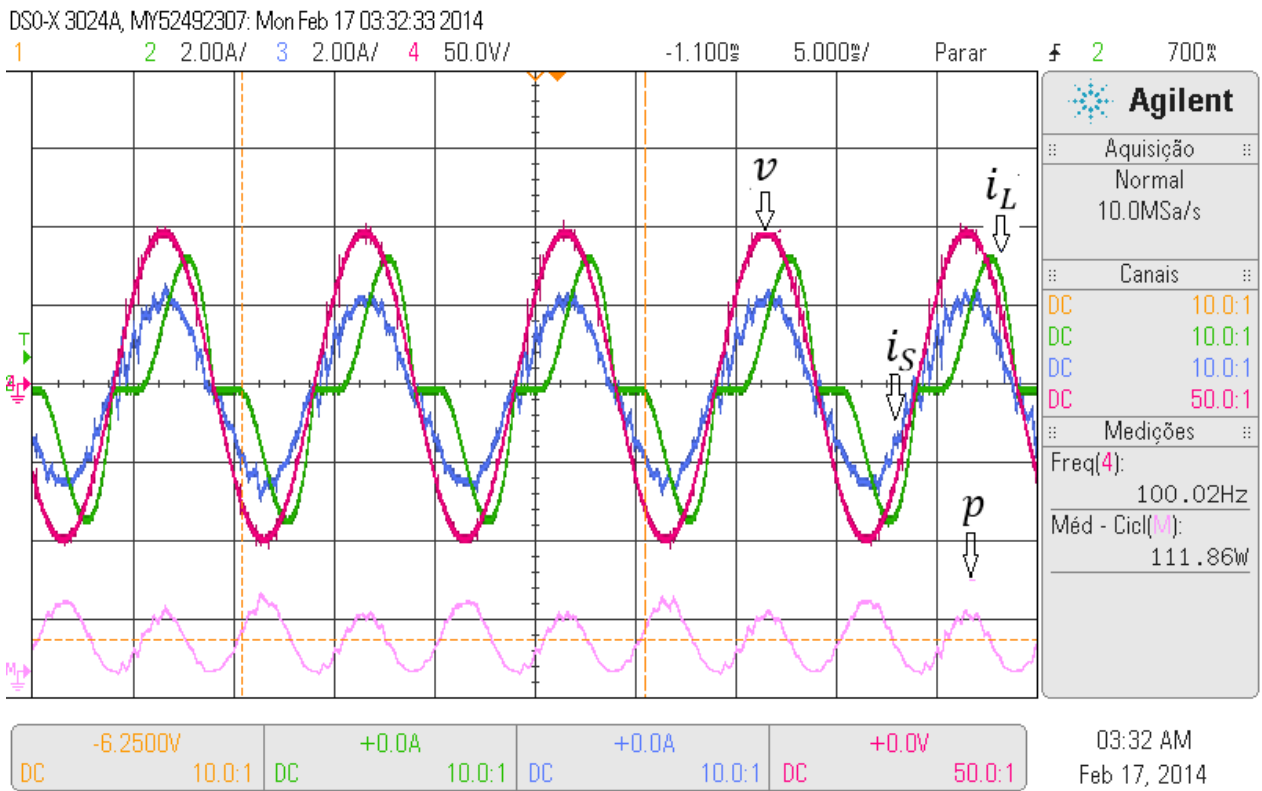
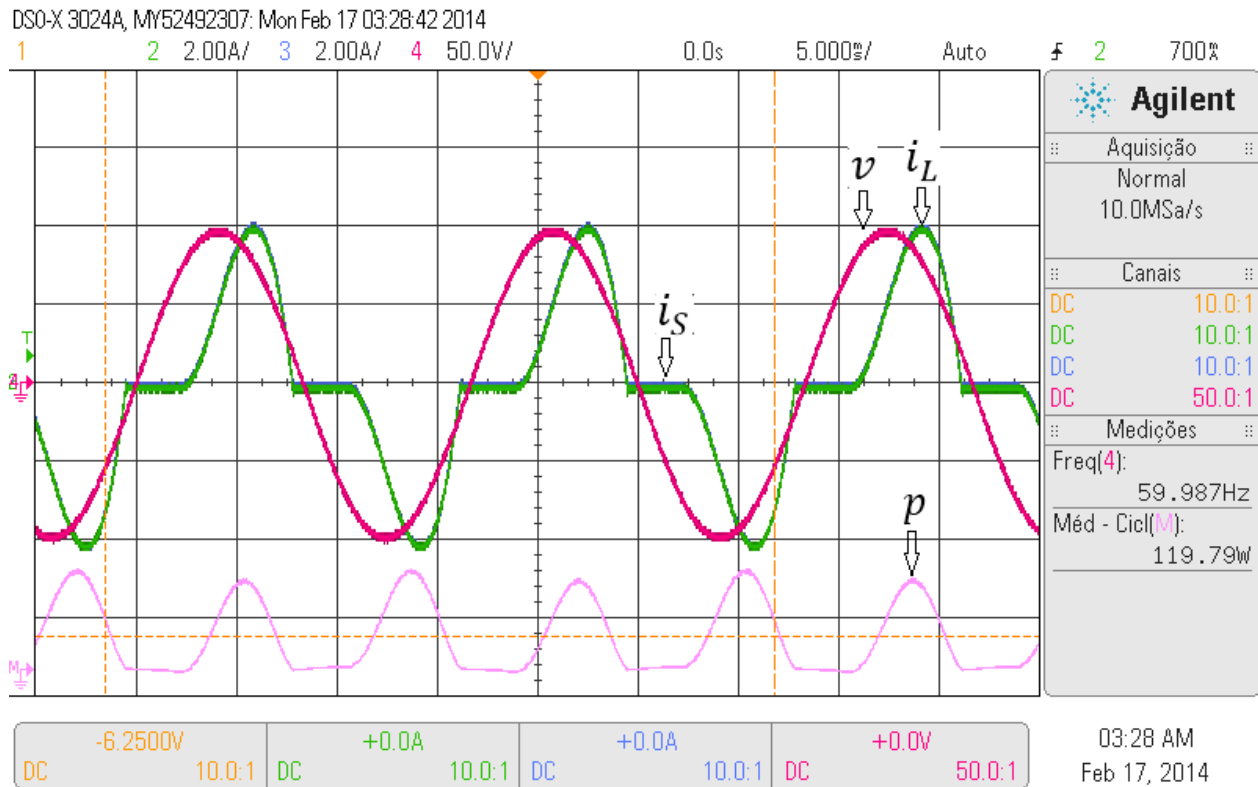Figure 5-25: System waveforms (Voltage and Currents) after Active Filtering (100Hz)

Figure 5-26 and Figure 5-27 show the current spectrum (pink) before and after active filtering.
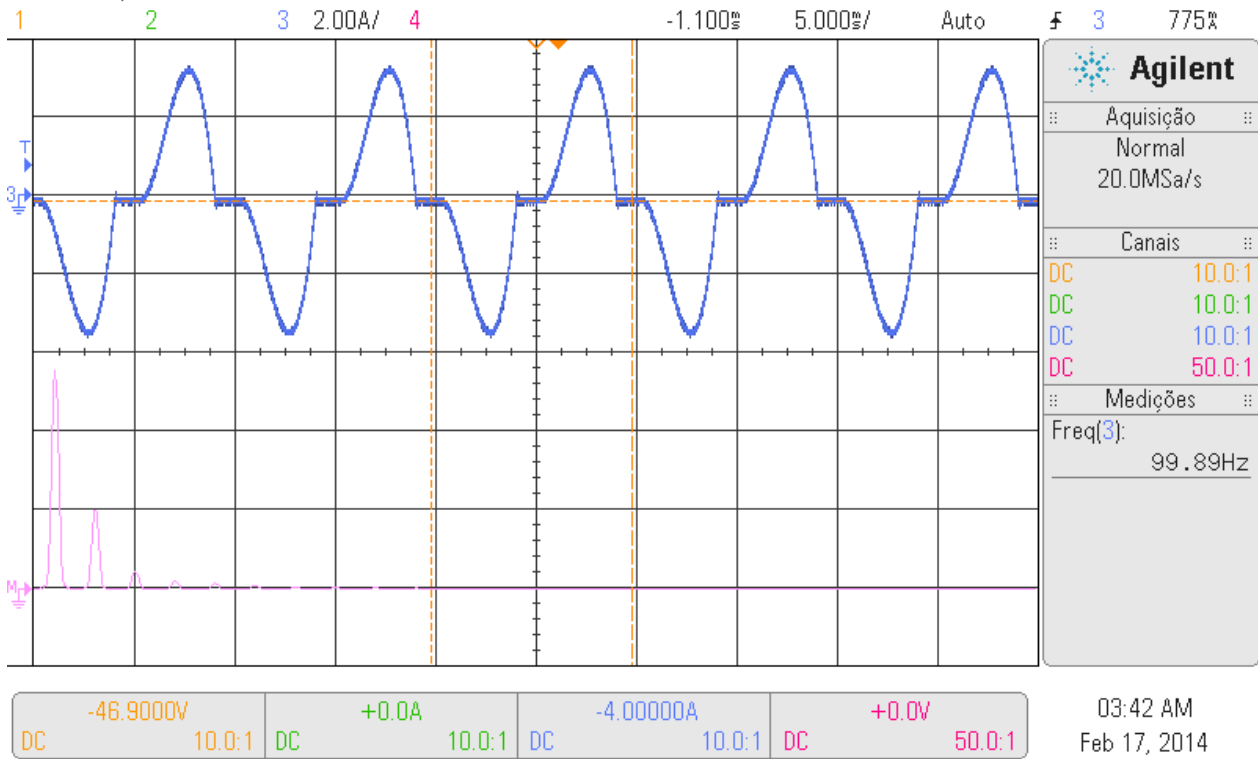
Figure 5-26: Non-Linear Current Spectrum (100Hz)
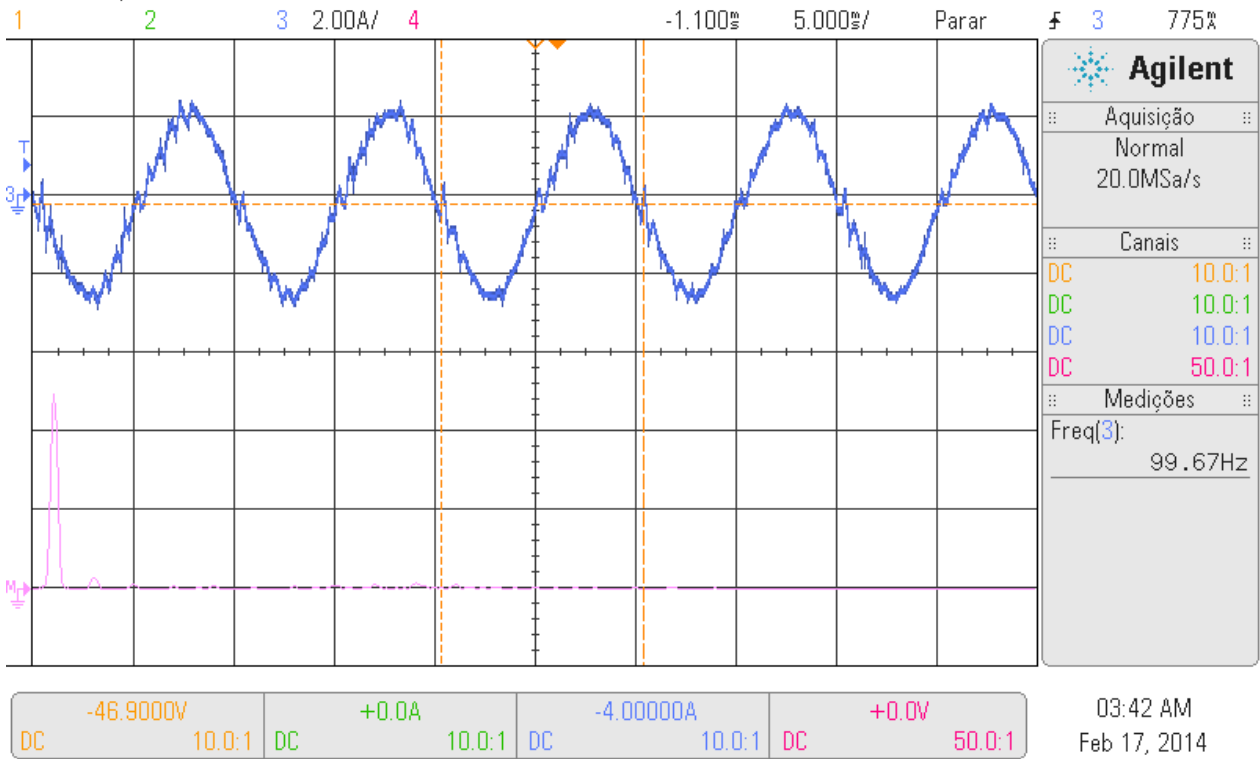
Figure 5-27: Filtered Current Spectrum (100Hz)

As verified, it is observed that the AAPF was able to compensate most of the non-active currents, however the filtering quality is weaker the higher is the fundamental frequency.

6 CONCLUSION

The more electric aircraft trend has led to the increasing use of power electronics devices on board of modern aircrafts; thus the use of shunt active power filters becomes attractive for on-board power conditioning. This work proposes and describes the design, simulation and implementation of an Aeronautical Active Power Filter for aircraft Variable Speed Variable Frequency power networks.

Regarding the complexity and high fundamental frequency of the aircraft electrical system, the active filter is required to be robust and able of compensating harmonics at very high frequencies. Consequently the project has been optimized with a 27 level asymmetrical multilevel voltage source converter employing the conservative power theory. The control system uses a Kalman Filter Phase-Looked Loop to synchronize to the grid and the staircase modulation technique is applied in order to obtain 27 voltage levels in the inverter's output.

The modeling techniques of the Aeronautical Active Power Filter (AAPF) in abc and $dq0$ coordinates have been applied. Based on the proposed models, the feedback control scheme is analyzed and designed to perform reactive power compensations. The proposed controller is designed according to the simplified models. The compensator design based on small-signal transfer function gives the system the desired control bandwidth, and stability margin.

After analyzing accurate simulation results and partial prototype testing results, it can be concluded that the proposed active filter control has proved to be effective for mitigating current harmonics on aircraft power grids. The simulation results show the performance of the designed controller, achieving good dynamics in the required frequency range (300 Hz to 800 Hz).

Considering the environment of the fundamental frequency varying, present in modern aircraft power network, the proposed strategy gives very good results without any need for additional controller parameters adjusting.

A single-phase prototype was developed and experimented in order to verify the feasibility of the proposition. The CPT calculates accurately the non-active currents, while the staircase modulator enables the generation of various voltage levels in the AAPF output. The filtering quality was low, as a consequence of the use of PI controllers which were not placed in a rotating reference frame.

A three-phase prototype was developed to test the three-phase algorithm. The algorithm was processor intensive, resulting in high execution time, which limited the performance of the AAPF. Regardless of this issue, the Kalman Filter Phase-Locked Loop (KF-PLL) was stable and the filter succeeded in mitigating most of the non-active currents.

The three-phase prototype has the potential to active filter in 400 Hz frequencies and higher, yet, proper prototype modifications must be done as sown in section 6.1.

6.1 FUTURE WORK

Some recommendations for future work are proposed below.

- The microcontroller F28335 must be overwritten by FPGAs in order to decrease the algorithm execution time and consequently enable higher switching frequencies.
- The 9 single phase IGBT inverters must be overwritten by high frequency MOSFET inverters in order to enable active filtering in higher fundamental frequencies.
- The prototype must be tested against the recommendations of the MIL-HDBK-704 (Guidance for Test Procedures for Demonstration of Utilization Equipment Compliance to Aircraft Electrical Power Characteristics) and RTCA DO-160F (Environmental Conditions and Test Procedures for Airborne Equipment).
- Development of the DC bus voltage control strategy of the asymmetrical multilevel inverter AMI.

7 REFERENCES

[1] "http://www.eurtd.com/moet/," [Online].

[2] K. W. E. Cheng, "Comparative study of AC/DC converters for more electric aircraft," *Power Electronics and Variable Speed Drives Conference in Proc. Inst. Elect. Eng.,* p. 299–304, 1998.

[3] A. Eid, M. Abdel-Salam, H. El-Kishky and T. El-Mohandes, "Simulation and transient analysis of conventional and advanced aircraft electric power systems with harmonic mitigation," *Elect. Power Syst. Res.,* vol. 79, no. 4, p. 660–668, Apr. 2009.

[4] J. A. Rosero, J. A. Ortega, E. Aldabas and L. Romeral, "Moving towards a more electric aircraft," *IEEE Aerosp. Electron. Syst. Mag.,* vol. 22, no. 3, p. 3–9, Mar. 2007.

[5] M. Taha, " Active rectifier using DQ vector control for aircraft power system," *IEMDC,* pp. 1306-1310, 2007.

[6] X. Liu, A. Forsyth, H. Piquet, S. Girinon, X. Roboam, N. Roux, A. Griffo, J. Wang, S. Bozhko, P. Wheeler, M. Margail, J. Mavier and L. Prisse, "Power Quality and Stability Issues in More-Electric Aircraft Electrical Power Systems," *More Electric Aircraft Forum,* 2009.

[7] P. Tenti, H. Paredes and P. Mattavelli, "Conservative Power Theory, a Framework to Approach Control and Accountability Issues in Smart Microgrids," *IEEE Transactions on Power Electronics,* vol. 26, no. 3, pp. 664 - 673, March 2011.

[8] D. K. Michaels, "MORE ELECTRIC AIRCRAFT Implications for Suppliers," in *SpeedNews 13th Annual Aviation Industry*, Suppliers Conference in Toulouse, September 19, 2012.

[9] T. Jomier, "Moet public technical report," *Aeronautics and Space,* 2009.

[10] A. I. o. A. a. Astronautics, "Beyond the more electric Aircraft," *Journal of Aerospace Computing, Information, and Communication,* 2005.

[11] X. Roboam, B. Sareni and A. d. Andrade, "Toward Optimized Electrical Networks Embedded in More-Electrical Aircraft," *IEEE industrial electronics magazine,* vol. 12, pp. 1932-4529, december 2012.

[12] "L'avion plus électrique," *Revue 3E.I,* vol. 63, Mar. 2011.

[13] M. Sinnett., " 787 no-bleed systems: Saving fuel and enhancing operational efficiencies.," *Boeing Aero Mag.,* p. 28, 2007.

[14] R. D. Maglie, G. Osvald, J. Engstler, A. Engler and J.-P. Carayon, "Optimized 70 kW power inverter dedicated to future aircraft application," *in Proc. EPE Conf., Barcelona, Spain,* p. 1– 10, 2009.

[15] X. Feng, J. Liu and F. C. Lee, "Impedance specifications for stable DC distributed power systems," *IEEE Trans. Power Electronics,* vol. 17, no. 2, p. 157–162, Mar. 2002.

[16] H. N. Huu, L. Gerbaud, N. Retiere and J. R. F. Wurtz, "Analytical modeling of static converters for optimal sizing of on-board electrical systems," *VPPC Conference in Proceedings IEEE; Lille, France,* pp. 1 - 6, 2010.

[17] H. Nguyen-Huu, N. Retière, F. Wurtz, X. Roboam, B. Sareni and D. Alejo, "Optimal sizing of an embedded electrical system with an approach for restricting the search space," *COMPEL-Int. J. Comput. Math. Electr. Electron. Eng.,* vol. 28, no. 5, p. 1141–1154.

[18] T. L. M. Pillay, "Physical basis for the variation of lamination core loss coefficients as a function of frequency and flux density," *in Proc. IEEE 32nd Annu. Conf. Industrial Electronics , IECON,,* p. 1381–1387, 2006.

[19] A. Abdel-Hafez, "Power Generation and Distribution System for a More Electric Aircraft - A Review," *Recent Advances in Aircraft Technology, InTech,* 2012.

[20] A. AbdElHafez and Forsyth, "A Review of More-Electric Aircraft," *Proceedings of The 13rd international conference on Aerospace Science and Aviation Technology conference ,ASAT-13. Cairo, Egypt,,* pp. 26-28,, May 2009.

[21] M. Cross, A. Forsyth and G. Mason, "Modelling and simulation strategies for the electric system of large passenger aircraft," *in SAE 2002 conference,* pp. 450-459, 2002.

[22] "MIL-STD 704 Revision F – Aircraft Electric Power Characteristics".

[23] W. Said, Writer, *Aircraft Electric Power System. A Power Conversion Perspective..* [Performance]. Hamilton Sundstrand, September 29th 2011.

[24] C. Raimondi, T. Sawata, M. Holme, A. Barton, G. White, J. Coles, P. Mellor and N. Sidell, "Aircraft embedded generation systems," *in Proceeding of International Conference on Power Electronics, Machines and Drives, PEMD,* pp. 217-222, April 2002.

[25] R.-R. Plc, "More Electric Engines for More Electric Aircraft," IET – The Institution of engineering and Technology.

[26] A. AbdEl-hafez, A. Cross, A. Forsyth, D. Trainer and J. Cullen, "Single-Phase Active Rectifier Selection for Fault Tolerant Machine, in 3rd IET International Conference on Power Electronics, Machines and Drives," *PEMD,* pp. 435-439, April 2006.

[27] "IEEE STD 519 - Recommended Practices and Requirements for Harmonic Control in Electrical Power Systems," 1992.

[28] "RTCA/DO-160 Environmental Conditions and Test Procedures for Airborne Equipment," RTCA, Incorporated., 2010.

[29] Z. Chen, Y. Luo, M. Chen, L. Shi and J. Li, "Design and Implementation of a High Performance Aeronautical Active Power Filter," *IECON 2010 - 36th Annual Conference on IEEE Industrial Electronics Society,* pp. 2032 - 2037, Nov. 2010.

[30] Y. Luo, Z. Chen, M. Chen and J. Li, "A Cascaded Shunt Active Power Filter with High Performance for Aircraft Electric Power System," *Energy Conversion Congress and Exposition (ECCE),* pp. 1143 - 1149, 2011 IEEE.

[31] Z. Chen, Y. Luo and Miao Chen, "Control and Performance of a Cascaded Shunt Active Power Filter for Aircraft Electric Power System," *IEEE TRANSACTIONS ON INDUSTRIAL ELECTRONICS,* vol. 59, no. 9, pp. 3614 - 3623, SEPTEMBER 2012.

[32] Z. Chen, C. Wang, M. Chen and Jianxia Li, "A Research on Cascade Five-level Aeronautical Active Power Filter," *IEEE 7th International Power Electronics and Motion Control Conference ECCE Asia, Harbin, China,* pp. 2732 - 2737, June 2-5, 2012.

[33] H. Hu, W. Shi, J. Xue, Y. Lu and Yan Xing, "A Multi-resolution Control Strategy for DSP Controlled 400Hz Shunt Active Power Filter in an Aircraft Power System," *Applied Power Electronics Conference and Exposition (APEC),* 2010.

[34] H. Hu, W. Shi, Y. Lu and Yan Xing, "Design Considerations for DSP-Controlled 400 Hz Shunt Active Power Filter in an Aircraft Power System," *IEEE TRANSACTIONS ON INDUSTRIAL ELECTRONICS,* vol. 59, no. 9, pp. 3624 - 3634, SEPTEMBER 2012.

[35] M. Odavic, P. Zanchetta and Mark Sumner, "A Low Switching Frequency High Bandwidth Current Control for Active Shunt Power Filter in Aircrafts Power Networks," *The 33rd Annual Conference of the IEEE Industrial Electronics Society (IECON),* pp. 1863 - 1868, 5-8 Nov. 2007.

[36] V. Biagini, M. Odavic, P. Zanchetta, M. Degano and P. Bolognesi, "Improved Dead Beat Control of a Shunt Active Filter for Aircraft Power Systems," *IEEE International Symposium on Industrial Electronics (ISIE),* pp. 2702 - 2707, 2010.

[37] V. Biagini, P. Zanchetta, M. Odavic, M. Sumner and Marco Degano, "Control and Modulation of a Multilevel Active Filtering Solution for Variable-Speed Constant-Frequency

More-Electric Aircraft Grids," *IEEE TRANSACTIONS ON INDUSTRIAL INFORMATICS,* pp. 600 - 608, May 2013.

[38] J. Liu, P. Zanchetta, M. Degano and Elisabetta Lavopa, "Control Design and Implementation for High Performance Shunt Active Filters in Aircraft Power Grids," *IEEE TRANSACTIONS ON INDUSTRIAL ELECTRONICS,* vol. 59, no. 9, pp. 3604 - 3613, SEPTEMBER 2012.

[39] J. F. Guerreiro, J. A. Pomilio and T. D. C. Busarello, "Design of a multilevel Active Power Filter for More Electrical Airplane variable frequency systems," *IEEE Aerospace Conference,* pp. 1 - 12, 2013.

[40] A. Eid, H. El-Kishky, M. Abdel-Salam and M. T. El-Mohandes, "On power quality of variable-speed constant-frequency aircraft electric power systems,," *IEEE Trans. Power Del.,* vol. 25, no. 1, p. 55–65, Jan. 2010..

[41] R. P. VENTURINI, P. MATTAVELLI, P. ZANCHETTA and M. SUMNER, "Adaptive Selective Compensation for Variable Frequency Active Power Filters in More Electrical Aircraft,," *IEEE TRANSACTIONS ON AEROSPACE AND ELECTRONIC SYSTEMS,* vol. 48, no. 2, pp. 1319 - 1328, APRIL 2012.

[42] R. Cardoso and H. A. Gründling, "Grid Synchronization and Voltage Analysis Based on the Kalman Filter," *I-Tech, Vienna, Austria.,* p. 584, April 2009.

[43] S. K. Chung, "A phase tracking system for three phase utility interface inverters," *IEEE Transactions on Power Electronics,* pp. 431 - 438, May 2000.

[44] V. Kaura and V. Blasko, "Operation of a phase locked loop system under distorted utility conditions," *IEEE Transactions on Industry Applications,* vol. 33, no. 1, pp. 58-63, January/February 1997.

[45] M. S. Padua, S. M. Deckmann, G. S. Sperandio, F. Marafao and D. Colon., "Comparative analysis of Synchronization Algorithms based on PLL, RDFT and Kalman Filter," *IEEE International Symposium on Industrial Electronics,* pp. 964 - 970, 4-7 June 2007.

[46] A. Gelb, J. F. K. JR, R. A. N. JR., C. F. Price and A. A. S. JR., "Applied Optimal Estimation," *M.I.T. Press, Cambridge,* vol. 64, no. 4, pp. 574- 575, 1976.

[47] R. G. Brown, "Introduction to Random Signals and Applied Kalman Filtering," *John Wiley & Sons, New York,* January 1, 1992.

[48] F. Huerta, D. Pizarro, S. Cobreces, F. J. Rodriguez, C. Girón and A. Rodriguez., "LQG Servo Controller for the Current Control of LCL Grid-Connected Voltage-Source Converters," *IEEE Transactions on Industrial Electronics,* vol. 59, no. 11, pp. 4272 - 4284, Nov. 2012.

[49] G. Gong, U. Drofenik and J. Kolar, "12-Pulse Rectifier for More Electric Aircraft Applications," *IEEE International Conference on Industrial Technology,* vol. 2, pp. 1096 - 1101, 2003.

[50] F. P. Marafão, S. M. Deckmann, J. A. Pomilio and R. Q. Machado, "Selective Disturbing Compensation and Comparisons of Active Filtering Strategies," *IEEE International Conference on Harmonics and Quality of Power,* vol. 2, pp. 484-489, 2002.

[51] E. H. Watanabe, H. Akagi and M. Aredes, "Instantaneous p-q Power Theory for Compensating Nonsinusoidal Systems," *Przegląd Elektrotechniczny, (Electrical Review),* vol. 84, no. 6, pp. 28-37, 2008.

[52] H. K. M. Paredes, D. I. Brandão, T. M. Terrazas and F. P. Marafão, "SHUNT ACTIVE COMPENSATION BASED ON THE CONSERVATIVE POWER THEORY CURRENT'S DECOMPOSITION," *Brazilian Power Electronics Conference (COBEP),* pp. 788 - 794, 11-15 Sept. 2011.

[53] H. K. M. Paredes, ""Conservative Power Theory: A new Approach to Cooperative Control of Power Conditioners and Considerations Regarding to Responsibility Assignment," *PhD Thesis, UNICAMP, 2011..*

[54] M. Manjrekar and G. Venkataramanan, "Advanced topologies and modulation strategies for multilevel inverters," *Power Electronics Specialists Conference,* 1996.

[55] S. Sirisukprasert, A. Huang and J.-S. Lai, "Modeling, analysis and control of cascaded-multilevel converter-based STATCOM," *Power Engineering Society General Meeting,* pp. Power Engineering Society General Meeting, 2003, IEEE , 13-17 July 2003.

[56] C. Han, Z. Yang, A. Huang and M. Ingram, "Modelling and control of a cascade-multilevel converter-based STATCOM for electric arc furnace flicker mitigation," *Industrial Electronics Society, 2005. IECON 2005. 31st Annual Conference of IEEE,* 6-6 Nov. 2005.

[57] S. Vazquez, J. Leon, J. Carrasco, L. Franquelo, E. Galvan, J. Sanchez and E. Dominguez, "Controller design for a single-phase two-cell multilevel cascade H-bridge converter,," *IEEE International Symposium on Industrial Electronics, ISIE,* pp. 82342-2347, June 30 2008-July 2 200.

[58] G. Escobar, A. Valdez, M. Martinez-Montejano and V. Rodriguez-Zermeno, ""A Model-Based Controller for the Cascade Multilevel Converter Used as a Shunt Active Filter," *Annual Meeting. Conference Record of the Industry Applications Conference, IAS,* vol. 42, pp. 1837-1843, 23-27 Sept. 2007.

APPENDIX

APPENDIX A – KALMAN FILTER CODE

This Appendix shows the code developed in Matlab/Simulink to implement the Kalman Filter based Phase-Locked Loop.

```matlab
function Xout  = KalmanFilter(meas, wk , Kw, Ku)

% Initialization
persistent P;
persistent X;
persistent K;
if isempty(P)
    X = zeros ([2, 1]);
    P = eye(2);
    init=1;
    A=zeros ([2, 2]); %State transition matrix
else
    init=0;
    A = [cos(wk) sin(wk);-sin(wk) cos(wk)];
end

Q= [Kw 0; 0 Kw]; %Process noise covariance
R= [Ku 0; 0 Ku]; % Measurement noise covariance
M= [1 0; 0 1]; %Measurement matrix

%compute initial P
P = (A*P*A') + Q;
%compute gain
K = M*P'*inv((M*P') *M+ R);
K=K';
%update P (covariance matrix) for next step
P = P-K*M*P;
%for initialization
if init==0
%residual error estimation
residual = meas - X;
%update the values
X = X + K*residual;
Xout=M*X;
else
Xout=[0;0];
X=[0;0];
end
X = A*X;
```

APPENDIX B- PROTOTYPE PICTURES

Figure 0-1 shows the California Instruments power source.

Figure 0-1: California Instruments variable frequency power source

Figure 0-2 shows the 9 semix4 Semikron modules, the inverters are connected accordingly to Figure 3-18.
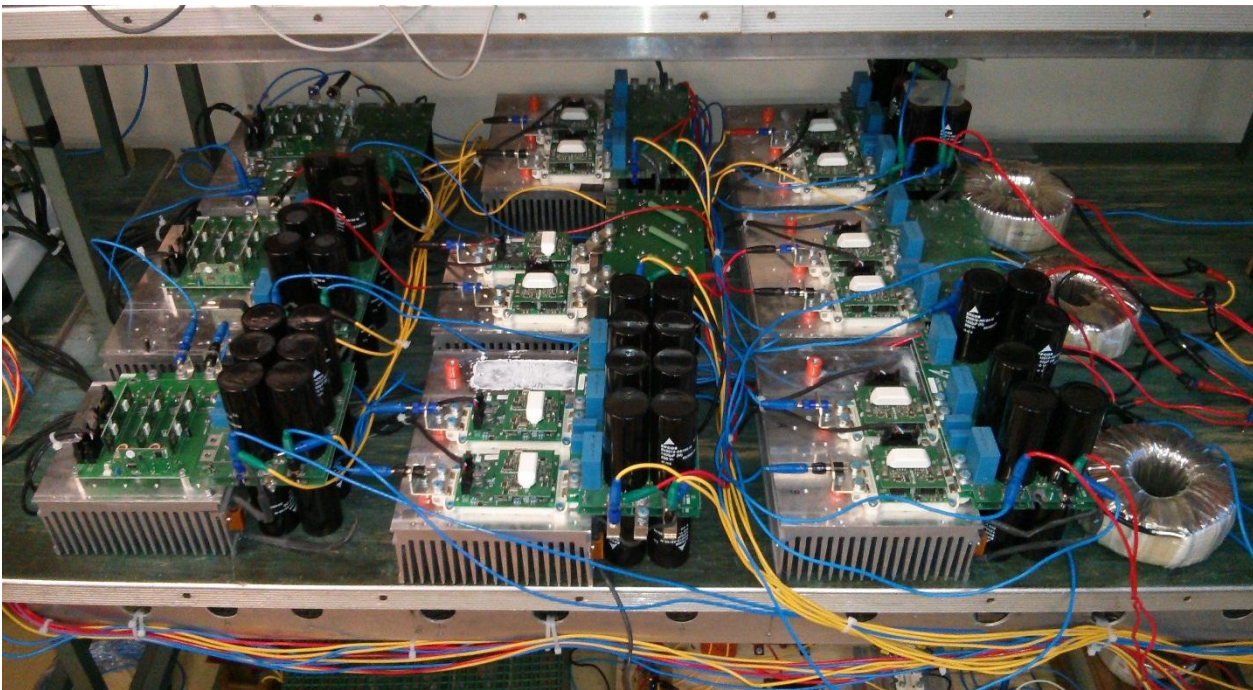

Figure 0-2: Asymmetrical Multilevel Inverter

Figure 0-3 shows the 9 voltage sources which are connected to the DC links of the single-phase cells.

Figure 0-3: DC Power Sources

Figure 0-4 shows the 9 power resistors, inconveniently, these resistors were needed to burn regenerative energy of the DC links since this voltage is not controlled.
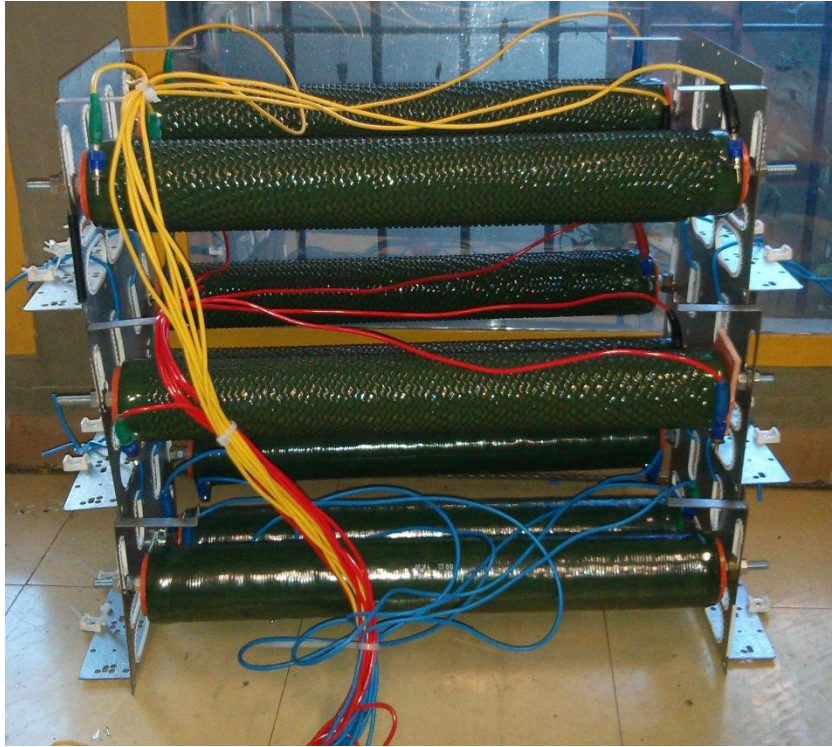
Figure 0-4: Power Resistors connected to the DC links of the AMI

Figure 0-5 shows the three-phase non-linear load. This load is not equivalent to the load used in the case study of section 4 because the three-phase transformer of Figure 3-4 was not available.
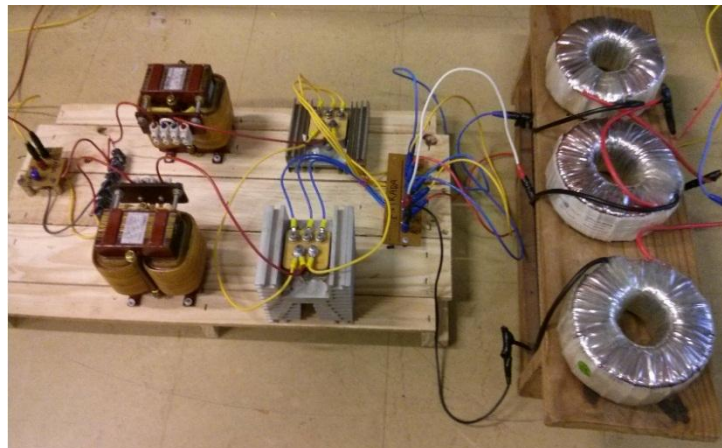

Figure 0-5: Nonlinear Load

Figure 0-6 shows the Texas Instruments DSP. 9 ADCs are used as well as 36 GPIOs for commanding the inverters. The same picture shows the 9 DSP Gate Driver interface boards. These

boards were needed because the Semikron skyper gate drives work with input signals of 15V and the DSP GPIO voltage is 3.3V.
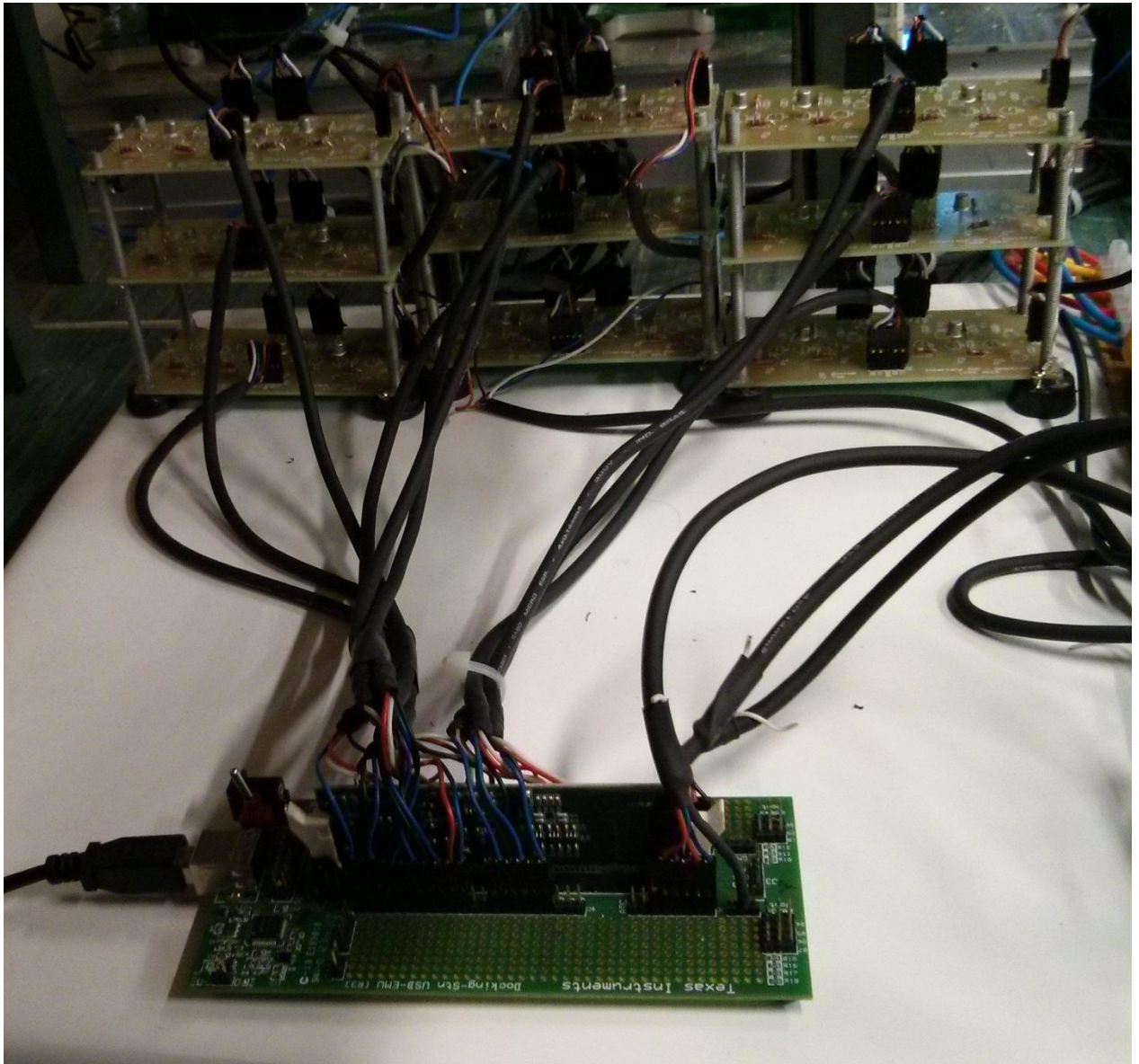

Figure 0-6: DSP and Interfaces

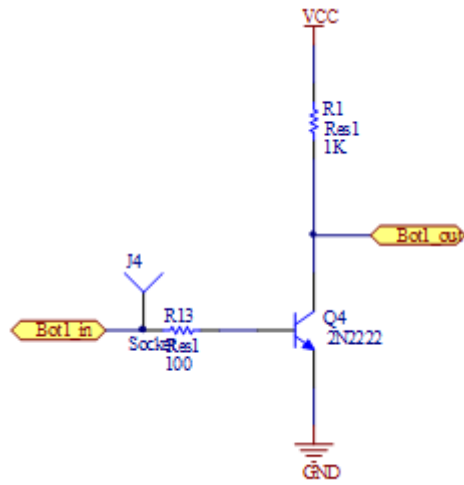The circuit diagram of the DSP Gate Driver interface is shown in Figure 0-7.

Figure 0-7: DSP Gate Driver Interface Circuit

Figure 0-8 shows the signal conditioning boards, the 6 LEM Hall Effect current sensors and the 3 LEM Hall Effect voltage sensors.
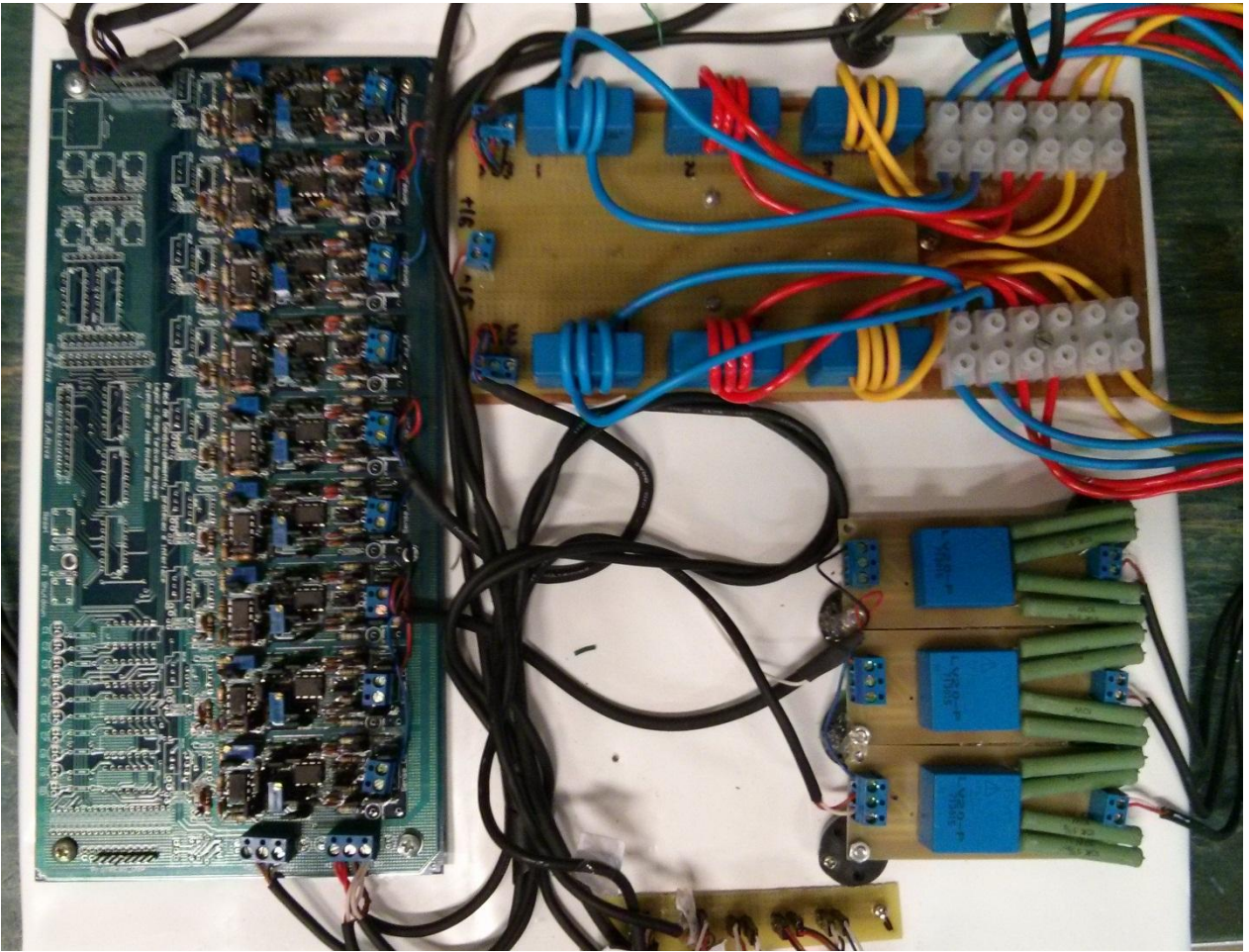
Figure 0-8: Signal Conditioning

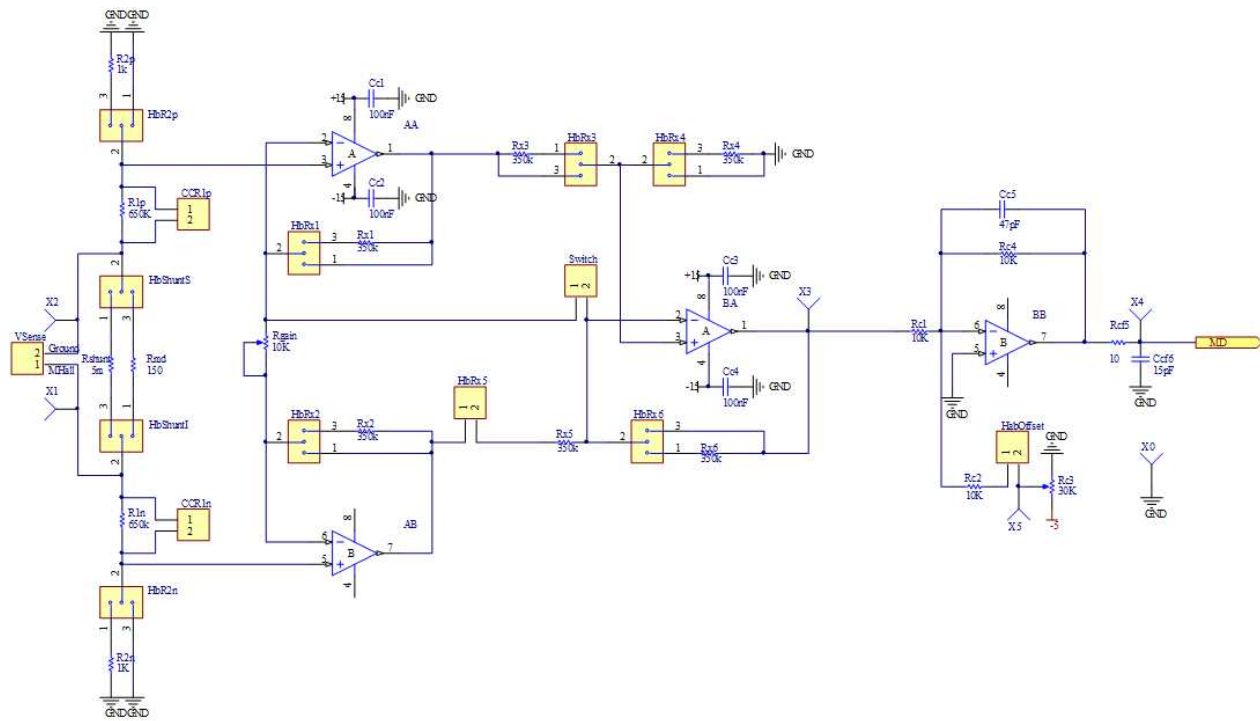The signal conditioning board has 9 channels; each channel implements the circuit of Figure 0-9.

Figure 0-9: Signal Conditioning Board Circuit

The above circuit is a differential amplifier, used to reject common mode signals and a low pass filter to damp the noise.

APPENDIX C- PUBLISHED PAPERS

Joel Filipe Guerreiro, José Antenor Pomilio, Tiago Davi Curi Busarello; "Design and Implementation of a Multilevel Active Power Filter for More Electric Aircraft Variable Frequency Systems;" COBEP Brazilian Power Electronics Conference; 27-31 October, 2013.

Joel Filipe Guerreiro, José Antenor Pomilio, Tiago Davi Curi Busarello; "Design of a Multilevel Active Power Filter for More Electric Airplane Variable Frequency Systems;" IEEE Aerospace Conference; 2-9 March 2013. p.p. 1 – 12.